Vol. 32

Remote Sensing Series

Daniel Schläpfer

Differential Absorption Methodology for Imaging Spectroscopy of Atmospheric Water Vapor

RSL Remote Sensing Laboratories
Department of Geography
University of Zurich, 1998

This dissertation has been approved by the Faculty of Mathematics and Natural Sciences of the University of Zürich on recommendation of Prof. Dr. Klaus I. Itten and Prof. Dr. Harold Haefner. The research has been co–supervised by Dr. Johannes Keller, Paul Scherrer Institute, Villigen, Switzerland.

Die vorliegende Arbeit wurde von der Mathematisch–naturwissenschaftlichen Fakultät der Universität Zürich auf Antrag von Prof. Dr. Klaus I. Itten und Prof. Dr. Harold Haefner als Dissertation angenommen. Die Forschungsarbeit wurde ausgeführt unter Mitbetreuung von Dr. Johannes Keller, Paul Scherrer Institut, Villigen (CH).

Remote Sensing Laboratories
Department of Geography
University of Zürich
Winterthurerstrasse 190
CH-8057 Zürich
Switzerland

http://www.geo.unizh.ch

Printed by the *Druckerei der Zentralstelle der Studentenschaft der Universität Zürich*

Summary

Differential Absorption Methodology for Imaging Spectroscopy of Atmospheric Water Vapor

The thesis describes the theory, preprocessing steps, and algorithms needed for differential absorption techniques in imaging spectroscopy. The procedure is shown especially for the retrieval of columnar water vapor content. This parameter is of major interest to meteorological applications as well as for atmospheric correction of remote sensing data.

The necessary radiometric laws and assumptions are given in the beginning of the study. The optical path of the solar radiation through the atmosphere to the ground and from the ground to a downward looking imaging spectrometer are specifically considered. The signatures of the atmosphere which are produced on this path are then depicted and validated according to their information content for imaging spectroscopy applications. The radiative transfer codes needed for the radiance simulation are compared, and some examples of their utility shown.

In the section on ground–based measurement of atmospheric properties, special emphasis is placed on the processing of sun photometer irradiance measurements. The performed calibration of the instrument on high altitude stations leads to the ability to measure aerosol optical thickness as well as the columnar water vapor content during experimental campaigns. The results of the sun photometer are then compared with values retrieved from in situ radiosonde measurements. The errors for both measurement methods are estimated and their viability for imaging spectroscopy described.

The imaging spectroscopy data have to be prepared appropriately for a correct atmospheric processing. The abilities and the calibration accuracy of the two instruments used (AVIRIS and DAIS) first are evaluated. Since both instruments measure from airborne platforms, their geometrical preprocessing is crucial for most of the applications including atmospheric correction and constituents retrieval. A new application is described which allows semi-operational geometric correction of airborne data based on a parametric approach. The geocoded data may then be atmospherically corrected with full respect for the geometry. The known atmospheric correction algorithms are described in a further section on preprocessing.

All preparations focus on the application of differential absorption techniques in imaging spectroscopy. Since only a limited number of channels is used for the differential absorption technique, they have to be selected from all avail-

able bands. A new quantitative method allows the selection of channels both in, and on both sides of a specific absorption feature. The method uses radiance simulations in each channel as well as the sensor characteristics. The thus defined channels are then combined into differential absorption techniques.

Starting with the radiometric assumptions, a new water vapor retrieval technique is derived which accounts for the atmospheric back scattered radiance in a different way than other techniques. This 'Atmospheric Precorrected Differential Absorption (APDA)' technique is described and validated, and some error analyses are conducted. It is shown that reliability of the water vapor retrieval over relatively dark targets is improved while the signal to noise ratio is slightly reduced. Furthermore, the relationship between amount of water vapor and transmittance is shortly analysed and the possible usage of the APDA technique is shown.

All techniques are tested on AVIRIS and DAIS data sets which originate from various campaigns between 1991 and 1996. The basic algorithms and their implementations are described. The results show that the performance of the new techniques is within a 5%–10% relative error range for columnar water vapor amounts. This high accuracy result is then processed in relation to the terrain elevation. This allows retrieval of final results such as water vapor profiles in mountainous terrain and sea level reduced water vapor quantities.

The analyses presented show how much information can be drawn from imaging spectroscopy data if differential absorption techniques are applied. The clue for an exact solution is the combination of geometric and atmospheric corrections and differential absorption techniques. If all of this is combined in a perfect model, accuracies may be achieved which are not possible if only the raw data are processed. The achieved results fulfill the requirements of meteorologic measurements as well as of remote sensing applications. The new techniques may also be used for an improved atmospheric correction of imaging spectroscopy data as well as for ground reflectance based imaging spectroscopy applications.

Zusammenfassung (German)

Bildspektrometrie von atmosphärischem Wasserdampf durch differentielle Absorptionsmethodik

Das Ziel der vorliegenden Dissertation ist eine umfassende Beschreibung von differentiellen Absorptionsmethoden und deren Anwendung in der Bildspektrometrie. Alle benötigten Vorverabeitungsschritte und Algorithmen werden in Bezug auf die Wasserdampferkennung dargestellt. Wasserdampf wurde gewählt, da er von speziellem Interesse für meteorologische Anwendungen ist und zudem als Hilfsparameter für die Fernerkundung benötigt wird. Ausserdem ist seine Signatur im elektromagnetischen Spektrum deutlich erkennbar, was genau quantifizierbare Resultate verspricht.

Zu Beginn der Studie sind die radiometrischen Grundsätze und Gesetze dargelegt, welche der Methodik dienen. Der optische Pfad des Lichtes wird dabei von der Sonne zur Erdoberfläche und zurück zur Sonne verfolgt, wobei der Beeinflussung durch die Atmosphäre besondere Beachtung geschenkt wird. Die Signaturen verschiedener atmosphärischer Bestandteile werden dabei untersucht und Zusammenhänge zwischen der Absorption durch Wasserdampf und der Streuung in der Atmosphäre aufgezeigt. Die Signaturen werden darauf auf ihre Verwendbarkeit in der Bildspektrometrie und ihren Informationsgehalt hin überprüft. Die Absorptionsbänder verschiedenster Gase sowie der spektrale Verlauf der Aerosol-Streufunktionen versprechen vielfältige Anwendungen.

Damit eine allfällige Anwendung evaluiert werden kann, sind bodengestützte Hilfsmessungen notwendig. Ein Instrument, welches in dieser Studie verwendet wurde, ist das Sonnenphotometer. Es misst die Einstrahlung auf Bodenhöhe, woraus Informationen über die Aerosole und den Wasserdampf der Atmosphäre gewonnen werden können. Auf die Kalibration des Geräts wird speziell eingegangen, da die Messungen als Referenzinformation gebraucht werden sollen. Insbesondere die Wasserdampferkennung wird beschrieben und deren Resultate mit den integralen Werten aus Radiosondenaufstiegen verglichen. Die Sonden werden als echte in-situ Methode oft für die Methodenevaluation verwendet. Deshalb werden die speziellen Eigenschaften der Radiosonden vor allem in Bezug auf Fernerkundungsanwendungen dargelegt.

Die Aufarbeitung von Bilddaten besteht aus Kalibration, Geocodierung, Qualitätsanalyse und atmosphärischer Korrektur. Diese Schritte werden anhand der beiden Bildspektrometer DAIS–7915 und AVIRIS dargelegt. Flugzeuggestützte Geräte sind während des Abtastvorgangs starken Bewegungen unterworfen. Deshalb ist es unumgänglich, sie mittels eines parametrischen Ansatzes zu

entzerren; aufgrund sämtlicher Fluglagedaten ist es möglich, die Geometrie in Bezug auf das Gelände für jedes Bildelement zu rekonstruieren und das Bild so zu geocodieren. Die Funktionsweise eines dazu erstellten Programmes wird erläutert. Die solcherart geocodierten DAIS- und AVIRIS-Bilder können nicht nur besser bezüglich von Bodeninformationen ausgewertet, sondern auch aufgrund der nun bekannten atmosphärischen Geometrie weiter prozessiert werden. Gewisse Atmosphärenkorrekturprogramme machen davon Gebrauch – ein Überblick über mögliche Ansätze zur Atmosphärenkorrektur wird zum Schluss dieses Kapitels gegeben.

Aus den Eigenschaften der Strahlung an einem hyperspektralen Sensor wird dann eine Methode zur präzisen Kanalauswahl für die differentielle Absorption hergeleitet. Sie ermöglicht die Reduktion der benötigten Kanalanzahl auf das Optimum mittels quantitativer Methoden. Danach werden die bekannten Methoden der differentiellen Absorption charakterisiert, welche die ausgewählten Kanäle verwenden. Die radiometrischen Annahmen, welche im Theorieteil dargelegt wurden, werden dann benutzt, um eine neue differentielle Absorptionsmethodik herzuleiten. Es ergibt sich, dass nur eine Vorkorrektur atmosphärischer Effekte es ermöglicht, einen direkten Bezug zwischen Gastransmission und differentiellem Signal herzustellen. Simulationen zeigen, dass diese neue Methode ('Atmospheric Pre-corrected Differential Absorption (APDA)' Technik) vor allem über dunklen (aber nicht schwarzen) Bodenreflektanzen wesentliche Verbesserungen gegenüber herkömmlichen Methoden bringt. Für tief fliegende Sensoren hingegen verschwindet das Wasserdampfsignal bei sehr dunklem Hintergrund im Rauschen.

Die Implementierung der Methodik und die Struktur der wichtigsten Algorithmen wird zum Schluss dargelegt und auf DAIS und AVIRIS Datensätze angewandt. Es stehen Datensätze zur Verfügung, welche aus Kampagnen von 1991, 1995 und1996 in der Schweiz und in Kalifornien stammen. Die resultierenden Wasserdampfsäulen werden mit Ballonsondierungen verglichen. Dabei kann bei den AVIRIS Daten eine gute Übereinstimmung im Bereich von 5–10% festgestellt werden. Die DAIS Daten müssen hingegen nachkalibriert werden, um in diesen Fehlerbereiches zu gelangen. Da die Szenen auf ein Geländemodell geocodiert sind, können die Resultatbilder mit der Topographie verknüpft werden. Es gelingt, Wasserdampfkonzentrationsprofile entlang von Steilhängen aus der Ableitung der Totalsäule zu berechnen. Mit dieser Methode kann zudem die Totalsäule auf eine Höhenniveau reduziert werden, womit die Interpretation der räumlichen Wasserdampfverteilung wesentlich vereinfacht wird.

Die Arbeit hat gezeigt, dass die Erkennung von Wasserdampf mit differentieller Absorptionsmethodik Resultate liefern kann, welche sowohl den Anforderungen der Fernerkundung als auch jenen der meteorologischen Forschung genügen. Die Wichtigkeit von kombinierter geometrisch-atmosphärischer Verarbeitung konnte für diese Art der Bildauswertung aufgezeigt werden. Diese Kombination wird den Schwerpunkt zukünftiger Arbeiten in diesem Forschungsbereich bilden.

Contents

List of Figures

List of Tables

Glossary

a) General

A	area	[m^2]
a,b,c	constants for equations	var.
i, j	counter variables	[-]
f	frequency	[Hz]
l, s	length	[m]
t	time	[s]
T	temperature	[K]
λ	wavelength	[nm]
ν	wavenumber	[cm^{-1}]
ω	angular frequency	[rad s^{-1}]

b) Irradiance/Radiance

E_0	extraterrestrial solar irradiance	[W/(m^2 nm)]
E_{dif}	diffuse solar irradiance	[W/(m^2 nm)]
E_g	ground solar irradiance	[W/(m^2 nm)]
E_{gnd}	solar flux (ground solar irradiance on real surface	[W/(m^2 nm)]
I	radiant intensity	[W/(sr nm)]
L_{atm}	atmospheric path radiance ('sky radiance')	[W/(m^2 sr nm)]
L_{atm}^M	atmospheric path radiance (MODTRAN simulated)	[W/(m^2 sr nm)]
L_s	total radiance at the sensor	[W/(m^2 sr nm)]
L_g	total ground reflected radiance at ground	[W/(m^2 sr nm)]
$L_{g,dir}$	direct ground reflected radiance at ground	[W/(m^2 sr nm)]
L_{gnd}	total ground reflected radiance at the sensor	[W/(m^2 sr nm)]
L_m	radiance at the sensor in a measurement channel	[W/(m^2 sr nm)]
L_r	radiance at the sensor in a reference channel	[W/(m^2 sr nm)]
ΔL	total radiance uncertainty at a sensor	[W/(m^2 sr nm)]
M	excitance of a radiation source	[W/(m^2 nm)]
ϕ_0	solar flux (extraterrestrial)	[W/nm]

c) Measurement, Calibration

g	gain of an instrument	[W/(m^2 sr nm DN)]
m	relative optical airmass	[-]
m_{wv}	relative optical airmass for water vapor	[-]
M_q	qualification factor q for a channel	[-]
M_{ref}	qualification factor for reference channels	[-]
M_{meas}	qualification factor for measurements channels	[-]
N_p	photon flux	[phot/s]
R_S	relative sun-earth distance	[AU]
R	ratio number from differential absorption	[-]
R_{APDA}	ratio number as derived by the APDA technique	[-]
V	voltage (uncalibrated digital numbers)	[DN]
V_0	sun photometer calibration constant related to the extraterrestrial irradiance)	[DN]
V_{DC}	dark current voltage	[DN]

d) Transmission, Absorption, Reflection

a	absorbency	[-]
n	index of refraction	[-]
N	number of absorbers	[particles]
Q	absorption efficiency	[-]
w_a	weighting factor for adjacency correction	[-]
$w_{atm,i}$	weighting factor for atmospheric path radiance correction	[-]
w_{r1} , w_{r2}	weighting factors for continuum interpolation	[-]
α	absorption coefficient	[m^{-1}]
ρ	apparent reflectance of the ground	[-]
ρ_g	reflectance of the target	[-]
ρ_{adj}	average reflectance of the adjacent area	[-]
τ_d	total downward transmittance	[-]
τ_u	total upward transmittance	[-]
$\tau_{d,i}$	[downward] transmittance of an atmospheric constituent i	[-]
$\tau_{d,irr}$	irradiance downward transmittance (including diffuse irradiance)	[-]
$\tau_{d,app}$	apparent downward transmittance (including diffuse irradiance and terrain sky view effect)	[-]
$\tau_{d,dif}$	diffuse downward transmittance	[-]
τ_{tot}	total apparent path transmittance of the atmosphere	[-]
τ_{wv}	total apparent path transmittance of water vapor	[-]
τ_{wv}^{dif}	diffuse apparent path transmittance of water vapor	[-]

τ_0	total apparent transmittance of the dry atmosphere	[-]
τ^*	optical thickness	[-]
τ^*_{ae}	aerosol optical thickness	[-]
τ^*_0	vertical optical thickness	[-]
σ	scattering coefficient	[m^{-1}]
γ	extinction coefficient	[m^{-1}]

e) Geometry

FOV	sensor total Field of View	[rad]
h	height above sea level	[m]
h_a	airplane height	[m]
h_{pix}	pixel height (from DEM)	[m]
rol	airplane roll angle	[rad]
pit	airplane pitch angle	[rad]
hed	airplane true heading angle	[rad]
$\mathbf{R}$	airplane roll matrix	
$\mathbf{P}$	airplane pitch matrix	
$\mathbf{H}$	airplane true heading matrix	
$\vec{L}$	theoretical view vector	
$\vec{L}_l$	effective view vector per pixel	
$\vec{P}_a$	airplane position vector	
$\vec{P}_{pix}$	pixel position vector	
s	sky view factor (terrain)	[-]
s_θ	incidence sky view factor (dependent on solar zenith angle)	[-]
θ_a	astronomical sun zenith angle	[rad]
θ_e	exo-atmospheric sun zenith angle	[rad]
θ_g	observed ground sun zenith angle	[rad]
φ	irradiance incident angle	[rad]
Ω	solid angle	[sr]

f) Meteorology

e_s	saturated vapor pressure	[hPa]
H	relative water vapor concentration	[%]
l_{vis}	visibility	[km]
p_{air}	air pressure	[hPa]
p_{part}	partial gas pressure	[hPa]
PW	precipitable water column	[cm]/[kg/(m^2)]
u	precipitable water concentration	[g/(m^3)]
ρ_{wv}	water vapor density	[kg/m^3]

g) Constants

c	velocity of light	$= 2.9979 \times 10^8$ m/s
p_0	standard atmospheric pressure	$= 1013.25$ hPa
r_E	earth radius	$= 6.371 \times 10^6$ m
$R_{S,0}$	earth-sun distance	$= 1.496 \times 10^{11}$ m (=1 AU)
T_S	radiant temperature of the sun	$= 5770$ K
R	ideal gas constant	$= 8.3143$
M_{wv}	molecular weight of water	$= 0.018015$ kg/m^3

Chapter 1:

Introduction

Imaging spectroscopy provides remote sensing data at high spectral and spatial resolution. The data bear information on the land cover as well as on the atmosphere. The analysis of this data in relation to atmospheric absorbers is the main goal of this study.

1.1 Problem Description

The following problems have to be addressed to achieve results on imaging spectroscopy of atmospheric absorbers in general:

- appropriate notation of the radiometry for the atmospheric application,
- characterization and calibration of ground based validation instruments,
- standardization of imaging spectroscopy data preprocessing for atmospheric applications,
- definitions and tests of differential absorption methodologies,
- definition of algorithms for one chosen methodology and their implementation.

These single tasks lead to a network of theory, algorithms, and procedures which altogether describe a differential absorption methodology for imaging spectroscopy. In this thesis, the methodology is developed and tested with special respect to the atmospheric water vapor retrieval although it might also be used for other absorbers.

1.2 Remote Sensing of Atmospheric Water Vapor

Water vapor is one of the main driving forces in the global weather cycle and is mainly involved in mesoscale air transport processes. Its concentration in the earth's atmosphere varies significantly with time and location. The exact measurement and prediction of the amount of water vapor in the atmosphere is therefore an important task for remote sensing applications and meteorology.

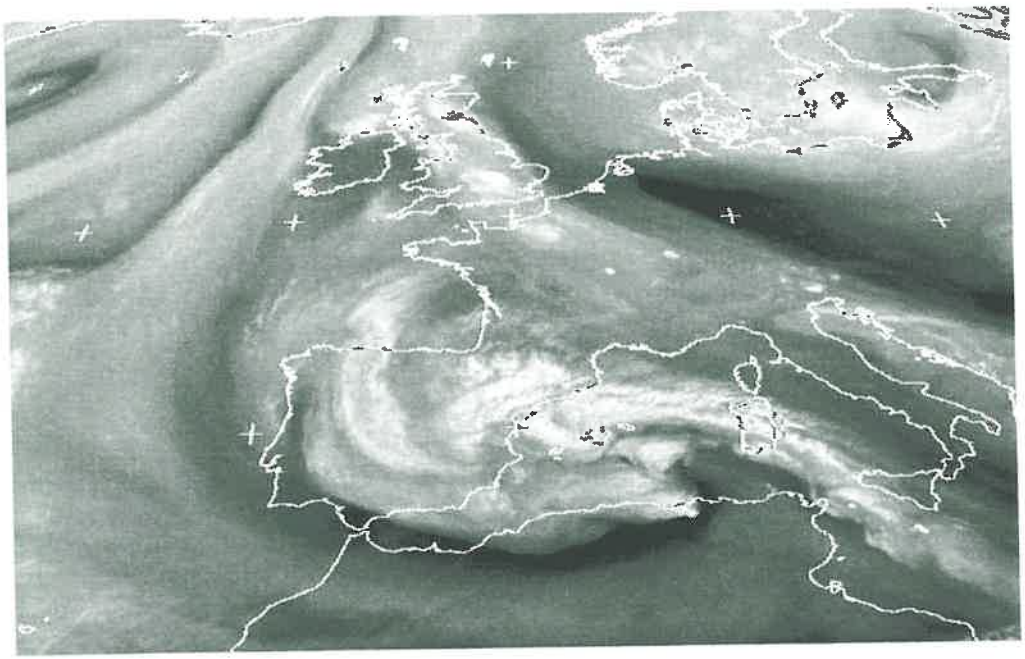

Figure 1.1: Water vapor emission over Europe as seen by the Meteosat sensor in the infrared channel at 5.7 - 7.1 µm. Spatial resolution: 5 km, Date: 14th of May 1998 (source: [48], ©EUMETSAT).

Moreover, about one third of the spectral range where optical sensors are sensitive is affected by water vapor absorption. This implies that remote sensing of the earth surface using optical data is only meaningful if the atmospheric correction is performed properly. An accurate atmospheric correction is only possible if the spatial distribution of both the aerosol loading and the water vapor distribution are known. The methods described in this study concentrate on water vapor, although they could also be applied to any other absorbing gases of the atmosphere. Moreover, water vapor is the 'most wanted' gaseous absorber of the atmosphere for meteorologic applications as well as for atmospheric correction algorithms in remote sensing.

Current operational systems for water vapor detection are primarily based on the emission in the thermal infrared (AVHRR, GOES, ATSR, Meteosat) or in the microwave radiation bands (DMSP) (see [6], [45], and [46]). They allow measurements of vertical profiles at a resolution down to 1 km in the lower tropospheric layers. The disadvantages of such satellite sounding systems are a coarse spatial (horizontal) resolution ranging from one to tens of kilometers and a limited insight into the lower troposphere. Imaging spectroscopy, on the other hand, measures total column water vapor content at a high horizontal spatial resolution and therefore has the potential to complete the abilities of the sounding systems.

1.3 Differential Absorption Techniques in Imaging Spectroscopy

The sensors of the current imaging spectrometers (e.g. the AVIRIS instrument) are capable of acquiring hyperspectral data in dozens to hundreds of bands in the visible and near infrared part of the electromagnetic spectrum, usually between 400 and 2450 nm wavelength. The spectral resolution ranges from 5 to 50 nm while the spatial resolution is between 5 and 50 meters. The measured radiances depend on spectral reflectance of the earth's surface, as well as on absorption and scattering in the atmosphere.

The measurement of water vapor (or any other absorbing species) can be performed using sensor channels located in bands (or on lines) of the absorption spectrum. The AVIRIS sensor has been used to retrieve water vapor [32] and, with less accuracy, oxygen [33], carbon dioxide [17], and ozone [65]. The water vapor amount is retrieved by applying the so-called differential absorption technique ([11] and [40]). This technique will be described extensively in Chapter 5. Various ratioing methods have been developed so far based on different channels and calculation techniques, and there still remains great potential for further developments.

The influence of an atmospheric gas of interest on the radiance at the sensor level is usually simulated by radiative transfer codes. In this study, the spectral transmittance and the atmospherically scattered radiance are calculated by MODTRAN simulations [44]. The use of such radiative transfer codes is the only reliable way to invert radiance values measured at the sensor level: Generally, a Look Up Table is computed which is inverted numerically for the input parameters such as aerosol content, aerosol type, or gas amounts in the atmosphere. The differential absorption technique used in this study allows inversion of the relationship of radiance at the sensor to columnar water vapor abundance. The direct retrieval of vertical profiles from imaging spectroscopy data is not possible. Nevertheless, some approaches are shown which use modeling steps over the Digital Elevation Model (DEM) to invert for the atmospheric profile along terrain slopes.

1.4 Organization of this Thesis

Atmospheric processing algorithms are based on fundamental radiometric concepts. The notations and assumptions made for remote sensing applications are described in Chapter 2. Additionally, the signatures of atmospheric constituents and principles of their simulation with radiative transfer codes are shown in that chapter. The full explanation of all parameters used can be found in the glossary at the beginning of the thesis.

The main auxiliary data sets are derived from radiosonde data and from sun photometer measurement. These retrieval techniques are described and their

errors are estimated in Chapter 3. The sun photometer is used as a ground based instrument for atmospheric water vapor and aerosol measurement. The techniques for the retrieval of both constituents and their implementation are shown in that chapter. This leads to a first application of a differential absorption technique for water vapor.

For the appropriate processing of imaging spectrometry data for water vapor, additional auxiliary data have to be evaluated and the image data have to be preprocessed accurately. Some tests regarding the radiometric calibration of the data sets are shown, and a procedure for geometric correction of airborne imaging spectrometer data is described in Chapter 4. The procedure was developed as a general preprocessing tool with special respect to atmospheric applications. This step was particularly necessary for atmospheric processing in mountainous terrain. Accurate preprocessing allows one to relate the derived water vapor content to the terrain without introducing substantial terrain dependent errors.

The principles of differential absorption and channel selection are described in Chapter 5. The major differential absorption techniques are compared to modern techniques by using simulated data as well as the image information.

The results in application to imaging spectroscopy data follow in Chapter 6. The application of the methodology shows the reliability of the procedures. The tests are mainly done on DAIS and AVIRIS data, originating from California and Central Switzerland. Some modelling experiments using the terrain information are depicted in the end of the chapter.

The used acronyms, some special definitions to this thesis, the used hardware and software are described in the appendix pages. Additionally, the description of the developed program modules can be found in those pages. Digital data and code are available upon special request to the author.

Chapter 2:

Signatures of the Atmosphere

Atmospheric gases and the aerosols in general influence the radiation transport in the atmosphere. The most important quantities relevant to optical remote sensing are the aerosol loading and the amount of water vapor. Aerosols are well known for their strong scattering effects especially in the visible and near infrared part of the spectrum, whereas water vapor absorbs in multiple strong bands, distributed over the whole spectral range. Additionally, water vapor is a major molecular scatterer at low wavelengths (in combination with the scattering effects of other atmospheric gases).

As in most meteorological science applications it is actually impossible to setup reliable experiments to isolate the signal of a single parameter variation. All measurements of the radiative signal contain a mixed signature of all atmospheric parameters and constituents. These signatures are not easily discernible from one another. The only way to obtain separated signatures of the atmosphere is through use of radiative transfer codes. They allow variation of one single parameter of the virtual atmosphere while leaving the remaining parameters untouched. This methodology produces spectral data which afterwards can be compared with image data.

This chapter first reviews the definitions and used fundamental equations of radiometry (see the Glossary on page XIX for a description of the single parameters). It then shortly describes the radiative transfer code MODTRAN [44]. Some examples of atmospheric signatures of water vapor and aerosols are finally given.

2.1 Radiant Path through the Atmosphere

The main source of the radiance in optical remote sensing is the sun. More than 99.9 percent of the sensor signal in the visible part of the spectrum comes from that source. Even at 2.5μm the emitted radiance of the earth contributes only about 1% to the total radiance (at regular surface temperatures). Hence, the emitted radiance of the earth is ignored throughout this study.[1] This section describes

how the radiance can be expressed on its way from the sun to a sensor. This derivation is mainly based on the description in the 'Handbook of Optics' [85].

2.1.1 Path from the Sun to the Earth's Surface

The origin of the radiative path is the sun. The source spectrum is already influenced by the sun's atmosphere, resulting in various absorption lines in the solar spectrum, the so-called Fraunhofer lines. They are assumed to be of constant strength and therefore do not have to be accounted for in imaging spectroscopy.

The extraterrestrial irradiance E_0 is now defined as the solar energy flux ϕ_0 per unit area (in [W/m^2], area perpendicular to the beam direction) at the top of the atmosphere (in the following, the wavelength index is usually dismissed since almost all parameters in atmospheric modeling depend on the spectral position):

$$E_0 = \frac{\phi_0}{A_\perp}. \tag{2.1}$$

The extraterrestrial irradiance is mainly influenced by the sun-earth distance and temporal variations of the solar excitance M (emitted radiance). The measured radiance just above the atmosphere at the average sun-earth distance is taken as a reference for further radiative transfer calculations. This solar spectrum is continuously updated by measurements from spaceborne instruments (e.g. from satellites), and by sun photometer extrapolations by the world radiation centers. Currently, a compilation of such data from various sources for different wavelength ranges is used [44]. The integration of the solar irradiance over the wavelength range is called the solar constant and denotes the total energy transmitted from the sun to the earth. This parameter is seldom used in imaging spectroscopy because it is lacking any spectral information.

On its path from the top of the atmosphere to the ground, the radiation is scattered and absorbed by atmospheric aerosols and trace gases. The downward transmittance τ_d is a combination of aerosol and gas transmittances of the single atmospheric constituents i:

$$\tau_d = \prod_i (\tau_{d,i}). \tag{2.2}$$

A proportion of the scattered radiance is redirected back to space while the remainder is scattered forward to the ground, or may even be scattered multiple times between the atmosphere and the ground (trapping effect). Together with the direct transmitted irradiance, this diffuse irradiance E_{dif} contributes to the total irradiance E_g at the ground level:

1. However, in bands of total atmospheric absorption, the emitted radiance can be exploited by optical sensors to determine ground fire temperatures (Green 1998, JPL, Pasadena, oral presentation).

$$E_g = E_0\tau_d + E_{dif}. \tag{2.3}$$

The diffuse irradiance is usually written as the product of the extraterrestrial irradiance E_0, the diffuse downward transmittance $\tau_{d,dif}$, and the incidence sky view factor s_θ. Equation (2.3) is then written as

$$E_g = E_0\tau_d + E_0\tau_{d,dif}s_\theta = E_0(\tau_d + \tau_{d,dif}s_\theta). \tag{2.4}$$

The irradiance transmittance ($\tau_{d,irr} = E_g/E_0$) could be measured by evaluating the incident energy on a plane perpendicular to the sun direction and taking the ratio to the (known) extraterrestrial irradiance E_0. The zenith angle dependent skyview factor s_θ accounts for the reduced diffuse irradiance on a tilted plane (which is perpendicular to the incident beam by definition). An example of simulated irradiance spectra is shown in Figure 2.1. Nearly half of the solar energy below a wavelength of 1400 nm does not reach the ground. The water vapor absorption features (broad bands) are clearly evident in the ground irradiance spectrum while they are not visible above the atmosphere.

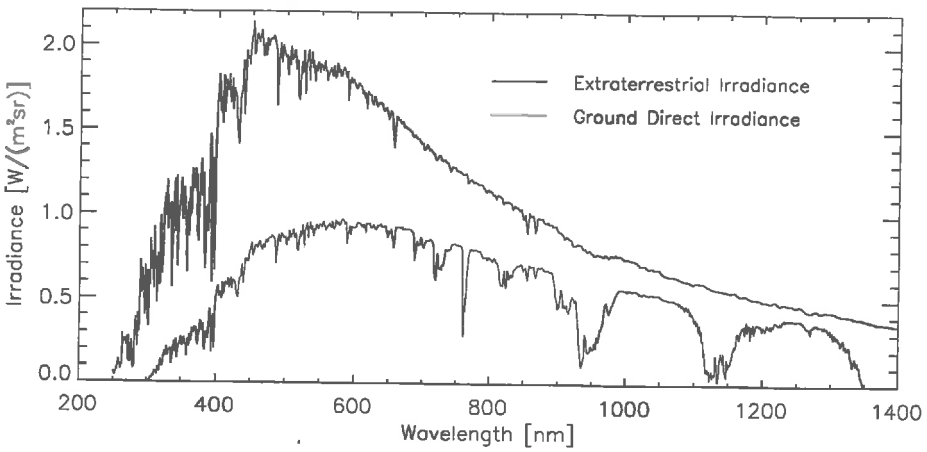

Figure 2.1: **Solar irradiance at the top of the atmosphere and at the ground at typical Swiss summer atmospheric conditions (MODTRAN simulation).**

2.1.2 Irradiance on a Real Surface

The definition of the irradiance given in equation (2.4) is not suited for remote sensing since it does not consider slope and aspect of the terrain. The solar flux (direct irradiance on a real surface[2]) is the irradiance reduced by the cosine of the incident angle φ, whereas the diffuse irradiance only depends on the sky view fac-

2. The terms 'irradiance' and 'solar flux' are used synonymously within this work to avoid definition conflicts between direct and diffuse irradiance.

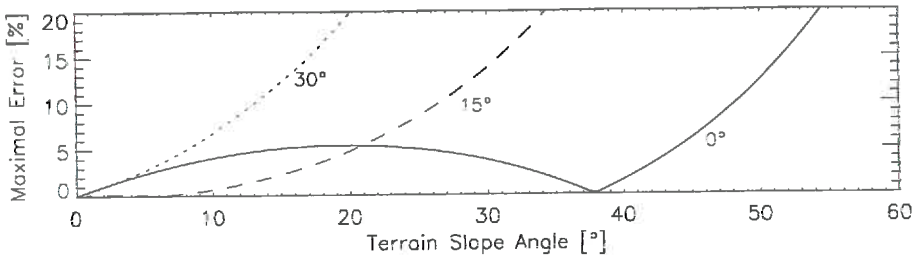

Figure 2.2: Maximum error of the cosine assumption for the sky view factor, calculated for three different sun zenith angles. The analysis is made in a plane in path azimuth direction.

tor s of the target related to the local terrain shape [59] (this sky view factor is terrain dependent, conversely to s_θ). The irradiance on a real surface E_{gnd} is then derived from equation (2.4) as

$$E_{gnd} = E_0 \tau_d \cos\varphi + E_0 \tau_{d,\,dif} s = E_0 \cos\varphi \left(\tau_d + \tau_{d,\,dif} \frac{s}{\cos\varphi} \right), \qquad (2.5)$$

where s is the skyview factor and φ is the angle between the solar direction and the vector perpendicular to the surface (compare Figure 2.3).

The relation of $\cos\varphi$ to s is now assumed to be a constant for one scene[3]. In a first approximation, the skyview factor decreases linearly with the slope angle α, such that $s = (180° - \alpha)/180°$. This function is now compared with the cosine of φ (see Figure 2.2). The analysis depicts that the assumption for a constant relation is valid only for slope angles up to 20 to 40 degrees, within an error range of 10% while the solar zenith angle should not be greater than about 30 degrees. The ground irradiance then is set to

$$E_{gnd} \approx E_0 \cos\varphi (\tau_d + c\tau_{d,\,dif}) = E_0 \cos\varphi \tau_{d,\,app}, \qquad (2.6)$$

with the apparent downward transmittance $\tau_{d,app} = \tau_d + c\tau_{d,dif}$. The approximation in equation (2.6) can be made as long as the direct irradiance is significantly larger than the diffuse irradiance, the average terrain slopes are lower than about twenty degrees, and if the image is taken (e.g.) at noon under midlatitude summer geographical conditions. If these requirements are not fulfilled, the diffuse irradiance has to be accounted for separately in atmospheric correction as well as in gas retrieval procedures.

2.1.3 Ground Reflection

As the solar irradiance is reflected at the ground, further parts of the incident energy are lost for remote sensing. The reflectance ρ_g is defined as the part of the

3. The c- or the Minnaert model accounts for this behaviour; see Section 4.5.1 on page 58.

energy reflected by the ground assuming a Lambertian target (this means that given a constant field of view the measured reflectance is constant from all viewing directions). The direct ground reflected radiance then is defined as

$$L_{g,\,dir} = \frac{\rho_g}{\pi} E_{gnd}\,. \tag{2.7}$$

The unit of the radiance is W/(m² sr nm). The factor π originates from the integration of the radiance over the hemisphere for comparison with irradiance measurements. The emitted radiance would add to this expression for thermal applications.

For a general target in the radiative path, the incoming, absorbed and outgoing radiation must be balanced. Thus, for an illuminated object the following rule applies:

$$\rho + \tau + a = 1\,, \tag{2.8}$$

where a is the absorbency of the object. The equation (2.8) is strictly valid for any wavelength interval because it does not include the emission term. According to Kirchhoff's law, the emission of the object has the same coefficient as the absorbency integrated over the whole spectral range. However, there are often transitions from absorption at short wavelengths to thermal emission at longer (infrared) wavelengths. These effects do not influences the atmospheric radiance transfer significantly in the visible/near infrared part of the spectrum.

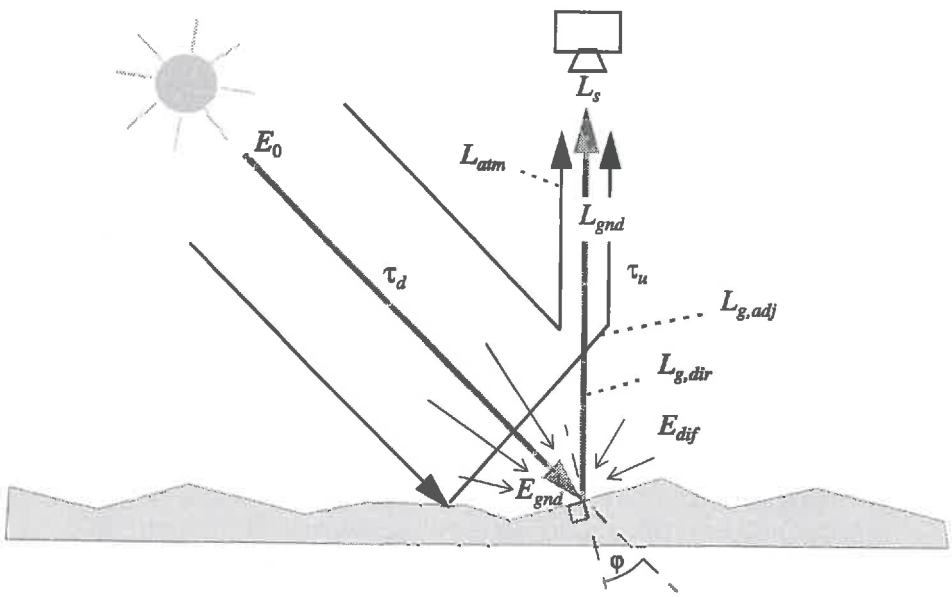

Figure 2.3: Components of the radiance at an imaging spectrometer sensor. The radiant path through the atmosphere of the single components is illustrated (see also [19] and the Glossary for the single parameters).

2.1.4 Path from the Ground to the Sensor

On the path of the beam to the sensor two major scattering components are added to the ground reflected radiance (see Figure 2.3). The first scattering component originates from radiance which is reflected by the adjacent area of the target pixel and subsequently scattered into the path. This adjacency effect can contribute significantly to the total radiance for high altitude sensors in the visible and ultraviolet part of the spectrum. The spatial spread of this effect can reach up to 1-2 km [76]. The effect can be treated as a bias on the reflectance of the target pixel. Thus the total ground reflected radiance is described as

$$L_g = L_{g,\,dir} + L_{g,\,adj} = (\rho_g + \rho_{adj} w_a)\frac{1}{\pi} E_{gnd}, \tag{2.9}$$

where ρ_{adj} is the average reflectance of the adjacent area and w_a is a weighting constant for the adjacency effect (dependent on the amount of aerosols within the atmosphere). The atmospheric paths for both ground reflected components is approximately the same. If the interest focuses mainly on the atmosphere and not on the ground reflectance, ρ_{adj} and ρ_g can be combined with the cosine of the incident angle to one parameter ρ which is called the apparent ground reflectance

$$\rho = (\rho_g + \rho_{adj} w_a)\cos\varphi. \tag{2.10}$$

The upward direct transmittances $\tau_{u,i}$ of the various atmospheric components i multiply in the same way as the downward transmittances and can be combined to the total path transmittance

$$\tau_{tot} = \prod_i \tau_i = \prod_i \tau_{d,\,app,\,i} \prod_i \tau_{u,\,i}. \tag{2.11}$$

A last additive term to the radiance at the sensor is the atmospherically backscattered radiance L_{atm} which never was influenced by the ground. This sky radiance is also affected by the atmospheric transmittance, but the shape of the absorption is very different from the total transmittance due to the shorter average path length.
The total radiance at the sensor can now be fully described as

$$L_s = \tau_u(\rho_g + \rho_{adj} a)\frac{1}{\pi}\cos\varphi\left(\tau_d + \tau_{d,\,dif}\frac{s}{\cos\varphi}\right)E_0 + L_{atm}. \tag{2.12}$$

For the application in atmospheric processing this equation can be reduced to a much more simple form, using the above equations (2.5)- (2.11):

$$L_s = \rho\tau_{tot}\frac{1}{\pi}E_0 + L_{atm}. \tag{2.13}$$

The apparent ground reflectance ρ includes the terrain slope dependent reflec-

tance of the observed pixel as well as the average influence of the adjacent area. In real data, the adjacency effect is always present, producing a bias on the data in addition to the atmospheric path radiance. Therefore ρ will never be zero in real data. It would be very small only for large areas of very small reflectances and for low altitude image acquisition (where the adjacency factor a is small). All parameters of equation (2.13) depend on the wavelength of the used channel. Note that the channel indices are not written in these equations.

2.1.5 Optical Thickness

For the imaging spectroscopy of atmospheric species, their specific transmittance has to be related to the amount of the specific constituent along the light path. Beer's law describes the attenuation for a single (gaseous) absorption line:

$$\tau_i = e^{-\int \gamma dl} = e^{-\tau^*} = e^{-m\tau^*_0}, \tag{2.14}$$

where γ is the extinction coefficient for a specific absorber along a path, and l is the optical path length [78]. τ^* is the optical thickness of the atmosphere for an arbitrary path and τ^*_0 is the optical thickness for a vertical path (often also referred as optical depth); m is the relative optical airmass (see Section 3.1.3 on page 23). Both m and τ^* are unit-free numbers (note that transmittance τ and optical thickness τ^* are defined differently). Similarly, this exponential law may also be used to describe the attenuation due to scattering aerosols [78]. However, if a number of absorption lines combines to an absorption band, equation (2.14) is no longer valid exactly. The exponential behaviour of the transmittance in relation to the optical thickness will persist.

The extinction coefficient γ in equation (2.14) can also be defined on the basis of the number of absorbers N per m^3 in the path [41]:

$$\gamma = \int_0^\infty \pi a^2 N(a) Q(a) da. \tag{2.15}$$

Q is the absorption efficiency for a specific species. Both parameters (Q and N) depend on the particle radius a for scattering effects. For gaseous absorption effects no such dependency is evident. Thus, equation (2.15) reduces to

$$\gamma = \pi a^2 NQ = N\kappa, \tag{2.16}$$

where κ is the absorption coefficient for the specific gas (unit: m^2/particle).

2.1.6 Atmospheric Refraction

Due to the atmospheric refraction, the radiant path through the atmosphere is not a straight line. The bending depends on the refractive index (n). Thus, the path is longer as if a straight path is assumed. The refractive index of air is a function of humidity, temperature and pressure ([20], compare also [15]) as follows:

$$(n-1)10^{-6} \cong \left[a_0 + \frac{a_1}{1-\left(\frac{\nu}{b_1}\right)^2} + \frac{a_2}{1-\left(\frac{\nu}{b_2}\right)^2} \right] \cdot \frac{(p-p_{wv})}{p_0} \cdot \frac{296.15\ \mathrm{K}}{T} + \left[c_0 - \left(\frac{\nu}{c_1}\right)^2 \right] \left(\frac{p_{wv}}{p_0}\right), \tag{2.17}$$

with the following constants and parameters:

$a_0 = 83.43$,	$a_1 = 185.08$ $a_2 = 4.11$	
$b_1 = 1.140 \times 10^5$	$b_2 = 6.24 \times 10^4$ c0 = 4349	c1 = 1.70×10^4
p_0	standard pressure (= 1013.25 hPa)	
p_{wv}	partial pressure of water vapor	[hPa]
ν	wavenumber	[cm-1]
T	air temperature	[K].

The partial pressure of water vapor is derived from relative humidity (RH) as $p_{wv} = RH \cdot e_s$, where the water vapor pressure in saturated air (e_s) is usually calculated by the approximate equation (see [77]):

$$e_s \cong e_{s,0} \cdot \mathrm{e}^{\frac{a(T-273.16\mathrm{K})}{(T-b)}}, \tag{2.18}$$

with the constants over liquid water:

a = 17.26939	b = 35.86 K
$e_{s,0}$	e_s at T = 273.16 K (= 6.1078 hPa).

More accurate equations for the pressure of saturated water vapor were compared by Murray [51]. The simple approximation (2.18) was shown to be accurate within 0.1% for typical atmospheric conditions. The error increases for very dry and cold atmospheres at temperatures below zero degree Celsius (273.16 K).

2.2 Radiative Transfer Codes

The transfer equations of the radiation in the atmosphere are well known (see [31] and [47]), but their solution in an efficient manner cannot be easily reached. Various codes have been created to solve this problem. The most common implementations for use in remote sensing are 6S [76] and MODTRAN [44], and to some extent LOWTRAN[43] and FASCOD [82].

Table 2.1 on page 13 shows a comparison between the two major radiative transfer codes. 6S is a convenient code for multispectral imagery and allows the simulation of the signal at a standard sensor in fast computing time. MODTRAN on the other hand provides data of higher accuracy at the cost of a slower speed. Since the differences can reach 10 percent (especially in absorption features

Acronym	6S	MODTRAN 3.5
Name	Second Simulation of the Satellite Signal in the Solar Spectrum	Moderate Resolution LOWTRAN
References	[76],[81]	[4],[44]
Related codes	5S	LOWTRAN, FASCOD
Atmospheric models	standard atmospheres 32 levels	AFGL standard atmospheres, 50 levels
Radiation path	straight 13 levels iteration for aerosols	bended (refractive) full 33 levels iteration
Aerosol Models	continental, urban, maritime, Shettle desert, visibility of 5km	rural, urban, maritime, desert for visibilities 2-50 km, stratospheric models available
Gases considered	O_2,O_3, H_2O, CO_2, CH_4, N_2O	O_2,O_3, H_2O, CO_2, CO, CH_4, SO_2, NO, N_2O, NO_2, NH_3, HNO_3
Band model	derived from AFGL 84 atlas, pressure and temperature dependent 10 cm^{-1} compilation	derived from HITRAN 92, pressure and temperature dependent 3-parameters 1 cm^{-1} compilation
Best resolution	5 cm^{-1}	2 cm^{-1}
Scattering algorithms	2-Stream method (successive scattering)	ISAAC 2-stream DISORT
Modi	at sensor radiance inverse run	transmittance radiance solar irradiance
Special features	BRDF support common satellite orbits	cloud & cirrus models 'hyperspectral' outputs
Application	multispectral imagery, BRDF research VIS-NIR range	hyperspectral imagery in-flight-calibration full optical wavelength range

Table 2.1: Comparison of the 6S and the MODTRAN radiative transfer code.

and above 2 micrometers), MODTRAN is the choice for hyperspectral data processing. 6S is used only if fast performance is necessary and the main interest is the visible/near infrared part of the spectrum.

All simulations and also the Look Up Table (LUT) generation in this study have been performed using MODTRAN. The slow but accurate 'Discrete Ordinate Transfer' option (DISORT, [47]) had to be used for the aerosol multiple scattering in order to reach the highest possible accuracy within the absorption features.

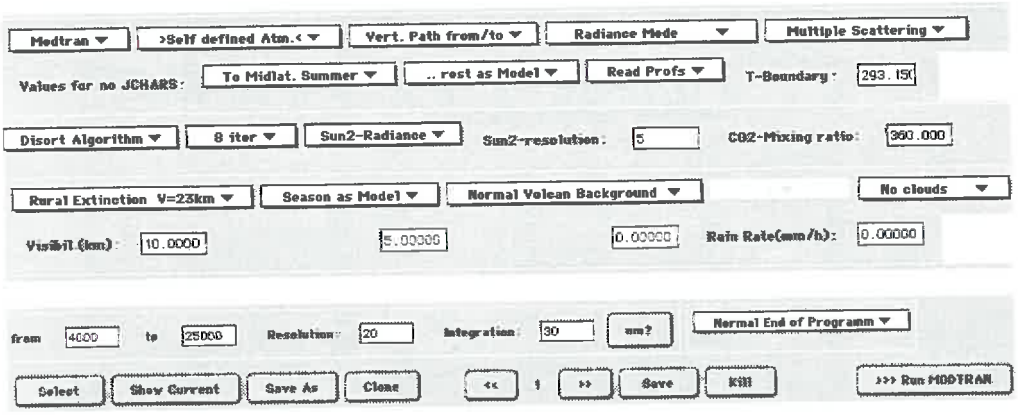

Figure 2.4: Example subset of the MODTRAN interface 'MODO'; translator for the ASCII input file 'tape5' (see Appendix D.1).

2.2.1 The 'MODO' Interface

The extensive use of the code led to the necessity of creating a special interface to MODTRAN. The IDL-widget interface was mainly constructed to provide a graphical user interface to MODTRAN which eases the setup of the various input parameters (described by an ASCII file, the so called 'tape5'). Most of the input parameters can now be set using pull-down menus instead of manually editing the rigidly formatted ASCII file.

Additional features allow the plotting of the spectral output, the extraction of single spectra from the whole output and the convolution to hyperspectral (Gaussian) channel characteristics. Other key-features include the creation and handling of multiple run tape5's, the editing of a customized atmospheric profile (except aerosols) and the direct and unrestricted execution of MODTRAN. A sample of the MODO input window is shown in Figure 2.4. and a description of the (shareware-) code and its key features can be found in Appendix D.1.

2.3 Signatures of Aerosols

Aerosols have a very strong impact on the radiance, especially in the ultraviolet and visible part of the spectral range. The absorption of radiation is primarily affected by scattering processes. 'Rayleigh scattering' occurs only with small particles (molecules). The attenuation due to this effect depends on the wavelength exponentially to λ^{-4}. The forward– and backward scattering effects are symmetrical for this kind of attenuation.

The 'Mie scattering' is an attenuation process mainly due to aerosols. Its dependence on the wavelength varies for different aerosol size distributions. It can thus not be described easily using an analytical expression. Mie scattering

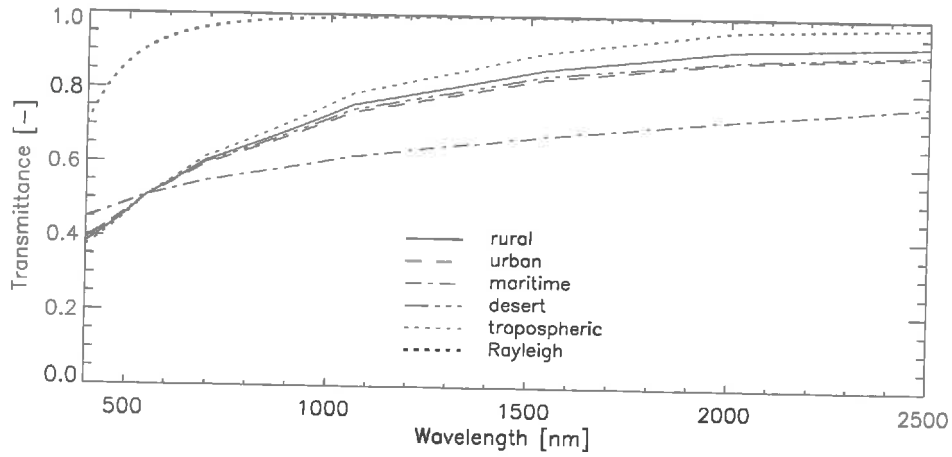

Figure 2.5: **Transmittance characteristics of various aerosol types and the Rayleigh scattering transmittance for a vertical path through a midlatitude summer atmosphere at a visibility of 10 km [MODTRAN simulation].**

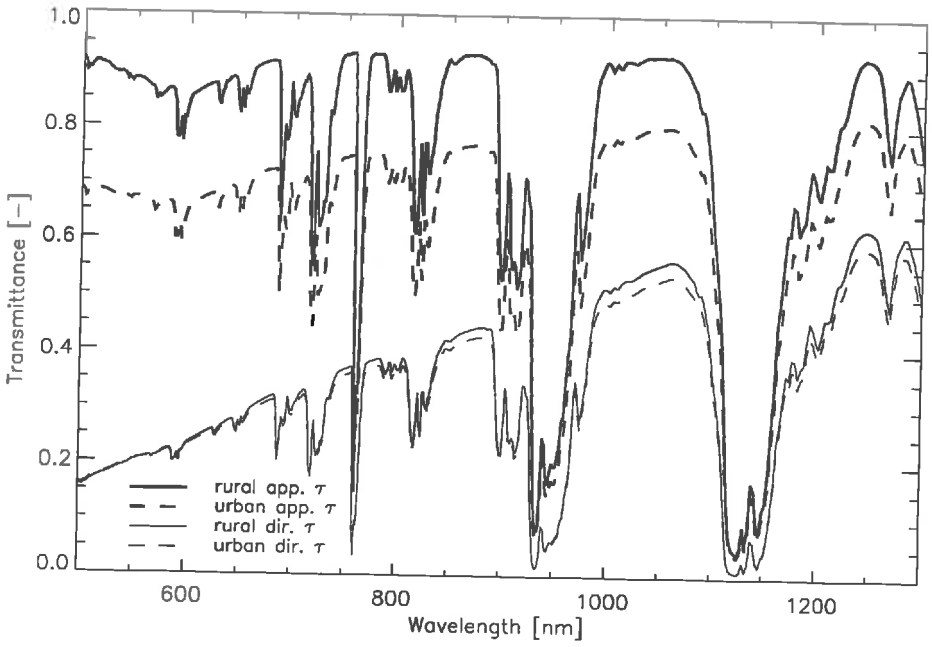

Figure 2.6: **Apparent (effective) and direct total transmittance for urban and rural aerosol profiles. The apparent transmittance contains direct transmitted and backscattered radiance while the direct does not include (added) path scattered radiance [MODTRAN simulation].**

depends on the wavelength exponentially at λ^{-a}. The Ångström coefficient a varies between 0.5 and 1.5, depending on the aerosol size distribution. High coefficients are related to small scattering particles. For large particles, the scattering effects are no longer dependent on the wavelength, but produce a constant attenuating effect on the signal (e.g. fog or dust). The complete theory of scattering is described in [78].

The aerosol size distribution determines the spectral shape of the transmission function together with the assumed amount of atmospheric gas molecules. The amount of molecules is directly defined based on the assumed surface pressure. Some typical transmittance curves for standard aerosol models (as provided by MODTRAN) are shown in Figure 2.5. The maritime aerosol model is dominated by hydrogenated aerosols which are larger than rural aerosols. Thus, the scattering effect persists also for higher wavelengths, because of the low Ångström coefficient.

The scattering transmittance is reciprocal to the amount of backscattered radiance. Thus, the apparent transmittance at the sensor level for aerosols has a very different spectral shape than the direct transmittance (see Figure 2.6). The path scattered radiance adds to the ground reflected radiance such that the apparent transmittance for scattering is quasi constant. This effect can be explained using equation (2.8); the aerosols absorb only a little part of the irradiance ($\alpha \approx 0$) while a significant part is backscattered. Thus, the low transmittance is directly related to high backscattering. The Rayleigh scattering in the smallest wavelengths even amplifies this effect: the reflected radiance at the sensor level is maximal in this range although – or in fact because – the atmospheric transmittance is very low.

2.4 Atmospheric Signature of Water Vapor

Water vapor is the main absorbing constituent of the atmosphere besides the aerosols. The solar spectrum observed at the ground is highly influenced by the signature of water vapor which dominates more than half of the solar irradiance wavelength range. Figure 2.7 shows the atmospheric transmittance curve for water vapor with the most important bands.

The absorption process is caused by the vibrational states of the water vapor molecules. Rotational effects occur only in the thermal infrared while electronic transition absorption is observed in the ultraviolet part of the spectrum [31]. The absorbed energy is mainly emitted in the thermal infrared and is used for water vapor detection by common meteorological sensors (see Figure 1.1 on page 2). The atmospherically obscured parts of the spectrum are not completely useless for remote sensing: the features in the near infrared part of the spectrum (e.g.) can be evaluated for cloud detection since only the reflected radiance of high level targets reaches the sensor [25].

Water vapor is detected in bands of moderate absorption. The suitable bands

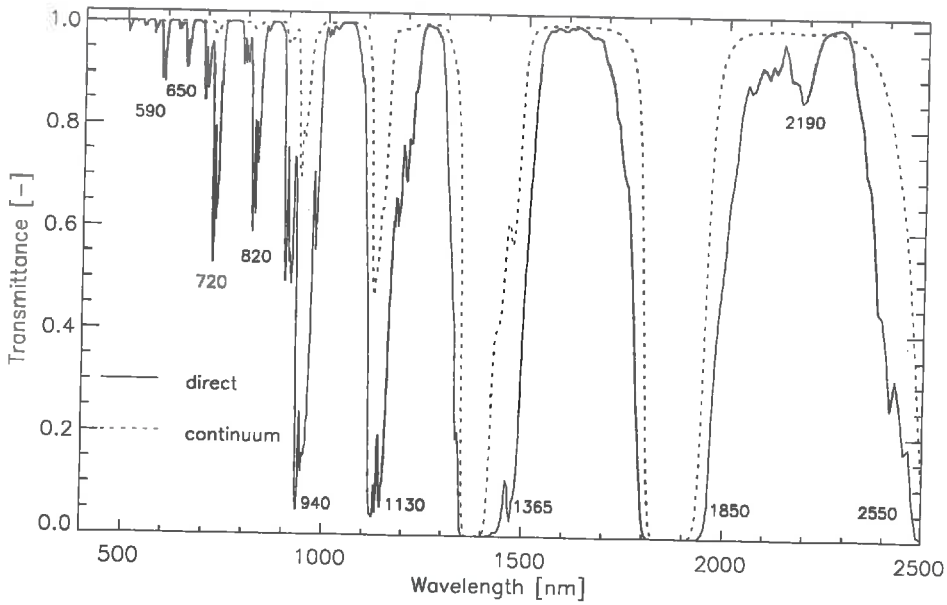

Figure 2.7: Water vapor direct transmittance over the common imaging spectroscopy wavelength range. The most important absorption bands are depicted by their highest absorption wavelengths. The water vapor continuum curve describes the hull of the highest possible transmittance values at best spectral resolution [MODTRAN simulation].

vary according to the amount of water vapor in the atmosphere (a method to detect the best suited spectral regions is derived in Section 5.1 on page 63). The direct transmittance will be used to relate the absorption strength to a water vapor amount.

Figure 2.8 shows the difference between direct transmittance values (simulated directly along the optical path) and apparent transmittance values (simulated by relative absorption for at-sensor-radiance as described in Equation (2.13)). The apparent transmittance in the absorption feature is increased if the atmospheric radiation is not separated for the transmittance calculation. The reason for this effect is a shortage of the optical path by direct backscattering of the atmospheric radiance to the sensor what results in increased transmittance values for this part of the radiance. A subtraction of the atmospheric radiance term from the total radiance leads to a simulated transmittance curve, which is very close to the direct transmittance. The radiance values thus can be related to the direct transmittance which permits the link of radiance measured at the sensor level to the absorption signature of water vapor. The impact of this linking procedure is higher than expected; an extensive analysis of partial atmospheric correction procedures for differential absorption techniques is shown in Chapter 5.

The total water vapor column in the atmosphere varies strongly worldwide.

It ranges from almost zero at high altitude stations and in polar regions, and up to 4 cm in tropical climates. The single standard atmospheres given in the radiative transfer codes represent a wide variety of water vapor content which is given in Table 2.2. This standard situations have to be used for radiance simulations if no in-situ values are available.

Atmosphere	Water Vapor [kg/m^2]	Ozone column [g/m^2]	Ground Pressure [hPa]	Ground Temp. [°C]
Tropical	41.98	5.43	1013.0	26.85
Midlatitude Summer	29.82	6.95	1013.0	20.85
Subarctic Summer	21.20	7.50	1010.0	13.85
US Standard	14.39	7.48	1013.0	14.95
Midlatitude Winter	8.67	8.64	1018.0	-0.95
Subarctic Winter	4.23	10.40	1013.0	-16.05

Table 2.2: Integral characteristics of the McClatchey standard atmospheres, as stored in MODTRAN [44].

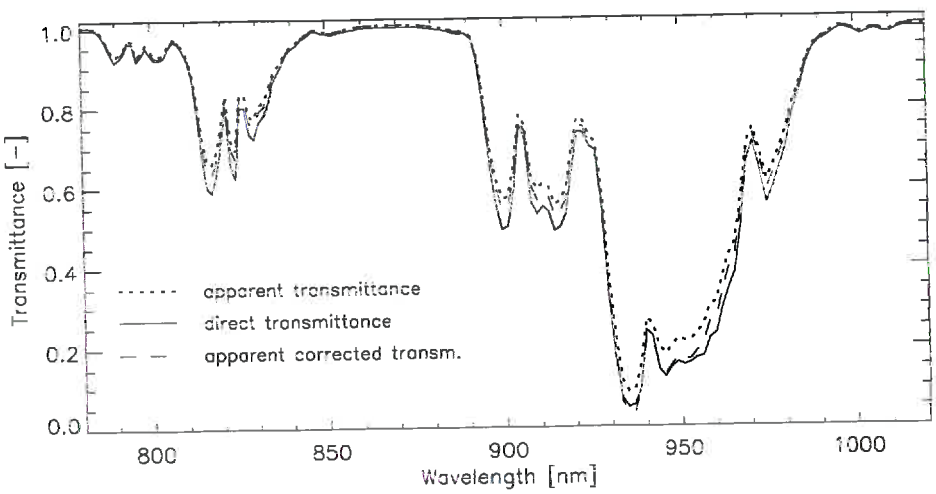

Figure 2.8: Comparison of direct and apparent (radiance simulated) transmittance in the 940 nm water vapor absorption band. The correction of the atmospheric radiance allows the relation of the apparent transmittance to the direct transmittance values [MODTRAN simulation].

2.5 Signatures of Various Atmospheric Gases

The main secondary gaseous absorbers between 0.4 and 2.5 µm are ozone, oxygen, carbon dioxide and methane. Carbon monoxide and nitrogen only have insignificant absorption features in this wavelength range (HITRAN, [58]).

Table 2.3 shows a compilation of the main absorption features of these additional atmospheric gases. Most of these absorption feature are very narrow or of low significance. Thus, the analysis of these features requires high performance sensors with a high spectral resolution. Oxygen could be exploited using the narrow 760 nm absorption feature while the best results for carbon dioxide could be achieved using the absorption feature just above 2 µm. The Chappius band of ozone was exploited in an earlier work [65]. The weak absorption only allowed qualitative results over homogeneous backgrounds such as over water. The technique was not further investigated due to the low significance of the observed signal.

Gas	Position [nm]	Strength [Transmittance]	Width [nm]
Oxygen	687	0.83	687-689
	760	0.63	760-768
	1268	0.93	1262-1269
Carbon dioxide	1601	0.96	1599-1611
	2004	0.39	1999-2008
	2055	0.73	2050-2071
Ozone	574	0.986	550-640
	602	0.985	
Methane	1666	0.94	1665-1667
	2276	0.93	2221-2310
	2317	0.90	2316-2320

Table 2.3: Position and strength of selected strong absorption features of various atmospheric gases [MODTRAN simulation].

Imaging spectroscopy of methane could be interesting for global observations since methane is the second strongest forcing gas for the greenhouse effect in the atmosphere. The absorption features between 2.2 and 2.3 µm could help to monitor the distribution of this absorber.

The strength of the absorption features of N_2O and CO is too low to allow a gas detection by means of imaging spectroscopy. N_2O has a weak absorption line at 2.25 µm which interferes with the stronger CO_2 absorption in this wavelength range. The absorption of CO at 2.33 µm is less than 1% and thus cannot be used for CO detection if the current noise and error levels for current sensors of up to 5% are considered.

2.6 Conclusions on Atmospheric Signatures

The influence of the atmospheric constituents on the radiance at the sensor were described and quantified by using radiative transfer codes and basic radiometric laws. A way to relate the observed radiance values at a sensor to the specific columnar amounts is proven to be possible by extracting the atmospheric transmittance for a specific constituent out of the observed radiance values.

The signatures which could be utilized by means of imaging spectroscopy are those of water vapor and aerosols, while the features of ozone, carbon dioxide and methane are less relevant. This work, although focused on water vapor, has to deal with aerosol effects due to the strong impact of the aerosol signatures on the observed radiance and the intermixed signals observed in the water vapor absorption features.

The derived laws will mainly be used for the evaluation of sun photometer data (see Chapter 3) and for the definition of a water vapor retrieval technique in Chapter 5.

Chapter 3:

Measurement of Atmospheric Properties

3.1 Sun Photometry

Atmospheric correction requires exact information on the optical properties of the atmosphere [28]. Currently, the accuracy of methods to make such measurements is limited. Visibility estimations by human observers in a test area are very subjective and can only be used at an estimated reliability of 50 percent. They also depend on the line of sight since observations in the forward scattering direction (looking in the direction of the sun) are much more affected by the atmosphere than observations in the backward scattering direction. Radiosonde measurements on the other hand can only provide data on atmospheric gases at an accuracy no better than ±10%. The measurement of aerosol is not possible at all using radiosondes.

Sun photometry basically is a method for determination of the solar irradiance at the ground over a certain period. The irradiance values can then be trans-

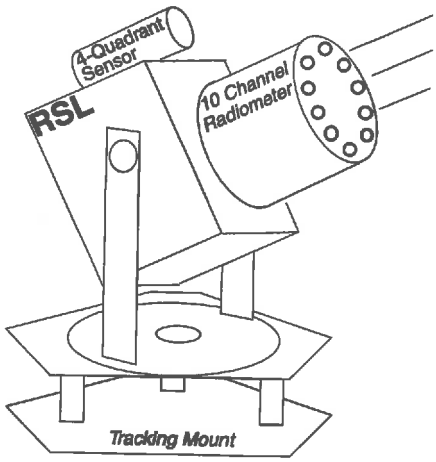

Figure 3.1: Schematic view of the Reagan 10 channel sun photometer (radiometer head without tripod and data logger).

formed to atmospheric optical thickness in a number of channels. These data allow estimation of the amount of water vapor, ozone or aerosols, as well as determination of the aerosol particle size distribution. The data can be inverted for the ground visibility which is an important tuning factor for atmospheric models.

3.1.1 The Reagan Sun Photometer

The Reagan sun photometer is a sun-looking, ground based instrument for atmospheric measurements. It is mainly used as an atmospheric ground truthing instrument in field campaigns [21].

Specifications:

- 10-channel parallel co-aligned tubes with FOV (field of view) ≈ 3.2°
- channels at 382, 410, 501, 611, 669, 721, 780, 872, 940, and 1033 nm.
- narrow band three-cavity interference filters with FWHM (full width at the half maximum) of ≈ 8 to 12 nm,
- digitizing 16 bits,
- RS-232 line driver/receiver,
- temperature stability at ≈ 43 ± 0.5°C by heater control,
- data logger for 2-3 days of data acquisition (32 K byte non volatile RAM)
- automatic sun tracking with four quadrant detector technology, ± 17° tracking capability,
- 12 V power supply or battery for one day of current-independent usage
- average power consumption 15W,
- fully transportable (total weight: ca. 13.5 kg + boxes).

3.1.2 Sun Photometer Calibration

The sun photometer calibration is performed on a high mountain station[1] using the Langley–Plot method. The direct solar irradiance is measured during a morning hour sunrise period at stable atmosphere conditions. These values are then extrapolated to exo-atmospheric conditions to obtain the calibration coefficients. This calibration procedure allows afterwards to calculate the atmospheric transmittance and irradiance directly from the radiometer outputs.

The Langley Plot Method

The ability of the instrument to measure the solar irradiance during a diurnal period makes the application of the Langley plot calibration technique possible. This technique was applied for the calibration of solar looking radiometers in various studies ([23], [68], [69], [73] and [84]) and is based on the following simplified irradiance model:

$$E = E_0 e^{-\tau_0^* m} + E_{dif}, \tag{3.1}$$

1. The calibration runs in this study were done on Jungfraujoch and Weissfluhjoch, both located in the Swiss Alps.

where E_0 is the extraterrestrial solar irradiance, E_{dif} is the diffuse irradiance and τ_0^* is the vertical optical thickness of the atmosphere. The relative optical airmass m describes the ratio of the optical thickness for a tilted line of sight and the vertical optical thickness. The sun photometer only measures the direct irradiance, while tracking the sun automatically. Its field of view is only slightly larger than the angular size of the sun. Thus E_{dif} can be set to zero and equation (3.1) is reduced to a linear expression:

$$\ln(E) = \ln(E_0) - \tau_0^* m . \tag{3.2}$$

A linear relationship between irradiance and sun photometer data response is assumed for the measured output voltage $V = gE$ (where E is the irradiance and g is a gain factor). The dark current of the instrument is well below 1% of the signal and is therefore neglected[2]. The extraterrestrial irradiance E_0 which is the source term of the measured irradiance, is dependent on the square of the relative sun-earth distance R_S (in astronomical units) and thus on the day of the year. The calibration constant V_0 is defined as the measured voltage above the atmosphere for the average sun-earth distance ($R_{S,0} = 1$ AU). The conversion of the irradiance to the calibration constant therefore is given as:

$$V_0 = E_0 g R_S^{\,2} \quad \text{from} \quad E_0 = \frac{V_0}{g R_S^{\,2}} . \tag{3.3}$$

The calibration constant V_0 may then can be calculated using Beer's relationship (3.2)[10]. This leads to the equation

$$\ln(V) = \ln\left(\frac{V_0}{R_S^{\,2}}\right) - \tau_0^* m . \tag{3.4}$$

The calibration constant for a sun photometer channel is now derived by plotting $\ln(V)$ against the airmass m. The intercept at $m = 0$ is extrapolated from the daily variation of the relative airmass during a clear sunrise period. Its value then is used to solve for the calibration constant whereas the slope is an average daily value for the optical thickness of the atmosphere:

$$V_0 = V_{m=0} R_S^{\,2} \quad \text{and} \quad \tau_0^* = -\frac{\partial(\ln(V))}{\partial m} . \tag{3.5}$$

3.1.3 Airmass Calculation

The relative airmass is defined as the optical path of a ray through the atmosphere divided by the optical path of a zenith looking ray at sea level conditions. As long as the atmospheric refraction is neglected (assuming a straight path through the atmosphere), the relative airmass calculation reduces to:

2. The dark current is corrected in the Reagan sun photometer by internal software.

$$m = \frac{1}{\cos(\theta_e)} \frac{p}{p_0}. \tag{3.6}$$

The pressure quotient accounts for the height above sea level. The astronomical (pure geometric) sun zenith angle θ_a can be calculated from astronomical procedures. The extraterrestrial zenith angle θ_e is calculated from θ_a with respect to a time delay of the sunlight from the sun to earth of about 8.3 minutes (depending on variations in the earth-sun distance). Finally, the observed zenith angle θ_g is derived using Snell's law:

$$n_e \sin(\theta_e) = n_g \sin(\theta_g), \text{ with } \quad n_e = 1. \tag{3.7}$$

The refractive index n_g is derived using equation (2.17), based on surface temperature, pressure and humidity. A more sophisticated airmass calculation was defined by Kasten and Young([39], [84]). They have defined an airmass model with consideration of the refractive path of the light through the atmosphere for given θ_g or θ_e, respectively:

$$m = \frac{1}{\sin(\theta_g) + a_1(\theta_g + a_2)^{a_3}}, \tag{3.8}$$

with the empirical constants:
a_1 =0.50572, a_2 =6.07995° and a_3 =-1.6364.

More accurate methods are used in the radiation transfer codes like MODTRAN. They calculate mainly the refraction in each layer of the atmosphere, and add the single path length to a total optical path value. According to Schmid [68] Kasten's model is sufficient for Langley plot analysis in an error range of below 1%.

3.1.4 Modified Langley Plot

The calibration procedure described in the above section only yields satisfactory results for sun photometer channels outside atmospheric absorption bands. The calibration inside the bands has to be performed using information from irradiance simulations (with MODTRAN) and on aerosol scattering from the adjacent channels. This leads to a modified Langley approach with the following assumption for the water vapor optical thickness:

$$\tau_{wv}^{*} = k(m \cdot PW)^b = k(PW)^b m_{wv}, \tag{3.9}$$

where k and b are empirical constants. The proposed values by Bruegge et al. [10] are k = -0.655 cm^{-1} and b = 0.57, respectively. The analysis of MODTRAN simulations have shown values of k = -0.577 cm^{-1} and b = 0.626, respectively. The absolute value of k also includes a factor for the unit of the output, while b only depends on the strength of absorption. The values are derived from an inversion of MODTRAN runs under varying atmospheric conditions (see also Section 6.1

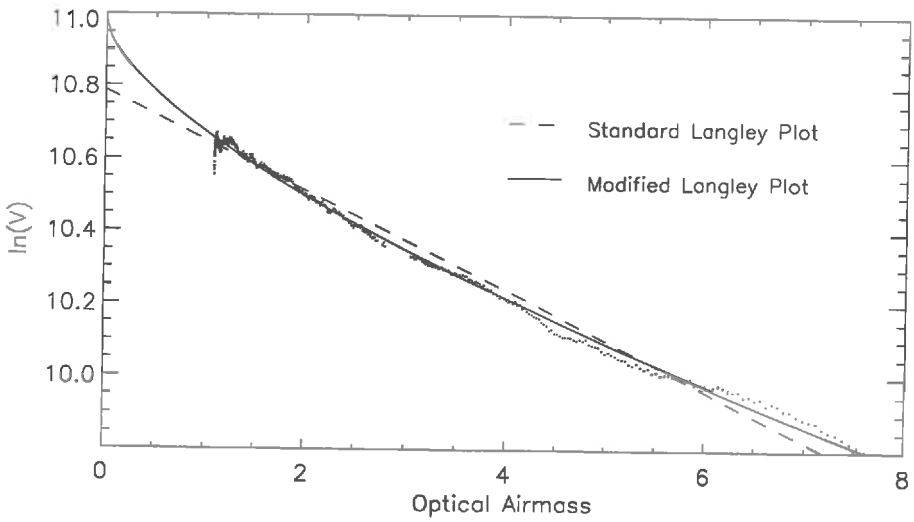

Figure 3.2: Comparison of a Langley and a modified Langley plot for the 940 nm water vapor absorption band (see text). The instrument response for the modified Langley plot is not linear with optical airmass.

on page 89 for a detailed description of such a procedure).

The precipitable water vapor column (PW) is integrated along a vertical path. Thus, the relative optical airmass can be used to obtain the relevant amount of water vapor in the (tilted) optical path, such that $PW_{tilt} = m \cdot PW$. The effective optical airmass for water vapor then is defined based on equation (3.9) as $m_{wv} = m^b$. The total optical thickness then is a summation of water vapor and aerosol optical thickness τ^*_{dif}. Thus, the Langley calibration equation changes to:

$$\ln(V) = \ln\left(\frac{V_0}{R_S^2}\right) - \tau^*_{dif,\,0} m - \tau^*_{wv,\,0} m_{wv}, \text{ and} \tag{3.10}$$

$$\ln(V) + \tau^*_{dif,\,0} m = \ln\left(\frac{V_0}{R_S^2}\right) - \tau^*_{wv,\,0} m_{wv}. \tag{3.11}$$

The calibration constant V_0 is now obtained by plotting the left hand side of equation (3.11) against the water vapor airmass equivalent m_{wv}. The aerosol optical thickness $\tau^*_{dif,0}$ is calculated in the adjacent channels which are not influenced by water vapor, using the regular Langley plot method. The two values of optical thickness are then interpolated to the centre of the 940 nm sun photometer channel.

Figure 3.2 shows the effect of the modified Langley plot calibration on the determination of the calibration constant. The single values (dots) are much bet-

ter represented by the modified interpolation curve which is no longer in linear relationship to the optical airmass. The resulting calibration constants exceed the values obtained by the regular Langley plot technique systematically.

3.1.5 Calibration Results

Based on the above procedures, a set of three calibration experiments was analyzed. The first data set was provided by the manufacturer of the instrument, while the other two calibration campaigns were performed at high altitude stations in Switzerland (see also Figure 3.3). A summary of the single campaigns follows below:

a) Mount Lemmon 1995

A set of calibration constants was provided by the manufacturer from the University of Arizona. The constants were derived in November 1995 at the high altitude station Mount Lemmon, close to Tuscon (AZ, USA). A total of three runs could be provided at very stable atmospheric conditions in a desert climate. The columnar water vapor amount was very low at 0.5 to 2 mm. This calibration provided reliable constants at an RMS-deviation of 1–4% between the single runs.

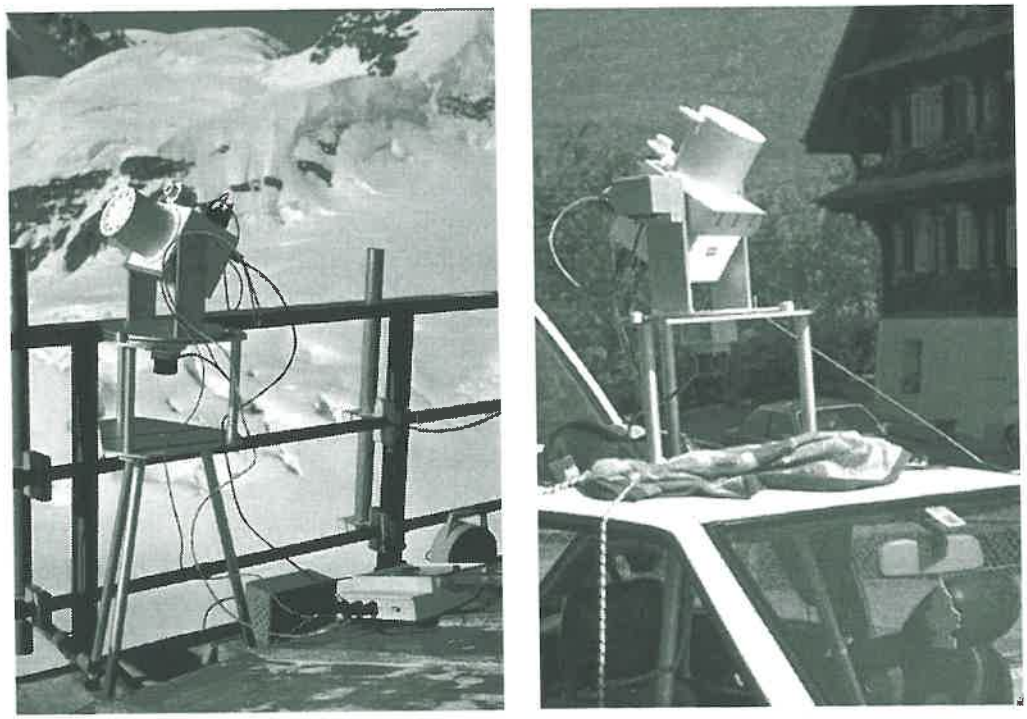

Figure 3.3: The Reagan sun photometer during a calibration run on the alpine research station Jungfraujoch (left) and mounted on top of a car during a field campaign (right).

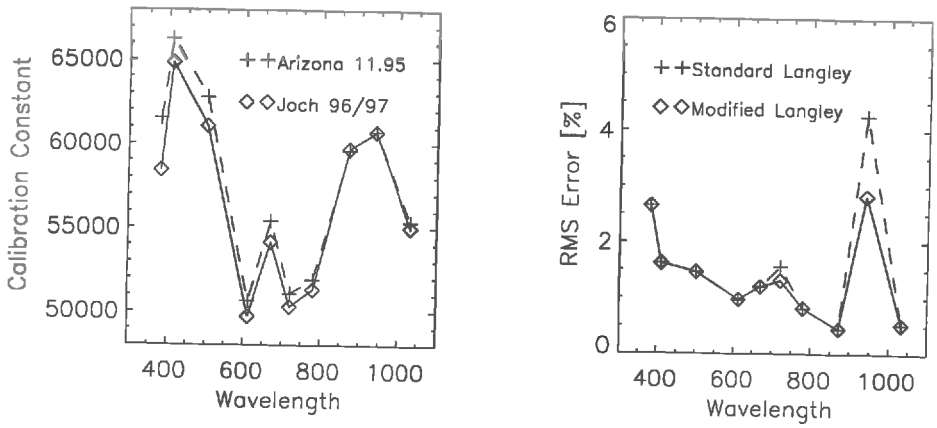

Figure 3.4: **Left: calibration constants for 1995 and the average of the 1996/97 calibration runs. There seems to be an effect of sensor degradation in the short wavelength channels. Right: RMS variation of all calibration runs between 1995 and 1997 for standard Langley plot method and modified Langley plots.**

b) Jungfraujoch 1996

The calibration at the alpine research station Jungfraujoch was performed between June 10th and 13th, 1996. The conditions during these days were not optimal:

- *10th*: Cloudy weather does not allow a complete calibration run.
- *11th*: The first calibration runs under convective weather conditions. The results show that this run cannot be used for an appropriate calibration due to advective fog.
- *12th*: The run is started very early in the morning under better conditions than on the 11th. There is still some convection left, but the data are usable. It is nevertheless not possible to go beyond a rejection limit of 1% variation against the Langley plot line.
- *13th*: Since there were some clouds left in the morning from the previous day, the run could only be started at 10 am. The span in optical airmass from then until midday is too low for an exact calibration.

Only one sufficient Langley plot could be created after these four days of operation. The high altitude station (3580 m.a.s.l) was not high enough to prevent influences of advective clouds during the calibration days at the beginning of summer. The water vapor column was still about 3mm, despite the height above sea level. The influence of this residual humidity had to be corrected by the modified Langley plot (see Figure 3.2) for the two water vapor absorption channels.

c) Weissfluhjoch 1997

The second high altitude campaign was performed on January 30/31st 1997 at the Swiss Federal Institute for Snow and Avalanche Research, Weissfluhjoch, Davos. The altitude of about 2430 m.a.s.l was well above the winter atmospheric inversion layer. Both runs provided consistent calibration constants which also did not vary significantly from the results of the Jungfraujoch campaign. The water vapor column was at about 0.5 to 1 mm. These dry conditions are common for winter atmospheres. The variations in water vapor indicates how stable the atmosphere was (see Figure 3.5). The dry conditions helped to obtain good results. This fact leads to the recommendation to favor late fall or winter calibrations against summer calibration runs.

Conclusions on Sun Photometer Calibration

The calibration constants of the latest runs were decreased against the Mount Lemmon calibration of October 1995 by 1–3%. This can be explained by sensor degradation. Such changes of the sensor response (and calibration constants) are the reason why calibration runs have to be made at regular time intervals on a yearly basis.

Another key factor, and possible source of errors for the calibration results, is the method of processing. There are several options to evaluate the Langley plot and to do the airmass calculation, of which only one way is described above. The calibration constants may change within 1–2% due to systematic errors in the calculation. And even the differences in calibration constants, attributed to sensor degradation could be artificial effects due to calculation uncertainties.

The relative error of the calibration constant was not derived analytically because information on initial errors of the instrument characteristics is unknown. The variation in solar irradiance during the period was below 0.1% within the two years and therefore is not a main contributor to the total change of measured signal[3]. An estimate of the error was made by calculating the RMS variation of the six final calibration runs against its mean. Figure 3.4 shows the results. The RMS variation is below 2% for most of the sun photometer channels. This variation is almost below the errors which can be achieved with laboratory calibration [61].

The modified Langley approach reduces the RMS variation in the water vapor channel. This improvement is independent of the reduction of the systematic error. The modified Langley plot systematically increases the calibration constants between 5–15% against results obtained with the standard Langley calibration in the 940 nm water vapor band.

The results of the calibration do not depend on any knowledge about the solar irradiance. This fact is important since the solar spectrum is not known to better accuracies than 2–4%[4] for some parts of the electromagnetic spectrum

3. C. Fröhlich, World Radiation Centre, Davos (CH), personal communication

(this despite the fact that the sun can be assumed to be a constant source). The instrument is directly calibrated based on the optical depth of the atmosphere, assuming a consistent extraterrestrial constant. The derived 'solar constants' therefore are only valid for the investigated instrument.

3.2 Applications of Sun Photometer Data

3.2.1 Water Vapor Measurement

Sun photometer measurements can be used for the monitoring of the water vapor column abundance in continuous operation over the year or during special measurement campaigns. The absorption in the 940 nm water vapor band of the irradiance is related to the water vapor amount using equation (3.9). The equation of the modified Langley plot is inverted to:

$$PW = \left[\frac{\ln \tau_{940} - \ln \tau_{940,\,ae}}{-k \cdot m^{b}}\right]^{\frac{1}{b}}, \qquad (3.12)$$

where k and b are the constants described in Section 3.1.4. The transmittance in

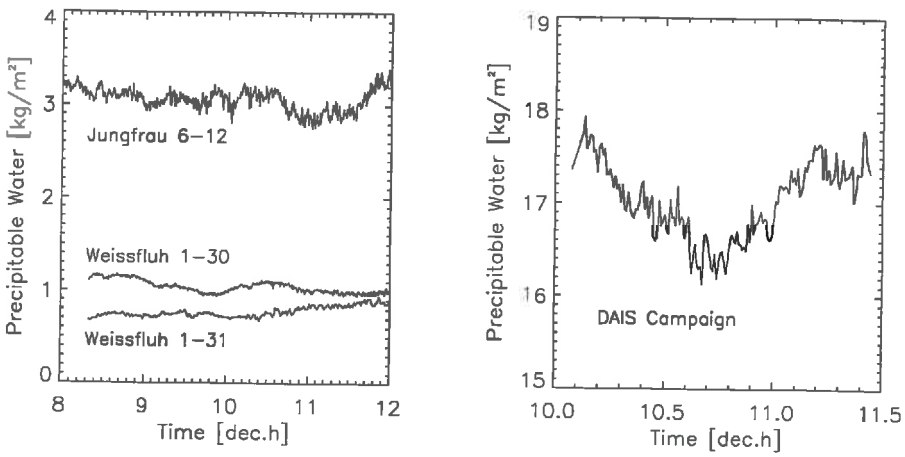

Figure 3.5: **Precipitable water measurements for high altitude calibration campaigns (left) and a regular field experiment in summer 1996.**

4. B. Schmid, NASA Ames (CA), personal communication, derived by comparison of extraterrestrial solar irradiance measurements

the 940 nm channel (τ_{940}) is derived by a pure division of the measured digital numbers against the calibration constant. Such calculation is performed also for the two adjacent sun photometer channels at the central wavelength positions of 872 nm and 1033 nm, respectively. The interpolated aerosol transmittance in the 940 nm absorption band then is calculated as:

$$\tau_{940,\,ae} = w_1\tau_{872} + w_2\tau_{1033}, \tag{3.13}$$

where w_1 = (1033-940)/(1033-872) and w_2 = (940-872)/(1033-872) (with numbers from the channel wavelengths in nm). The band weighted average of the adjacent channels is also known as a continuum interpolation. It reconstructs the aerosol transmittance at the centre band position. Such an interpolation allows the calculation of the differential absorption of the water vapor in relation to the irradiance for a totally dry atmosphere. The technique is therefore similar to the methods depicted in Chapter 5.

This method is applied to the calibration runs described in the previous section. It reveals the relative stability of the atmosphere in response to water vapor (see Figure 3.5). Only small variations are reported which are independent of the amount of aerosols (the aerosol optical thickness was quasi constant for the depicted time intervals). The instabilities during regular campaigns are much higher, with variations of up to 1 mm precipitable water within 10 minutes (see e.g. Figure 3.7).

The comparison between aerosol optical thickness and water vapor amount on diurnal measurements (as shown in Figure 3.7) illustrates that the above procedure distinguishes clearly between the two atmospheric constituents. The variations in total optical thickness due to cirrus clouds (afternoon variations) are not reported in the water vapor results. The differential method for water vapor retrieval thus corrects for the influence of aerosol scattering.

Comparison with Radiosonde Atmospheric Profiles

A special experiment was set up in Central Switzerland to compare sun photometer measurements at varying altitude with a simultaneous radiosonde launch. The photometer was mounted on top of a car (see Figure 3.3) and moved from a starting altitude of 490 m to a final one of 1030 m.a.s.l. Eight measurements, of 10 minutes duration each, were taken in height intervals of about 80 meters. The time difference from the first to the last measurement was two hours. A radiosonde (see Section 3.3) was launched from the starting point location half an hour prior to the start of the campaign. Figure 3.6 shows the results of the measurements. Except for the values above 900 m the integrated columns of the radiosonde are substantially higher than the inverted water vapor content from the sun photometer measurements. However, above 900 m the values agree within 0.3 kg/m^2.

The reasons for this difference are hard to find since both the sun photometer and the radiosonde have their disadvantages and uncertainties. On the side of the sun photometer, the time difference between the single measurements is the main

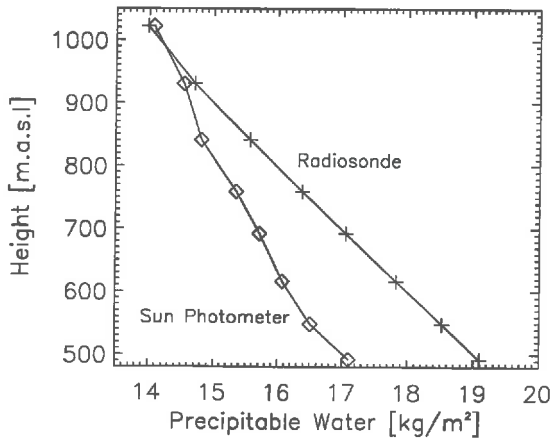

Figure 3.6: **Comparison of height dependent sun photometer measurements and an integrated radiosonde profile.**

problem. The atmosphere can vary very strongly within the total time of about 2 hours. The quantity of such variations often may reach 10 to 20% per hour, as indicated by the measurements shown in Figure 3.5. Moreover, the relocation of the sun photometer was within a horizontal distance of 4 km. The horizontal variations of water vapor in such rugged terrain may be very high within this distance and could have caused the observed difference.

The radiosonde measurements on the other side have to be integrated over height at a possible measurement error of about ±10% (see Section 3.3). This error persists with integration over height, and would only be reduced if it is of statistically distributed nature.

3.2.2 Aerosol Measurement

One main application of sun photometer measurements is the monitoring of the aerosol content in the atmosphere. The Reagan instrument offers seven out of 10 channels suited for aerosol retrieval. The aerosol optical thickness τ_{ae}^{*} is retrieved from calibrated transmittance data by inverting Beer's law (3.1). The amount of aerosols can then be derived by applying the specific extinction coefficients. However, the retrieval of aerosol content was not a major goal of this work. For the application of sun photometry for atmospheric correction and water vapor retrieval it is sufficient to know the aerosol optical thickness τ_{ae}^{*}.

Figure 3.7 depicts an example of the diurnal aerosol optical thickness variation in

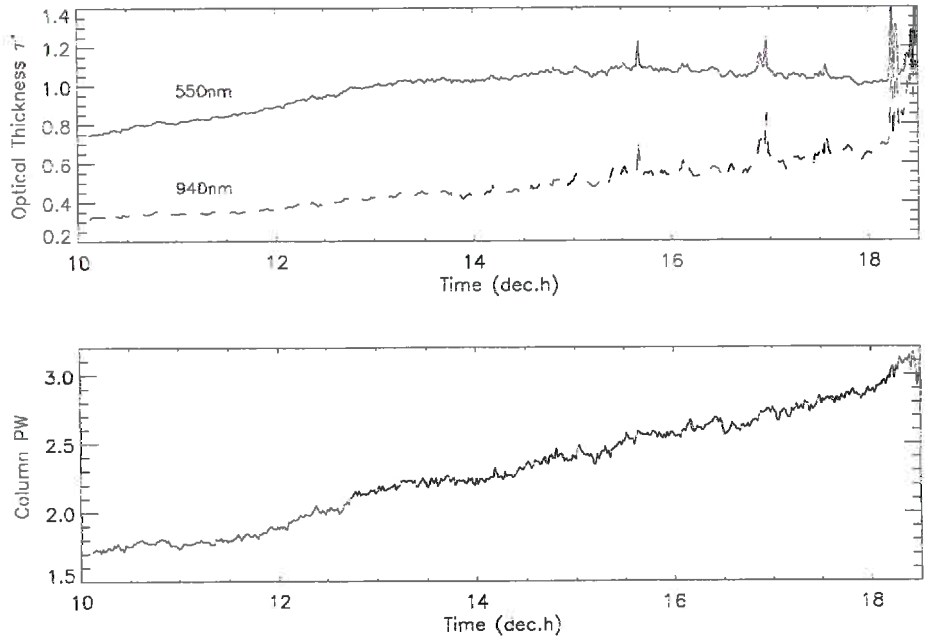

Figure 3.7: Variation of the optical thickness due to aerosols and due to water vapor, measured during the VOTALP experiment [24], August 1996.

comparison with the increasing water vapor contents over the day. Singularities in the aerosol signature occur when for example thin cirrus clouds absorb in the optical path.

Another parameter which potentially can be retrieved is the Ångström coefficient (a). It indirectly describes the aerosol size distribution and is derived by a best fit of the optical thickness values to the function $\tau^*_{ae}(\lambda) = k\lambda^{-a}$. The constant k then accounts for the total amount of aerosols whereas a only depends on the aerosol size distribution. More sophisticated methods for the retrieval of aerosol size distributions [42] use a single value decomposition to derive the spectrum of the scattering aerosol sizes.

Visibility determination

A critical factor often used for the description of the optical state of the atmosphere is the visibility. It is defined as the maximum horizontal distance at which a bright target can be distinguished from a dark one by an human observer. This definition leads to very inaccurate estimates of the visibility during field campaigns. The estimated values depend on the observers recognition, but also on the viewing direction; lower values of visibility are reported when looking in direction of the sun due to the strong forward scattered radiation, whereas too high

visibilities are observed in the opposite direction of the sun.

An easy conversion allows the definition of visibility based on the vertically measured optical thickness. It is achieved by the empirical equation (as seen in [44]):

$$l_{vis} = \frac{3.914}{\tau^*_{550}}. \tag{3.14}$$

This visibility is based on the (aerosol) optical thickness at 550 nm (τ^*_{550}) and can be calculated directly from measured values of optical thickness with the sun photometer. The value is interpolated from adjacent channels if no data at 550 nm are available. This method does not consider variations of the aerosol model, or of other atmospheric parameters. It therefore can only be used for a fast estimation of visibility.

A more accurate method for visibility retrieval is the direct inversion of the MODTRAN model. The horizontal visibility can be given as a variable input parameter to transmittance simulation runs at given geometric and atmospheric conditions. This leads to a look up table of visibility against transmittance. The transmittance can then be directly introduced from the calibrated sun photometer measurements, resulting in an interpolated range of visibility, valid for the investigated situation.

3.3 Radiosonde Measurements of Water Vapor

The direct measurement of the atmosphere is traditionally made by launching radiosondes. The standard instruments on a radiosonde unit are a barometer, a thermometer and a hygrometer. Some units also carry sondes for ozone and other gases. The accuracy of such measurements is good for pressure and temperature whereas mediocre accuracies are achieved for gases and aerosols. However, the radiosondes are the only practical way to get in–situ data of the atmospheric properties including the layering, and therefore have to be used to evaluate other measurement methods. Various types of sondes are in use by the different meteorological services, private organizations and the army. Their balloons can reach heights of up to 30 km. For remote sensing applications, the height of the tropopause at 12 to 14 km is usually sufficient. The accuracy in relative humidity is about ±10% for high humidity and decreases for low water vapor concentrations[5]. Nevertheless, the accuracy given by the producer is better than 5% for relative water vapor concentration [71].

The comparison of radiosonde technique and solar radiometry shows that sun

5. J. Keller, PSI, Villigen (CH), personal communication

photometer measurements have some advantages over radiosondes (see Table 3.1). However, the sounding units allow high vertical resolution and are commonly used in meteorological networks. The availability of radiosonde data for operational remote sensing therefore is given by the meteorological organizations of each country, while the sun photometer measurement network is not yet established in most of the countries.

Radiosonde	Sun Photometer
in situ, chemical method	indirect, radiometric method
operational network	partly operational network
expensive single measurements	extensive data processing necessary
complicated handling	easy setup
atmospheric layering information available	only integral (columnar) information
rel. accuracy range *PW*: ±10-15%	rel. accuracy range *PW*: ±5-10%

Table 3.1: Comparison of radiosonde and sun photometer technique for the retrieval of the columnar water vapor content.

3.3.1 Integration of Precipitable Water from Radiosonde Data

The amount of water vapor as measured by the radiosonde is usually derived from the relative humidity at various height levels. For remote sensing applications, the optically relevant amount is given in columnar mass [kg/m^2] which for water is equivalent to one millimeter columnar water vapor (given a density of 1000 kg/m^3 for water). The centimeter column is widely established for quantification of the precipitable water vapor column and is therefore also used in this study.

The first step of the transformation from relative humidity H [%] to columnar water vapor is the calculation of the density of the water vapor in air. The partial pressure is defined as:

$$p_{part} = \frac{H}{100} e_s(T) \tag{3.15}$$

where e_s is the saturated vapor pressure, given by equation (2.18) on page 12. If the partial pressure is known, the density of water vapor can be calculated using the law for ideal gases as

$$\rho_{wv} = \frac{M_{wv} p_{part}}{R \cdot T}, \tag{3.16}$$

where M_{wv} is the molecular weight of water vapor and R is the ideal gas constant.

Thus, the density only depends on the air temperature and the relative humidity

Figure 3.8: The mobile radio sounding unit, in operation during field campaigns (system in courtesy of the Paul Scherrer Institute PSI).

which both are measured simultaneously by the radiosonde.

The columnar precipitable water vapor PW can now be integrated from the starting altitude h_0 with height:

$$PW = 0.1 \int_{h_0}^{\infty} \rho_{wv} dh \,. \tag{3.17}$$

The factor 0.1 originates from the conversion of kg/m^2 to centimeters column. Equation (3.17) is integrated numerically for a specific radiosonde.

Figure 3.8 depicts the setup of the mobile radiosonde unit. A balloon of about 1 m diameter at ground level carries the sounding unit which is attached 8 meters below the balloon. The flight is tracked from the control unit which is located in the van. The balloon blasts at an altitude of about 20 to 30 km, while the sounding unit drops by parachute. The measurement unit is reusable.

3.4 Applicability of Atmospheric Measurements in Remote Sensing

Radiosonde data is mostly used for the validation of instrument calibration, of atmospheric transfer codes, or of atmospheric processing techniques. It therefore is an experimental and research based technique which is seldom used in operational remote sensing. An example of a method evaluation with radiosondes has already been shown in Figure 3.6. The integral amounts there were used for the evaluation of the water vapor retrieval technique for sun photometry.

The amounts of columnar water vapor can also be taken to evaluate the quantification results of remote sensing techniques. Problems arise because the radiosonde measurement cannot be referred to a single image pixel for remote sensing because the balloon may be dislocated by the winds. Another problem is the undefined precise time of the columnar measurement since one launch can last up to one hour from the ground to the top of the troposphere. However, the radiosonde measurements have to be considered, because they use a principally different technology than sun photometers and other radiation based instruments.

Another important parameter in remote sensing is the aerosol distribution within the atmosphere. The aerosols are not yet measured by common radiosondes and still have to be estimated from other sources. The in-situ retrieval techniques are only of limited reliability since it is technically challenging to collect and measure the full range of aerosol sizes in appropriate time intervals[6]. Therefore, the aerosol amount in the atmosphere still has to be modeled using the radiative transfer codes together with the knowledge about the layering of the atmosphere and the general geographical conditions.

Sun photometry gathers integral information on the aerosol size distribution. Similar techniques could be developed for future remote sensing applications. The image results will have to be cross evaluated against one another such as for water vapor applications.

However, the main application of the described techniques is atmospheric correction and in-flight validation of optical remote sensing instruments. The atmospheric measurements help to understand the nature of the signal at the sensor and to evaluate various processing and calibration techniques.

6. B. Schmid, NASA Ames (CA), 1998, oral presentation, University of Bern

Chapter 4:

Imaging Spectroscopy Data Preparation

Imaging spectroscopy has been developed as an universal tool for the monitoring of the earth's surface. Current instruments are therefore not constructed primarily for atmospheric applications. The data preparation is common for all application; it includes data exploration, data quality assessment, geocoding, and atmospheric correction. Its significance for atmospheric investigations together with the proposed procedures for airborne imaging spectrometer data will be shown in this chapter.

4.1 Imaging Spectroscopy of the Atmosphere

Most of the imaging spectrometers cover spectral regions, where the atmospheric signal is dominant (mainly, because 'true' spectrometers measure the continuous spectrum). The high spectral resolution of the data allows the quantitative retrieval of various atmospheric information, and the spatial resolution of down to 10 m is substantially better than for traditional atmospheric monitoring systems (see also the comments in the Introduction).

The end-users' main interest in imaging spectroscopy data for the atmosphere is the promise to correct for atmospheric effects. As already shown in Section 2.3 on page 14, aerosols are the main absorbers and scatterers, followed by atmospheric water vapor. If both of them could be estimated from the image itself, atmospheric correction procedures would be improved significantly.

The monitoring of atmospheric properties themselves, on the other hand is not a main interest and is only relevant if satellite based imaging spectroscopy systems would cover the earth on a daily basis. Applications for airborne systems would include monitoring of air pollution over large cities and research of local air transport processes.

4.1.1 Spectral Resolution

For aerosol retrieval a spectral resolution of about 30 nm is sufficient to cover the atmospheric windows where only the scattering processes of the atmosphere interfere with the ground-reflected signal (see Figure 2.6 and Figure 2.7). These figures also show that most of the channels of a continuously measuring spectrometer are affected by gaseous absorption, especially by water vapor.

Current imaging spectrometers are able to register images at a nominal spectral resolution of 6 to 30 nm. This allows for use of spectral features with a width down to 10 nm as long as the band center positions are not customized for the specific feature. Water vapor has very broad bands. Hence, it is even possible to measure with 30 to 50 nm resolution instruments. Conversely, the oxygen has very narrow absorption bands which can only be recovered by instruments of 10 nm bandwidth or better.

4.1.2 Spectral Range

The typical spectral range of spectroradiometers in the reflective part of the spectrum is from 400 to 2500 nm. Often a choice is made for several spectral ranges to be covered with gaps in between. AVIRIS (airborne visible and infrared imaging spectrometer, [79]) covers the range completely, while other sensors (e.g. DAIS; digital airborne imaging spectrometer, [53]) only measure in selected subranges. For atmospheric applications, the spectral regions below 400 nm are of special interest, because many molecules (especially the ozone) have strong absorption features in the ultraviolet part of the spectrum. Unfortunately, this range is not very useful for land applications and special detectors would have to be used to achieve an acceptable signal to noise ratio. Thus, in the near future this range will still be explored only by non-imaging sounding systems.

Most current operational atmospheric sounding systems use the ultraviolet part of the spectrum. Additionally, emissive lines of the atmospheric gases in the thermal infrared are used for measurement of gas distribution and vertical profiles. The emissive part of the spectrum (i.e. above 2.5 μm) usually is not covered by imaging spectroscopy data. Airborne thermal imaging detectors need cooling and a special optical design (i.e. no common lenses). Therefore, only a minority of imaging spectrometers cover the infrared region (e.g. DAIS, [53]) and only one instrument (TIMS, [55]) was built particularly for imaging the thermal signal in six continuous bands. These bands are not narrow enough to allow the profiling of atmospheric gases. They are therefore mainly used for land surface emissivity retrieval.

4.1.3 Possible Applications

The quality of current imaging spectroscopy data allows good results only for a few atmospheric constituents:

- *Water vapor:* Some differential absorption techniques for the retrieval of

atmospheric water vapor are shown in the next chapters (see Section 5.2 on page 70). Its most investigated absorption features are located in the reflective part of the solar spectrum.

- *Aerosols:* Methods for exact determination of the aerosol content as well as of the aerosol size distribution, are still under development ([3], [36], and [57]). The unmixing problem between the continuous absorption by aerosols and the spectrally variable ground reflectance has to be solved. This is achieved using statistical methods, as well as by inversion of scattering models.
- *Oxygen:* The oxygen feature could be used to obtain terrain dependent height information. First successful attempts were made using the AVIRIS imaging spectrometer [33]. The narrow absorption feature of oxygen can be used only by sensors with a spectral resolution better than 10 nm.
- *Carbon dioxide:* Some first attempts were made to retrieve the carbon dioxide content for the pressure dependent terrain elevation modeling, similar to the oxygen technique [17]. However it is not proven yet, how homogeneous the spatial distribution of CO_2 in dense populated areas is.
- *Ozone:* The weak absorption of ozone in the Chappius band (at 610 nm) was investigated for its usability for imaging spectroscopy by the author [64]. Up to now only qualitative results over homogeneous backgrounds are possible.

4.2 Relevant Imaging Spectrometers

A wide variety of imaging spectrometers is currently available on airborne platforms. Five of them were flown in Switzerland during the last years. First attempts were made in the late 1980's with the FLI/PMI imaging spectrometer prototype. This only allowed a first experience with data of this increased dimensionality. In 1991 the Airborne Visible and Infrared Imaging Spectrometer (AVIRIS) was flown over Central Switzerland and provided a first set of reliable imaging spectroscopy data for alpine regions [62]. Three years later, the DLR (German Aerospace Agency) provided a next data set of the ROSIS imaging spectrometer [29] (unfortunately this data were not calibrated). Starting in 1996, a series of further data sets could be flown with the Digital Airborne Imaging Spectrometer (DAIS) which also was provided by the DLR. This data are of satisfactory quality for land applications. However, its usability for atmospheric remote sensing is limited to aerosol and water vapor retrieval. Another sensor (CASI, [1]) was finally flown in 1997 for limnological application. It has not yet been tested for atmospheric processing.

Table 4.1 shows a comparison between the two most investigated imaging spectrometers in Switzerland, the DAIS and the AVIRIS. Both are still in use and undergo continuous improvements by their maintenance facilities. The AVIRIS has advanced to a kind of 'mother of all imaging spectrometers' because of its high performance over the whole wavelength range and because of the great experience gathered from working on AVIRIS data over the last decade. Its perfor-

mance has not yet been reached by other sensors, and AVIRIS data today are even taken as calibration sources for other instruments, including spaceborne scanners.

The DAIS is one of the few instruments available in Europe for research projects. Its performance in the visible and near infrared part of the spectrum is good, while the short wave infrared region (used for geological applications) is still under improvement. The thermal infrared channels are a speciality of this instrument. They are of interest for energy flux estimations and applications on lakes, although their absolute calibration was not possible yet.

	AVIRIS [79]	**DAIS (GER 7915)** [53]
Owner	NASA	DLR
Maintenance	JPL, Pasadena	OE, Oberpfaffenhofen
Producer	NASA (JPL)	GER Corp.
Year of production	1987	1986
Year of operation	1988	1994
Number of bands	224	79
VIS /NIR range	483-1268 nm (96 bands)	500-1030 nm (32 bands)
SWIR range	1254-2508 nm (118 bands)	1540-1654 nm (8 bands)(1962-2426 nm (32 bands)
Spectral resolution	10 nm	15-30 nm
Bandwidth (FWHM)	9-13 nm	30-50 nm
Infrared range	-	3.0 - 5.0 µm (1 band) 8.7 - 12.1µm(7 bands)
Type	Whiskbroom	Kennedy Whiskbroom
SNR (data provider)	500-1000	30-150
SNR (flat field)[1]	50-200	5-150
FOV	± 15°	± 26°
IFOV	1 mrad	3.3 mrad
Nominal pixel size	20 m	4-6 m
Nominal flight height	20 km a.s.l.	3-4 km above ground
Quantization	16 bit	15 bit
Pixels per line	614	512
Lines per scene	512 (cut)	1900-2700

Table 4.1: Comparison between the AVIRIS and the DAIS imaging spectrometer.

1. see Section 4.3.4 on page 43

4.3 Calibration of Imaging Spectrometers

An accurate calibration is absolutely necessary for correct usage of imaging spectrometer data in remote sensing of the atmosphere for the following reasons (fundamentals of spectrometer calibration can be found in Schaepman [61]):

a) Intercomparability to Field Measurements

Absolute physical calibration is required if the data have to be compared to measurements at ground level. The sun photometer and the field spectrometer both are based on physical measurements of the radiance. The intercomparison within heterogeneous data sets becomes impossible if one of the components can not be traced to radiance standards. Finally, the spectral and radiative response of each involved instrument has to be known.

b) Intercomparability to Radiative Transfer Codes

The retrieval algorithms for atmospheric constituents are usually based on physical simulations, using a radiative transfer code such as MODTRAN. The simulated radiance at the sensor is compared to the measured values directly, or by using ratioing methods. The direct comparison requires absolutely calibrated radiance values of the raw image data, whereas a relative calibration between the channels may be enough for ratioing algorithms.

c) Atmospheric Correction

Modern atmospheric correction algorithms rely on modeled radiance values which are based on the radiative transfer codes. The simulated path radiance term is subtracted and the influence of the total transmittance is corrected. Such processing is only possible with accurately calibrated data. If the calibration is insufficient or missing, image based approaches have to be used (e.g. dark target, empirical line, etc.; see section 4.5).

d) Spectral Feature Representation

For the investigation of spectral features, the spectral response of the sensor must be known exactly. Errors in the wavelength calibration may adversely affect methods which use strong and sharp absorption features. Wavelength shifts of 1 nm for the central wavelength can induce variations of the radiance of up to 20% for a narrow band image spectrometer. Similar errors can occur if the width of the channels is not known exactly.

4.3.1 Basics of Radiometric Calibration

The signal at the sensor has to be known in physical units (e.g. W/(m²sr)). Its calibration based on measured raw digital numbers (voltage V) can be expressed by:

$$L_s = g\left(\frac{\int r(\lambda)V(\lambda)\mathrm{d}\lambda}{\int r(\lambda)\mathrm{d}\lambda} - V_{DC}\right), \qquad (4.1)$$

where V_{DC} is the dark current of each channel in digital numbers, and $r(\lambda)$ is the wavelength dependent response function. Often the spectral response function is assumed to be Gaussian. For grating imaging spectrometers, the Gaussian response shape agrees with the optical theory (this is strictly valid only if it is plotted against the wave number). For this case it is sufficient if the calibration provides the central wavelength and the 'Full Width at Half Maximum' value (FWHM) as response function parameters for each channel.

The gain factor g describes the relation of the physical radiance units to the digital numbers (DN). This factor is usually assumed to be constant in a good approximation, but certain sensors also show exponential dependencies. For this case, g has to be given as a function of radiance per voltage. The temperature has a strong impact on the bias of radiance detectors. Its influence on each single parameter therefore always has to be calculated during a calibration procedure. An accurate calibration provides at least the following parameters:

- dark current signal V_{DC} of each channel,
- spectral response function $r(\lambda)$ for each channel or central wavelength and FWHM, respectively,
- radiometric response function or gain factor g for each channel, eventually dependent on the detector temperatures.

The data processing facility converts the raw data to calibrated digital numbers which usually are (unsigned) integer values. A given stretching factor allows then derivation of physical units for the radiance in each channel.

Two airborne imaging spectrometers are used for data analysis: The AVIRIS and the DAIS. The calibration steps performed for these two instruments are shortly described in the following two subsections. The geometric and atmospheric calibrations are subsequent steps in the whole preprocessing chain and are described in the Sections 4.4 and 4.5.

4.3.2 The AVIRIS Calibration

Extensive work on AVIRIS calibration has been done by Chrien et al. [13]. Standard laboratory calibration in conjunction with in-flight calibration and validation runs over homogeneous targets led to results of high quality. In descriptions of the most recent data [14], signal to noise (SNR) values of up to 1000 in the visible part of the spectrum are reported. Regarding the SNR, AVIRIS is probably the most reliable imaging spectrometer in operation today.

AVIRIS data are stored as digital numbers ranging from 0 to 65000. These numbers are stretched radiance values by a constant factor of 200 for 1991 data, and 1000 (and 500, respectively) for newer data. The calibrated level 1 data can be scaled to radiance units (mW/(m^2 sr μm)) by applying these constants.

As a consequence of the continuous upgrade of the sensor, the calibration accuracy was improved from flight year to flight year, while the channel characteristics changed. Each of the four AVIRIS sensor arrays has its own calibration file. It is recommended to use only the channels within one single sensor for the

analysis of absorption features to avoid calibration discrepancies between the sensor arrays. The sensor arrays overlap by about 2 channels which can be considered when selecting bands in the overlapping range.

4.3.3 The DAIS Calibration

All operational imaging spectrometers have to be calibrated in regular intervals and validated during the flight season. This concept is also the guideline for DAIS calibration activities. Laboratory calibration is performed every winter, using a known integrating sphere and spectral sources (an overview of the whole process is given in [74]). Because of periodical improvements to the sensor, the single calibration runs have to be remade after each sensor upgrade. This leads to the inconvenient situation that none of the calibration factors valid for one year can be transferred to the succeeding season.

The Kennedy scanner type[1] causes severe problems for calibration because of various reasons: first of all, the calibration results cannot be transferred to the flight conditions since the DAIS is an open system. Temperature, humidity and pressure at the flight level of about 3000–4000 m.a.s.l. differ strongly from the atmospheric situation in the laboratory. This can cause different responses of the sensors or a varying optical state of the mirrors. Furthermore, each of the four rotating faces of the scanner has its own response. Striping effects are the result in uncalibrated images. Their correction has to be calculated with caution since the striping produced by the Kennedy technique depends on the pixel position within the scanline (while the mirror faces change continuously).

The results of the DAIS calibration are, due to the above problems, not as compelling as those of the AVIRIS. Nevertheless, in-flight validation experiments have shown an agreement within a level of 10% to spectral field measurements after atmospheric correction [62]. The signal to noise ratios are given in the range of 50-200, depending on the position in the electromagnetic spectrum. A constant factor of 100'000 is applied to the visible and near infrared radiance values for data storage and distribution, while a factor of 10^6 is used for the thermal bands. The data then are calibrated to the unit [W/(m^2 sr nm)]. The most reliable results of the calibration were achieved for the first detector with its 32 channels (see Table 4.1). This spectral subset is therefore often taken for further processing of DAIS data.

4.3.4 Data Quality Assessment

Signal to noise estimation is a highly inconsistent task because the signal as well as the noise terms can be calculated in several different ways. Some popular sources for the signal are ground spectral measurements, spectral modeling, literature values, or averaged values from the image data itself. The noise can be derived by error propagation calculations, specifications of the data provider or

1. Kennedy scanner: four-faced rotating mirror system, unprotected (without any fore-optics)

from the statistics of the image data itself, assuming the noise to be a non-systematic bias on the image data. A short analysis was made for the data quality assessment of the used image data, using an image based flat field approach.

Two specific data sets of the DAIS (1996) and the AVIRIS sensor (1995) are analyzed (see Section 6.2 and Section 6.3, respectively). For both images, the most homogeneous areas are searched. Regions of Interest (*ROI*) with about 1000 pixels are selected. For the DAIS image a water area can be taken, while an agricultural field has to be taken for the AVIRIS data. A high pass filtering procedure (hp) eliminates non-noise influences on the selected ROI's. The noise is then denoted as the absolute standard deviation (sdev) of the selected area. The image based signal to noise ratio (*SNR*) is calculated in relation to the mean of the whole image channel ($\overline{CH}$) as signal term:

$$SNR = \frac{\overline{CH}}{\mathrm{sdev}(\mathrm{hp}(ROI))}. \tag{4.2}$$

The results for both test images are shown in Figure 4.1. The SNR values are highly related to the incoming radiance in the visible part of the spectrum because the noise variations between the channels are mostly small. The differences in the spectral signature for the vegetation dominated AVIRIS scene 1995, in comparison to the DAIS scene with a significant fraction of water, may partly influence the result. Atmospheric correction (see section 4.5) decreases the SNR since the signal is reduced by the path radiance term while the noise remains constant.

Result of the Image Based Data Quality Assessment

A comparison of the two data sets can only be done roughly with the above procedure; an exact comparison would require simultaneously registered data of both sensors over the same test site. The procedure described above allows a qualitative comparison, whereas correct signal to noise determination needs more sophisticated methods in combination with laboratory data. However, the atmospherically corrected DAIS data can be compared to the raw AVIRIS data, because the scene over Camarillo was taken at very clear atmospheric conditions.

The results in Figure 4.1 depict that in the visible part of the spectrum the AVIRIS seems to have only a small performance advantage over the DAIS. The data provider's signal to noise estimates for AVIRIS is up to 1000 in this part of the spectrum. The noise is possibly overestimated for this scene due to the natural radiance variation within the test target – the agricultural fields were probably not homogeneous enough. Conversely, the test area for the DAIS noise data was open water which is usually of more uniform reflectance.

In the near infrared part of the spectrum the AVIRIS sensor performs satisfactorily, with SNR's well above 100. The DAIS data, on the other hand, only reach values up to 30. For larger wavelengths the performance is even worse. Smoothing filter procedures, or the principal component analysis, have to be applied to suppress the noise in the image data in this spectral range. It has to be pointed out that spatial information is reduced by such processing steps and the

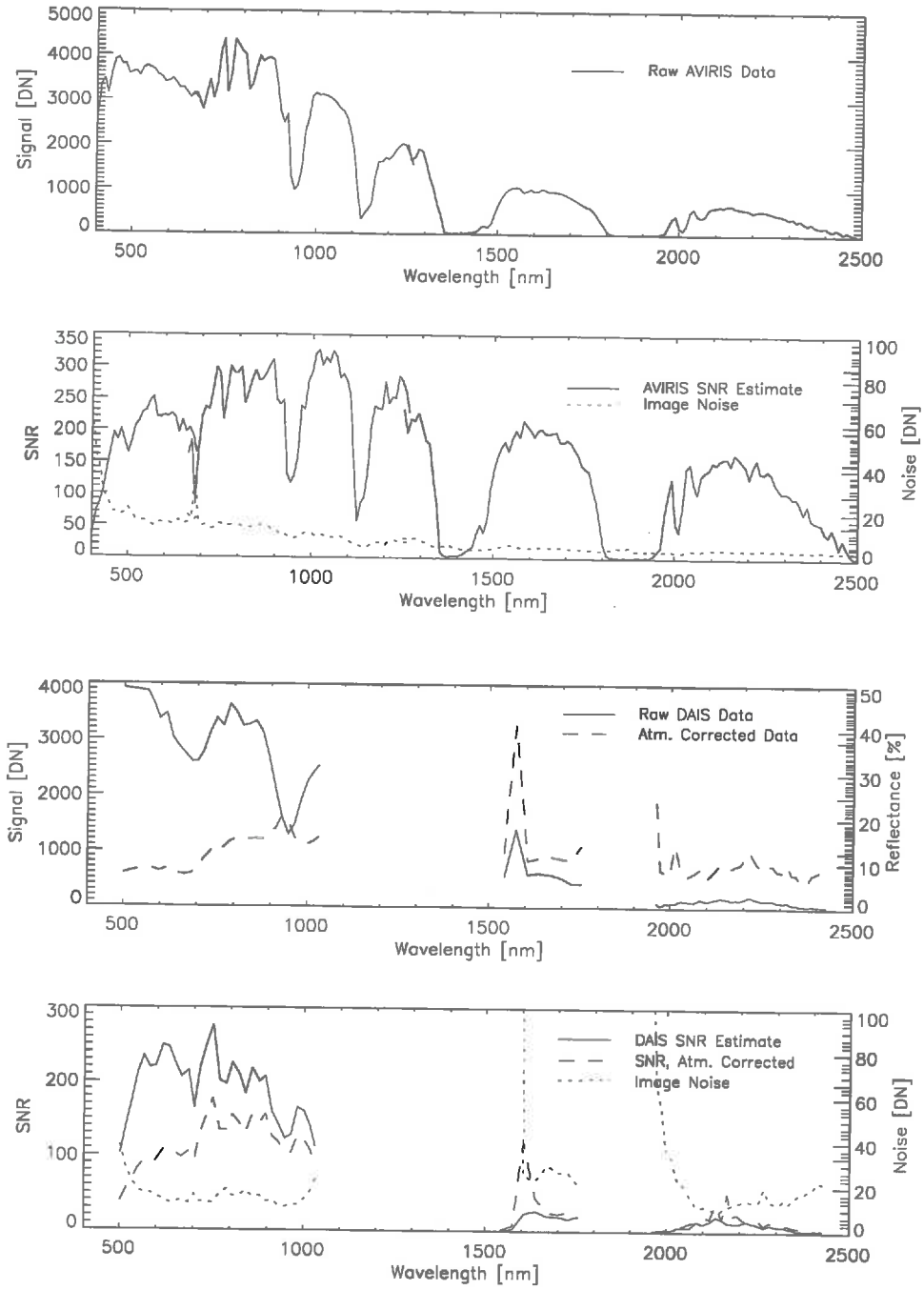

Figure 4.1: **Image based Signal to Noise Ratio (SNR) determination from AVIRIS and DAIS data. The difference in average signal characteristics of the two scenes influences the results.**

difficult radiometric calibration may introduce noise dependent systematic errors.

Both data sets (and sensors) show promising data quality in the visible part of the spectrum up to 1µm. The SWIR range of the AVIRIS (1995) data seems to be very useful too, whereas the corresponding channels of the DAIS (1996) data have to be used with caution.

4.4 Parametric Geocoding of Airborne Scanner Data

Nearly all current imaging spectroscopy data are obtained by scanning airborne systems. The stability of such systems is always worse than that of spaceborne platforms. Thus, geometric distortions occur due to variations of the flightpath as well as of the attitude (given by roll, pitch, and heading angles) of the plane. These distortions cannot be corrected simply by ground control point based traditional georeferencing procedures since the movements cannot be approximated satisfactorily by polynomial transformations of the image. A pixel by pixel calculation has to be performed instead, to account for the position and attitude of the plane during the scanning process.

Atmospheric processing of images over complex terrain requires an exact localization of the image in relation to the corresponding digital elevation model (DEM). Hence, a georeferencing procedure was developed which is based on a parametric approach and theoretically allows sub-pixel accuracy even in steep terrain. A predecessor of the algorithm was developed by Meyer et al. ([49], [50]). The current work resulted in an improved algorithm and a new application for parametric geocoding within the framework of atmospheric processing. A line by line calculation was chosen to improve the calculation performance, while losing only little in accuracy.

All auxiliary data have to be provided at highest accuracy possible. Since this requirement is very hard to fulfill, a ground control point based procedure has been developed to recalibrate the offsets of the attitude angles and to reconstruct the flightpath of the airplane.

4.4.1 Parametric Geocoding as Part of the Preprocessing Chain

Various projects have been carried out at RSL[2] which require either an exact localization of ground truth measurement, or need the information from a digital elevation model (DEM) in relation to the scanner data:

- *Spectroradiometry*: In-flight calibration of the DAIS sensor, using GER 3700 spectroradiometer [61] measurements at ground during the overflight (see [62]),

2. Remote Sensing Laboratories, Department of Geography, University of Zurich

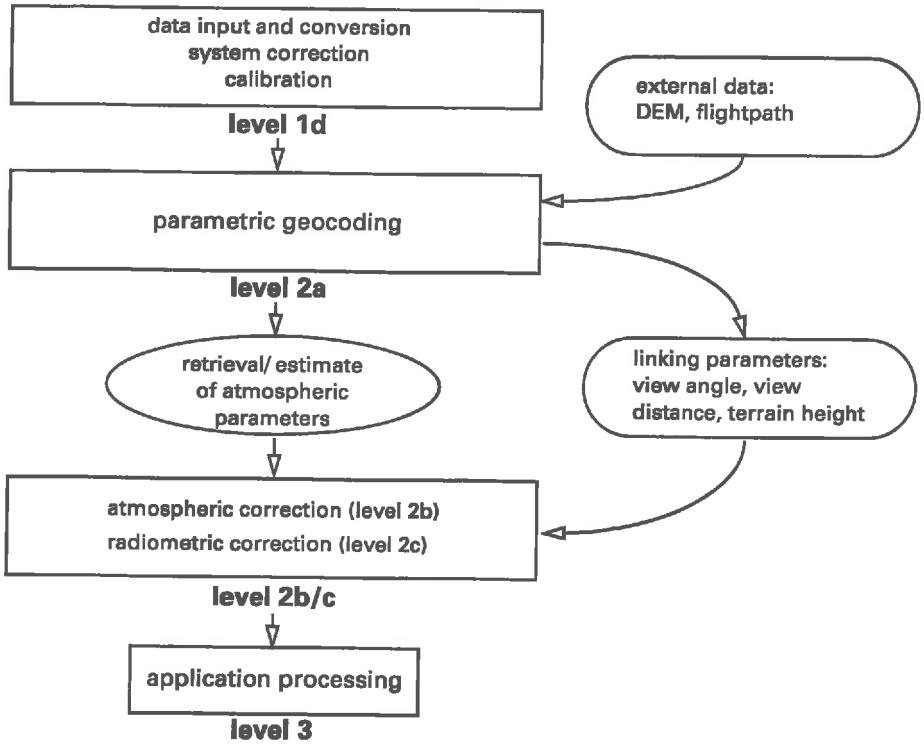

Figure 4.2: A concept for a complete processing chain, including a parametric geocoding algorithm and terrain dependent atmospheric correction.

- *Limnologic imaging spectroscopy*: Determination of chlorophyll content and other constituents in Swiss lakes,
- *Atmospheric imaging spectroscopy*: Water vapor retrieval over complex terrain and atmospheric correction algorithms using the digital elevation model (as described in this study).

The geocoding procedure described hereafter is planned for use in standard preprocessing chains (e.g for DAIS data).

The scheme shown in Figure 4.2 presents the concept of the procedure which includes the combined geometric and atmospheric processing. Geometric and atmospheric correction are no independent processing steps in methodological terms, and thus have to be treated together in the preprocessing chain. It is possible to use parameters from the georeferencing procedure for an improved atmospheric correction. Possible linking parameters are the viewing angle per pixel, the absolute distance from the satellite to each pixel location, or the relative airmass between sensor and pixel. Furthermore, other DEM related parameters, such as height, slope or aspect are required for radiometric correction algorithms and can only be used if the image is brought to the same geometry as the DEM.

The second link which has to be made is the combined atmospheric correction and atmospheric parameter retrieval. It is shown in this study that it is principally impossible to retrieve atmospheric parameters correctly, without using the techniques of atmospheric correction.

4.4.2 Input Data

A variety of input data are required for an exact geometric referencing. Often, some parts of these data are not known exactly and must be estimated or interpolated from external sources. This can occur even in generally well documented test sites overflown with high performance sensors. The three categories of input data are:

a) Navigation Data

These data consist usually of position (longitude, latitude, height) and attitude data (roll, pitch and true heading). They should be resampled exactly for each line (or even each pixel) of the scanner image.

b) Digital Elevation Model

The DEM has to be provided in the same coordinate system as the airplane data. The spatial resolution is chosen based on the nominal pixel size of the image. The DEM initiates the final geometry of the geocoded image.

c) Image/Sensor General Information

Additionally, the following information has to be known: Information on FOV (field of view) and IFOV (instantaneous field of view), scanning frequency, starting time, missing lines, and dimensions of the image.

For use with the geocoding package, all data are read into IDL[3], visually checked, and transformed to the geometrical units (radian and metres).

4.4.3 Geometric Algorithm

The parametric processor starts with an estimate of the 'theoretic view vector' ($\vec{L}$) which is the imaginary line of sight, oriented from an horizontal plane facing direction north to the current pixel. This vector has to be turned in three dimensions to get the 'effective view vector' ($\vec{L}_t$):

$$\vec{L}_t = \mathbf{R} \cdot \mathbf{P} \cdot \mathbf{H} \cdot \vec{L}, \tag{4.3}$$

where **R**, **P** and **H** are the coordinate transformation matrices for roll, pitch and true heading, respectively. The calculation order in equation (4.2) is of interest since matrix multiplications are not commutative – the order to be applied is based on the measurement sequence of the gyros. Equation (4.3) describes, how the sensor is virtually turned from the north looking flight to the actual position

3. Interactive Data Language, RSI Inc.

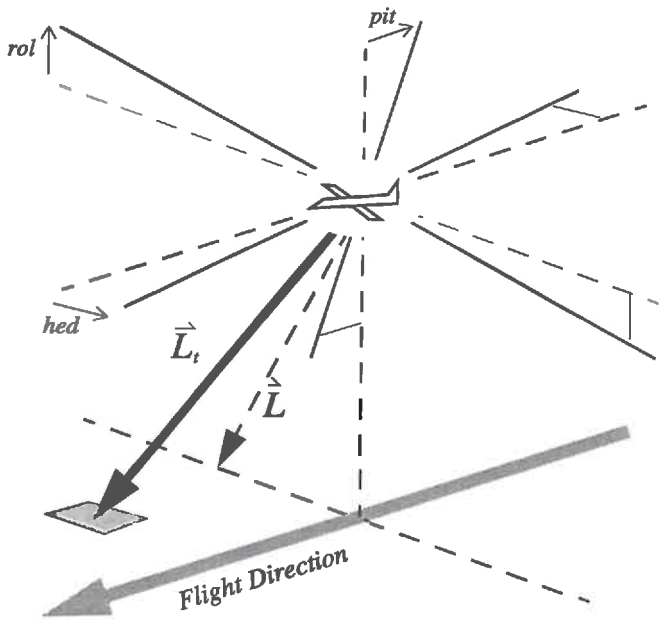

Figure 4.3: Transformation of the theoretical view vector $\vec{L}$ to the effective view vector $\vec{L}_t$. *rol, pit,* and *hed* denote roll, pitch and true heading angles, respectively (modified after Meyer [49]).

(see [18] and Figure 4.3). The vector $\vec{L}_t$ then is intersected with the DEM starting at the airplane position $\vec{P}_a$ to obtain the pixel position:

$$\vec{P}_{pix} = \vec{P}_a + \vec{L}_t \frac{\Delta h}{h(\vec{L}_t)} \quad , \tag{4.4}$$

where Δh is the height difference between the airplane position and the DEM intersection point.

The following steps are performed for the main processing algorithm:

a) Calculate the Current Observation Geometry (see Figure 4.3)

The theoretic view vector ($\vec{L}$) is calculated between the airplane position and a supposed 'flat' DEM, using the instruments FOV and the pixel position information. This vector is then transformed to the effective view vector ($\vec{L}_t$), using equation (4.3).

b) Find the Intersection Point on the Surface

There are various possibilities to intersect a vector with an irregular plane such as the DEM. Meyer [49] used a minimizing procedure of the angle between $\vec{L}_t$ and a number of surrounding test vectors. The intersection procedure used in the PARGE algorithm calculates a height profile along the footprint of $\vec{L}_t$ and searches for a point of equal height on $\vec{L}_t$ (see Figure 4.4).

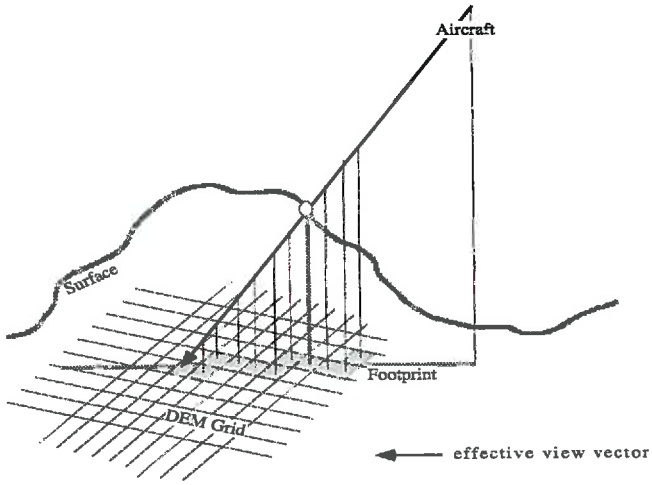

Figure 4.4: Intersection procedure of the effective view vector with the DEM. A profile along the footprint line is compared to the effective view vector for intersection (modified after Meyer [49]).

c) Map the image Coordinates

The pixel coordinates of the image (pixel and line number) are written to an array in DEM geometry at the intersection point position. The result of this procedure is a 'remapping array' which contains the indices of the raw image coordinates, mapped to the corrected positions on the DEM.

d) Fill the Gaps

In order not to loose too much information from the raw image, the spatial resolution of the final DEM (and image) has to be taken slightly higher than the nominal resolution of the original image data. It is not possible to avoid that some of the image data will be multiply mapped, while other parts will be lost because of aircraft motion. If the instabilities are relatively high, there will be a high number of pixels in the final image with no information from the scanner. These gaps have to be filled by image processing techniques in order to achieve an area dependent representation of the image data. Three methods to resolve this problem were tested:

1) The *oversampling method* was proposed by Meyer [49] and uses a temporary DEM with up to 16 times the original number of pixels. At this high resolution, it is possible to calculate the position of all four corners of each pixel and to fill this area with the correct pixel position. Afterwards the DEM is resampled to a final geometry using a modus filter procedure.
2) The *growing method* (see Figure 4.5) is a simple technique which expands each final pixel by a surrounding cross. If an adjacent pixel is already occupied, no replacing will occur. This technique is fast, and yields satisfactory results if high accuracy is not required and the DEM-pixels are of the approximate size of the original image.

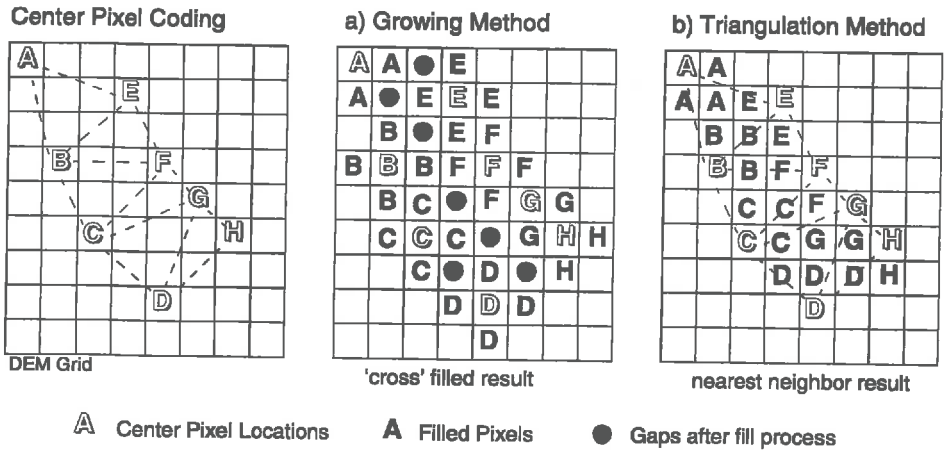

Figure 4.5: Gap filling methods for slightly oversampled output (DEM) images. The grey backgrounds denote the replacement values for the filled cells.

3) Our favored procedure is the *triangulation method*. The center pixel locations are triangulated to remap the missing pixels based on a gridding procedure (see Figure 4.5). The triangulation is a true nearest neighbor technique for filling all occurring gaps between the center pixels. Another advantage to this method is its independence from final product resolution. The produced TIN (Triangular Irregular Network) can be used to achieve whatever image final resolution is required.

e) Final Processing

The final processing step performs the effective production of geocoded images. It is separated from the main processing algorithm. The 'remapping array' is applied as an index directly to the original image data to perform the final geocoding. This step is applied band by band which makes the processing of a band sequential raw data cube very fast. The concept also allows one to process any image channel of the original image geometry, and thus also to geocode results of higher processing levels.

4.4.4 Implementation of the Algorithm

The algorithm was implemented based on the requirements for 'real world' hyperspectral sensors such as AVIRIS or DAIS. A main goal was to create an interactively usable application with all main features between raw input data and image output. A consistent data format was created containing image and DEM descriptions as well as all sets of the auxiliary data. The format helps to reconstruct the processing steps and to store intermediate status reports. Some minor

viewing and analysis capabilities for the DEM and the image data were introduced too but are not key parts of the package.

Ground Control Points Module

A ground control point (GCP) based offsets estimation tool was developed for the PARGE application. The inversion of the georeferencing algorithm allows the calculation of the airplane position for each GCP. The transformed view vector is subtracted from the GCP position and stretched by the relative height:

$$\vec{P}_a' = \overrightarrow{P_{GCP}} - \vec{L}_t \frac{h_a - h_{GCP}}{h(\vec{L}_t)} \quad , \tag{4.5}$$

where $\vec{P}_a$ and $\overrightarrow{P_{GCP}}$ are the position vectors of the airplane and the GCP, respectively, with the absolute heights h_a and h_{GCP}. The differences between the estimated positions $\vec{P}_a'$ and the real navigation data are analyzed to statistically obtain the offsets. Auxiliary data offsets can be calculated for roll, pitch, heading, x-y-navigation, height and/or field of view (FOV). The angular and distance offsets for a number of GCP's are evaluated statistically to obtain the corresponding offset estimates as follows:

- *roll*: average of the angular offsets in scan direction,
- *pitch*: average of the angular offsets in flight direction,
- *x-offset*: average of the distance offsets in longitudinal direction,
- *y-offset*: average of the distance offsets in latitudinal direction,
- *heading*: minimum correlation of the angular offsets in flight direction (pitch) to the pixel distances from nadir,
- *Field of View (FOV)*: minimum correlation of the angular offsets in scan direction (roll) to the pixel distances from nadir.

For heading offset estimation, the correlation between pitch offset and nadir distance is minimized by iteratively adjusting the true heading average. An analogous procedure is used for the height with the roll offset as indicator. Because each offset potentially depends on the others, iterations may be done between them; e.g. the heading offset may be iterated together with the pitch offset over sloped terrain.

A height offset can be interpreted as a FOV offset and vice versa. Each is derived from the other by the equation:

$$FOV_1 = 2\,\mathrm{atan}\left(\frac{h_1 \tan\left(\frac{FOV_0}{2}\right)}{h_0}\right) \quad \text{from} \quad h_1 = h_0 \frac{\tan\left(\frac{FOV_1}{2}\right)}{\tan\left(\frac{FOV_0}{2}\right)}, \tag{4.6}$$

where h_0 is the original flight height, FOV_0 is the original FOV while h_1 and FOV_1 are their corrected counterparts. Note that this method can only estimate the average height offset for an entire flightpath.

Flightpath Reconstruction

The flightpath normally is provided with a data set. If no path is available, a flightpath reconstruction procedure is applied based on a number of GCPs: the xy-position of the plane is determined for each GCP, and an average flight height is derived from the statistics of additional GCPs. The following assumptions allow such a flightline reconstruction based on a number of GCPs:

- the flight altitude is constant within the required accuracy,
- the flight velocity is constant within GCP distances, and
- the flight is more or less straight without any hard turns.

The aircraft position then is calculated using a cubic spline interpolation between the position points (see Figure 4.6). Errors may be introduced into this procedure if the height is not constant during the overflight and if the GCP accuracy is lower than the resolution of the resulting image. The procedure needs approximately one or two GCPs for 100 image lines for flightpath calculation and another GCP for the offsets determination within the same area.

Processing Timeframe

The whole processing (work and computing) can take from a few hours up to a week per scene, depending on the quality of the auxiliary data available. A typical schedule for an AVIRIS image of 512 x 614 pixels may follow this scheme(e.g.):

1) Get all data, including image, DEM, navigation data and airplane attitude data. Convert them to physical units (radian/metres). Test all data with a quick preview (1–6 h of work).
2) Check the flightpath and introduce a number (5–20) of ground control points. Possibly reconstruct the flightpath (1–8 h of work).
3) Calculate or test the offsets of the attitude data, using the selected ground control points. (2–4 h of work).

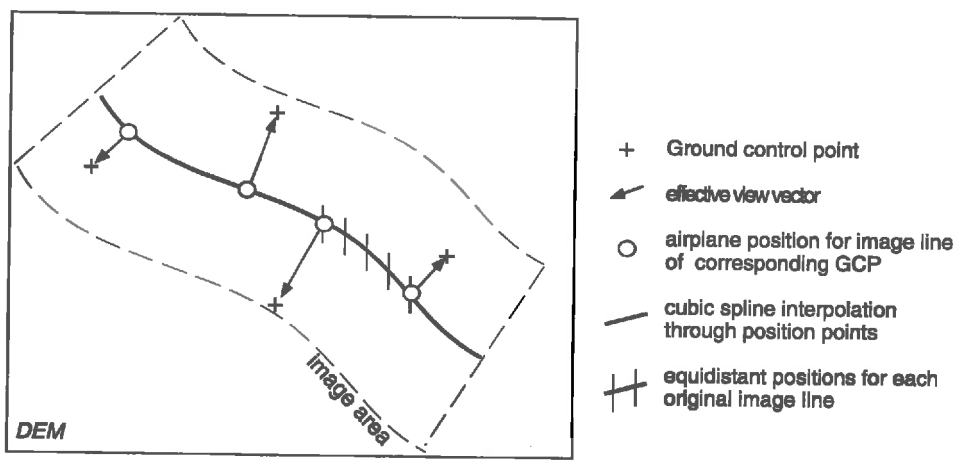

Figure 4.6: The flightpath reconstruction procedure.

4) Run the centre pixel georeferencing on a subset of the image and check the position on the DEM (15–30 min).
5) Run the main geocoding processor on the whole image (30 min–2 h runtime, depending on the computing speed).
6) Remap single bands and afterwards the whole cube (10–50 min runtime).

Based on the above estimates, a fast processing would be possible within about 5 hours of work and 1–2 hours of runtime. This time increases proportionally with the required geocoding quality and the number of lines to be processed. Additionally, missing or corrupted auxiliary data may cause substantial delays in processing.

4.4.5 The PARGE Application

All the described features were implemented within an application environment suited for further distribution and operational use. The new PARGE application supports the following features:

- consistent data structure for various airborne imaging instruments,
- consideration of the exact navigation data by line or by pixel,
- exact correction of roll, pitch and true heading (no small angle approximations),
- ground control point based algorithms for auxiliary data offsets estimation and flightpath reconstruction,
- output to desired DEM geometry,
- two implemented geocoding algorithms for different accuracy requirements:
  - 1st: sub-pixel accuracy achieved by a DEM-oversampling algorithm (considering the real dimensions of each pixel),
  - 2nd: pixel accuracy using a pixel centre based triangulation algorithm,
- nearest neighbor technique prevents data modifications,
- fully IDL (Interactive Data Language, RSI Inc.) based and therefore portable application with window based user interface and on-line help system.

Further information about the application and its availability may be found in Appendix D.2 or is available from the author.

4.4.6 Results

Application to AVIRIS Data

The new algorithm was applied to AVIRIS 1995 data over complex terrain in Camarillo, California. The geocoding of a 1991 AVIRIS data set was performed with the algorithm's predecessor (as described by Meyer [49]).

The internal navigation system of the airplane provided poor resolution at low absolute accuracy since there was no differential GPS system mounted during the 1995 AVIRIS campaign. It was therefore necessary to reconstruct the flightpath from the image data using the described procedure. The roll angle was set to zero because AVIRIS roll compensation was switched on. These two restrictions

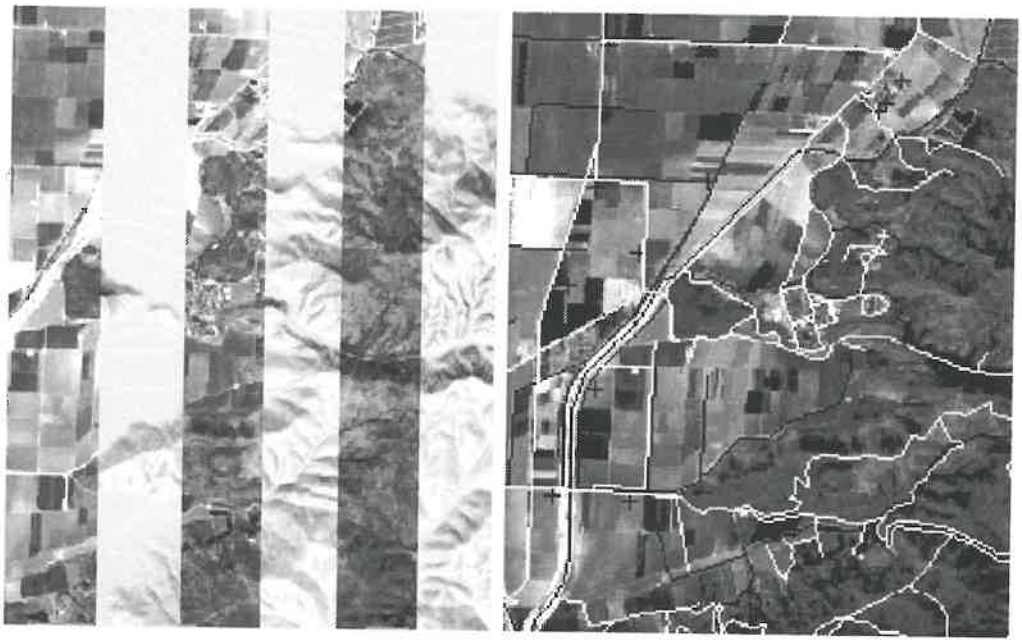

Figure 4.7: Subsets of the geocoded AVIRIS image of Camarillo (CA) in comparison with a DEM shadow view image (left) and with USGS digital linegraphs (right).

led to a lower geocoding accuracy than potentially attainable.

The fast pixel centre based algorithm could be used for the required final USGS DEM resolution of 30 m. The processing of the standard AVIRIS image (614x512 pixels) was performed within half an hour on a Sun SPARC 20 workstation. This time would increase by about a factor of 4 if for example 15 m final resolution would be chosen. The geocoded image is shown in Figure 4.7 in comparison with a DEM shadow view image. The ridge lines of the mountains fit within one pixel shift.

Application to DAIS Data

In 1996 the DAISwiss'96 calibration campaign was carried out in Central Switzerland ([74], [62]). The DAIS Sensor of DLR was flown in a DO–228 aircraft at an altitude of about 4000 m above sea level. Its nominal pixel size is 6 m at 512 pixels per line. Since its attitude is not very stable, horizontal distortions of up to 30 pixels can occur. These shifts have to be corrected with the parametric procedure. In the flight campaign of 1996, no exact navigation data were acquired due to technical problems. Therefore, the flight line had to be reconstructed using the above procedure with a set of 20 GCPs. The resulting image is shown in Figure 4.8 in comparison with the digital topographic map.

The error of the geocoded image is in the range of 2 to 8 pixels (50 m). However, all attitude effects appearing clearly in the raw image could be removed,

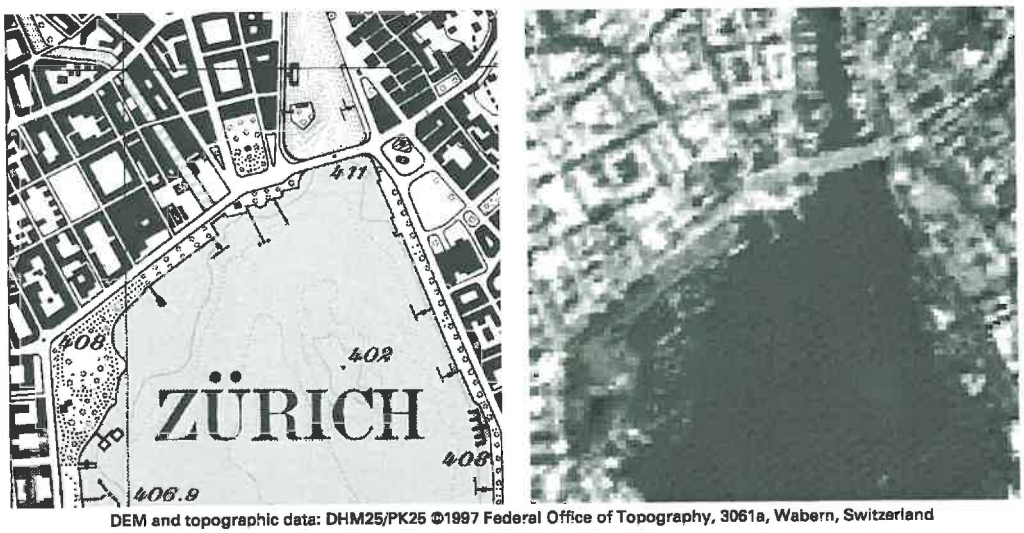

DEM and topographic data: DHM25/PK25 ©1997 Federal Office of Topography, 3061a, Wabern, Switzerland

Figure 4.8: Comparison of a subset of the geocoded DAIS image with a digital topographic map of Zurich.

making the resulting image useful for further interpretations. A second test on DAIS data was made in 1997. The test area in Central Switzerland was then flown and several data sets could be registered. This time, the flightpath was measured at an accuracy of better than one meter with a differential GPS on board the aircraft. The effects of gyro (mis–)calibration were therefore visible during the processing.

4.4.7 Geocoding Quality Assessment

Quantifying geocoding quality is difficult. Methods typically applied are:

- calculation of the location residuals of ground control points which were not used for the prior calculation,
- comparison of the image results with the DEM along terrain lines or in specific mountainous areas,
- overlay of digital linegraphs or pixel maps on the geocoded results (see Figure 4.8).

The quality was found to be within the accuracy of the input data. The parametric geocoding was possible at an accuracy of below three pixels (better than 20 m) for DAIS image data with known flightpaths. Distortions occur whenever the DEM altitude does not agree with the surface height (e.g. forests and settlements) and the compared object is located off nadir in the image. Such residual errors could be corrected by using real digital surface models.

If the flightpath is unknown, the accuracy for DAIS data is within 8 pixels (40–50 metres), while for AVIRIS data accuracies of 1–2 pixels are achieved (20–

40 metres). The higher accuracy of the AVIRIS data processing is possible due to the much more stable flight of the ER-2 aircraft at 20 km height, where the flightpath within one scene is approximately linear.

The residual errors for the DAIS data are attributed to the unknown gyro calibration of the instrument. Various analyses showed that the mounted gyros were drifting during an overpass. They had therefore to be cross-calibrated with the low resolution aircraft INS–gyro information. Still, this attitude determination was far from being perfect for the DAIS data. The results prove how important correct auxiliary data preprocessing is for obtaining geometrically correct data.

4.4.8 Conclusions on Parametric Geocoding

A new geocoding processor was implemented using a parametric approach. It allows for correction of attitude and flightpath dependent distortion, even for unstable sensor platforms such as for low level airplanes. The algorithm is now in a test status for hyperspectral sensors. Extensive tests have been performed in winter 1997/1998, whereas a fully operational application is planned for 1999. Currently, the DAIS and AVIRIS sensors are supported with perhaps further airborne systems to be introduced later. It was possible to geocode imaging spectroscopy data in mountainous terrain at accuracies of 20 to 50 m using this GCP based PARGE algorithm.

The DAIS data were geocoded at accuracies of 2-4 pixels using a DGPS measured flightpath. The gyro data was of mediocre quality and had therefore to be recalibrated using GCPs and absolute values from the aircraft INS. This procedure can not be extended to higher accuracies since the accuracy of GCPs is limited to approximately ± 15 m. The only solution for spatially high resolved sensors thus is an absolute calibration of the gyros together with differential GPS measurements of the flightpath.

AVIRIS geocoding leads to satisfactory results using USGS DEMs. Digital elevation models of higher accuracy would increase the accuracy of the geocoding at high spatial resolutions. Further work could be done on accurate residual roll determination on roll compensated AVIRIS images. The accuracy of AVIRIS pitch and true heading calibration has not yet been examined by the author. Another main issue is the introduction of DGPS based flightpath determination for airborne scanners in general. The presented GCP flightpath determination is only a rough estimate for missing or insufficient navigation data; the accuracy is significantly decreased compared to a georeferencing with an exactly known flightpath. The results are nevertheless better than those achieved with traditional georeferencing methods applied to images of unstable platforms flown over rugged terrain.

4.5 Algorithms for Atmospheric Correction

One of the applications of atmospheric gas detection is the use of the gas distribution for atmospheric correction of the image. The amount of water vapor, for instance, can be fed into a correction algorithm by weighting the wavelength dependent transmittance values of water vapor with its amount. The atmospheric correction reduces the radiance at the sensor to a reflectance value at the ground. The bidirectional reflectance distribution function (BRDF) usually is not considered by such functions. A simple Lambertian cosine correction is applied to the geocoded data to account for the relative angle between the direction of the solar incidence and the sensor-target line.

4.5.1 Empirical Methods

All empirical methods are based on the a priori knowledge of some targets within the image. The information gathered from these pixels is extrapolated to the whole image, normally without consideration of the topographic structure. Some algorithms for empirical atmospheric correction are well established because they often provide valuable results at low computing (and working) time.

a) Flat Field

The 'flat field approach' uses a spectrally flat spectrum out of the image data itself to derive a quasi-reflectance value for the whole image [56]. It thus does not require any a priori information about the ground reflectance. The reflectance is then defined as

$$\rho = \frac{V_s}{V_{ff}}, \tag{4.7}$$

where V_s is the measured voltage in each sensor pixel and V_{ff} is the flat field voltage of the chosen spectrum. Since the flat field approach works also on non–calibrated data it includes a correction for sensor calibration uncertainties. It can therefore (per definition) not be attributed as 'atmospheric correction'.

b) Known/Bright Target

If the reflectance of a (large) ground calibration target is known and the image data is calibrated to radiance values, an internal reflectance calibration can be performed:

$$\rho = \frac{L_s}{L_{ff}}\rho_{ff}, \tag{4.8}$$

where ρ_{ff} is the known flat field reflectance. A variation for known reflectance is the 'bright target' approach. It divides all image elements by the spectrum of the brightest pixel found in the image. Under the basic assumption that $\rho_{ff} = \rho_{bright} = 1$, equation (4.7) reduces to

$$\rho = \frac{L_s}{L_{ff}}. \tag{4.9}$$

The reflectance values retrieved with this methods are highly dependent on the selected reference reflectance. Such a method should only be used if a rough estimate of the reflectances in an image is sufficient.

c) Dark Target

An often used and straightforward method is called the 'dark target approach'. The darkest part in the image is taken and assumed to be black (reflectance ≈ 0). The measured radiance of this target (L_{dark}) is reported as atmospheric radiance. This radiance is subtracted from the relatively calibrated image data. The black target-corrected reflectance is derived according to

$$\rho = \frac{\pi(L_s - L_{dark})}{E_0 \cos\varphi}, \tag{4.10}$$

by dividing the corrected radiance with the surface solar irradiance. Problems arise from unknown adjacency radiation on the dark targets, the assumption on zero reflectance, and the missing information on the height distribution of the path radiance terms (see [30], [38]).

d) Empirical Line

A combination of the dark target and the bright target approach is the empirical line fit. A flat field target of known reflectance and a black target are defined in the image. These two targets define an empirical line for the relationship between reflectance and the radiance at the sensor. The reflectance then is derived by solving the linear equation for the reflectance [72]:

$$\rho = \frac{L_s - L_{black}}{L_{ff} - L_{black}} \rho_{ff}. \tag{4.11}$$

Another method to retrieve the empirical line is based on two (or even more) non-dark targets. The empirical line which relates reflectance and the measured radiance at the sensor can then be derived analytically. If more targets are available, the line may be obtained by a least squares fit to a linear or to an exponential function. The inversion equation for two targets with reflectances ρ_1 and ρ_2 and an at sensor radiance L_1 and L_2, respectively, is then defined as:

$$\rho = \frac{L_s - L_1}{L_2 - L_1}(\rho_2 - \rho_1) + \rho_1. \tag{4.12}$$

The empirical line fit is able to produce good results over flat terrain, but it still will fail in mountainous areas and for sensors with wide swath angles. For these conditions, height and angle dependent procedures have to be applied which can not be solved by such simple approximations.

4.5.2 Radiative Transfer Code Based Methods

Empirical atmospheric correction methods have the big advantage that no a priori information on the state of the atmosphere is required. When using a radiative transfer code, the forward runs of the model have to be done with special respect to the geometric and atmospheric situation for one specific scene. The external parameters used for such methods are:

- geometry of the sun (sun zenith and azimuth angle),
- geometry of the sensor (sensor view angle),
- the atmospheric profile of pressure, temperature, humidity and trace gases (usually a standard profile is chosen),
- aerosol description based on visibility, aerosol type and profile.

These parameters are used to invert the radiative transfer equation (2.12) for the ground reflectance ρ_g, calculated from the radiance at the sensor (L_s):

$$\rho_g = \frac{\pi(L_s - L_{atm})}{\tau_u E_0(\tau_d \cos\varphi + \tau_{d,\,dif} s)} - w_a \rho_{adj}. \tag{4.13}$$

The parameters φ and s are derived directly from the geometrical conditions of the image. All other parameters have to be simulated with the radiative transfer code. The parameters L_{atm}, τ_u, τ_d, $\tau_{d,dif}$, and a vary for each pixel location and thus have to be interpolated over view angle and height.

The correction can be simplified by neglecting the adjacency term and introducing the apparent transmittance term to

$$\rho_g = \frac{\pi(L_s - L_{atm})}{\tau_{tot} E_0(\cos\varphi + c)}. \tag{4.14}$$

The diffuse irradiance term is corrected by a constant c which can be described by Minnaerts model [70], derived semi-empirically, or calculated from the effective skyview factors and diffuse transmittance values (the downward diffuse transmittance itself is often approximated with $\tau_{d,dif} = 1 - \tau_d$). This model is equivalent to the correction proposed by Woodham [83]. The simplification for the irradiance term only can be made if the angles between the sun and the slope of the terrain are less than 40 degrees for most of the area (as already shown in Section 2.1.2 on page 7). For high zenith angles and steep terrain equation (4.13) has to be used.

a) Knowledge Based Methods

Atmospheric correction algorithms which make no use of the image data itself, require that all parameters are known from external sources. Some of the parameters are based on calculation over the DEM, while others are given by the solar and the sensor geometry. Information on the atmosphere has to be taken from meteorological stations and radiosonde profiles. This data is hard to obtain for a specific test area and is often of unsatisfactory quality. The disadvantage of such methods is that they rely on single measurements, whereas their advantage is a

high degree of automation. A detailed description of such a method is given in [59]. Knowledge based methods still have to use the image data if adjacency effects have to be corrected.

b) Image Based Methods

More accurate results can be achieved if some of the data is extracted from the image data itself, e.g. water vapor and the aerosol content [28]. The retrieval of the humidity is described in other parts of this study. Its spatial distribution allows calculation of exact value of the water vapor transmittance for all pixels and wavelengths. ATREM [16] estimates the water vapor content based on differential absorption techniques prior to the correction of the atmospheric effect.

The estimation of the aerosol content is not yet so advanced. Statistical approaches use the contrast reducing effect of strong scattering to estimate the aerosol content. Histogram matching allows one to even obtain the spatial distribution of the haze in the image [57] - as long as the image data is statistically homogeneous. Simpler approaches use dark targets or flat fields for an estimate of the atmospherically scattered radiance within the image. All currently known methods for aerosol correction do not attempt to quantify the physical abundance of aerosols, but try to achieve an assumption on the aerosol scattered radiance from the image data.

4.5.3 Adjacency Correction

The correction of the atmospheric adjacency effect is vital, especially for limnological applications. It has been shown that this effect significantly influences the radiance at the sensor up to distances of 1 to 3 km for spaceborne sensors [75]. Tests with a helicopter mounted spectroradiometer have proven that the effect is significant for flight heights of 1000 m above ground and higher [63]. The effect was significant on a horizontal range of 100–200 m for flight altitudes below 3 km.

Standard atmospheric correction methods usually do not include an adaptive compensation for the adjacency radiance (often an average adjacency is considered), although this effect can easily override the information over dark targets. Each pixel has to be corrected with respect to the average reflectance of the adjacent areas. This can be done by the definition of a spatial convolution function which takes a distance-weighted average of the adjacent area in the image to calculate the adjacency factor $\rho_{adj} w_a$ (see (4.13). The corresponding radiance has to be simulated in the radiative transfer code as indirect ground reflected radiance [2]. The shape of such a function depends on the aerosol content, the type of aerosols, the view angles, and the height of the sensor above the ground. Its correct modeling is not yet solved and remains a very challenging task.

Chapter 5:

Differential Absorption Techniques

The optical measurement of atmospheric trace gases can be performed using selected sensor channels located in bands or lines of the absorption spectrum. To quantify the amount of a specific gas between a target and the sensor, the so called differential absorption technique is applied [11], [40]. It performs a ratioing between influenced channels within the absorption band (*measurement channels*) and non influenced channels on the sides of the band (*reference channels*). This ratio is then related to the apparent transmittance which depends on the gas column. The various ratioing methods differ from one another in number of selected channels and calculation technique.

One objective of this work was to define and test the best performing differential absorption technique for imaging spectroscopy of tropospheric water vapor. A methodology is described in the following sections based on the appropriate selection of channels and a sophisticated differential absorption technique.

5.1 Methodology of Channel Selection

Two types of channels are distinguished:

- *Reference Channels:* They are usually located close to an absorption feature, and their transmittance is relatively high:
  - i) The signal in a reference channel should not be influenced by any atmospheric species, and
  - ii) its effective signal to noise ratio must be as large as possible.
- *Measurement Channels:* Such channels lie within an absorption band. They should meet three conditions:
  - i) they must be sensitive to variations of the gas amount,
  - ii) the difference between the signal of the absorbing gas and the noise should be clearly discernible, and
  - iii) other absorbing atmospheric species must not disturb the signal of the trace gas of interest.

Both reference and measurement channels can be evaluated using a quantitative

channel selection procedure. Specific evaluation factors are defined for all channel criteteria. The following methodology considers the whole spectral range of one or more absorption features and picks the best channels based on the atmospheric state of a specific scene and the spectral characteristics of the used instrument. The approach helps to avoid the use of erroneous channels while retrieving the maximum amount of information on the investigated absorption feature.

Qualification factors will now be defined for both channel types. Each factor represents an important channel property, as already given in the above definitions. The factors are scaled between zero and one. A value of '0' is assigned to 'not usable' for the given attribute, while a value of '1' is the 'best possible' rating for a channel with respect to the investigated attribute. The single factors finally are multiplied which defines common qualification equations for both reference and measurement channels.

5.1.1 Selection of the Reference Channels

The signal of a reference channel should not be influenced by any atmospheric species and the effective signal to uncertainty ratio must be as large as possible. Thus, the channel selection indicator for the reference channels is defined as the product of an atmospheric transmittance factor M_{trans} and a radiance uncertainty factor M_{noise}.

Transmittance Factor

The transmittance factor M_{trans} is the product of the transmittances τ_a of all atmospheric absorbers and the water vapor transmittance τ_{wv}:

$$M_{trans} = \tau_{wv} \prod_a (\tau_a) = \tau_{wv} \tau_0, \tag{5.1}$$

where τ_0 is the total transmittance of the atmosphere if no water vapor were present.

Radiance Uncertainty Factor

The radiance uncertainty factor M_{noise} is based on the observed variations of the radiance at the sensor:

$$\Delta L_s = \sqrt{(L_{ner})^2 + (L_{scal})^2 + \left(\frac{\Delta\rho}{\rho} L_{gnd}\right)^2} \tag{5.2}$$

The radiance uncertainty depends on three major parameters. First, the total noise equivalent radiance L_{ner} of the sensor channel is given by the sensor specifications. Second, L_{scal} is the radiance error due to spectral calibration uncertainty. It is derived from the variation of the radiance at the sensor if the same radiance spectrum is convolved to varying central wavelengths of a channel. The third term takes into account the variation of the radiance reflected at ground L_{gnd} due to the variability of the ground reflectance $(\Delta\rho)/\rho$ within the image.

This third factor is approximated directly from the mean standard deviation of each image channel radiance.

The radiance uncertainty factor then is defined relative to the radiance at the sensor as

$$M_{noise} = \frac{L_s - \Delta L_s}{L_s}. \tag{5.3}$$

Note that this factor is less than zero if the radiance uncertainty is greater than the expected radiance at the sensor.

Reference Channel Evaluation Factor

The two factors given in equations (5.1) and (5.3) are multiplied to evaluate the reference channels:

$$M_{ref} = M_{trans} \cdot M_{noise} = \tau_{wv}\tau_0 \cdot \frac{L_s - \Delta L}{L_s}. \tag{5.4}$$

A good reference channel is characterized with a high M_{ref}-value. For the evaluation, the following parameters are simulated for each spectrometer channel using the MODTRAN3 radiative transfer code: the apparent water vapor transmittance τ_{wv}, the apparent total atmospheric transmittance τ_0 of all disturbing atmospheric species, the radiance at the sensor level L_s and the total ground reflected radiance L_{gnd}. All simulations are done for a standard reflectance of $\rho = 0.4$.

In addition, the wavelength distance of the reference channels from their corresponding measurement channels has to be considered. It has to be minimized to reduce errors due to spectrally non-linear background reflectance characteristics. This factor is not included quantitatively because it has not possible to describe the spectral coherence of general spectra analytically (heretofore). It is nevertheless considered here by evaluating only up to 5 potential reference channels on each side of the absorption feature.

5.1.2 Selection of the Measurement Channels

Measurement channels are searched within the absorption band because they should be sensitive to variations in water vapor (→ sensitivity factor). Furthermore, the difference between the water vapor signal and the noise must be clearly discernible in these channels (→ significance factor) and other absorbing atmospheric species must not disturb the signal (→ cross sensitivity factor).

Sensitivity Factor

An absorption band is assumed to have a similar behaviour relative to the trace gas concentration as a single line. Hence, the modified Beer-Lambert law is a reasonable description of the transmittance function, as already shown in Section 3.2 on page 29:

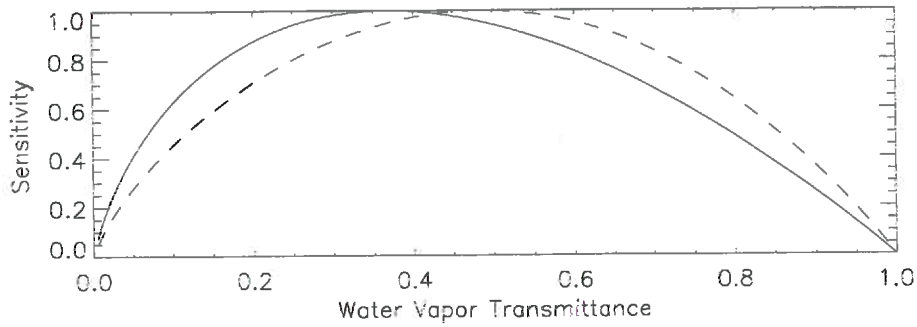

Figure 5.1: Relationship of sensitivity to the apparent water vapor transmittance with a maximum value at 1/e. The dashed function represents the relationship if the exponent b in eq. (5.5) increases linearly with the absorption coefficient k (see text).

$$\tau_{wv} = e^{-k(PW)^b}. \tag{5.5}$$

The absorption coefficient (k) can be described by inversion of this equation as $k = \ln(\tau_{wv})/(PW)^b$. Using these relationship, the change of the water vapor transmittance τ_{wv} due to a variation of the total column of water vapor PW follows directly as

$$\frac{\partial \tau_{wv}}{\partial (PW)} = -k\tau_{wv}b(PW)^{b-1} = -\frac{\ln(\tau_{wv})}{(PW)^b}\tau_{wv}b(PW)^{b-1} = -\frac{\ln(\tau_{wv})}{PW}\tau_{wv}b \ . \tag{5.6}$$

Note that the goal of the sensitivity analysis is an evaluation of the measurement channels for a given average water vapor amount. Thus, PW is to be taken as a fixed average value, valid for all compared channels. The exponential parameter b is assumed to be independent of the wavelength. The variations in k are described by the channel dependent transmittance, simulated at the average water vapor amount PW. Equation (5.6) is maximal at $\tau_{wv} = \frac{1}{e}$. The maximum position is independent of the absorption coefficient (and also independent of the constants b and PW). This can be proven by setting the first derivative of this function against τ_{wv} to zero. The sensitivity factor is now defined as equation (5.6), normalized to a maximum value of 1:

$$M_{sens} = -e \cdot \ln\tau_{wv} \cdot \tau_{wv}. \tag{5.7}$$

This scaling is meaningful because the quantities PW and b are the same for each channel. The factor e is derived directly from forcing the maximum value of the function (5.6) to one. Lower transmittances tend to saturate, whereas at higher transmittance the water vapor signal is too low.

The assumption of a constant exponent b (see equation (5.5)) for varying absorption channels leads to the above function. For low absorption channels, simulations show that b is rather a decreasing function of the absorption coefficient k (see Section 5.5). In a first approximation, a linear relationship is now assumed, such that $b_{k=0} = 1$ and $b_{k=0.58} = 0.62$ (the latter values for k and b originate from the analysis in Section 3.1.4 on page 24). With this function, the sensitivity factor curve maximum shifts to a higher water vapor transmittance, such that the best channels are at a transmittance value of about 0.5 instead of $\frac{1}{e}$ (see Figure 5.1). Some further analyses of the relationship between the factors b and k are given in Section 5.5 on page 85.

Significance Factor

The significance factor M_{sign} is defined as a relation between the radiative signal of water vapor and the radiance uncertainty (as given in equation (5.2)):

$$M_{sign} = \frac{(L_{PW=0} - L_s) - \Delta L_s}{L_{PW=0} - L_s} = 1 - \frac{\Delta L_s}{L_{PW=0} - L_s}, \qquad (5.8)$$

where $L_{PW=0}$ is the simulated theoretical radiance at the sensor if the trace gas amount were zero. Note that M_{sign} is negative if the total radiance uncertainty is greater than the expected absorption signal. M_{sign} is defined in a similar way as M_{noise} in equation (5.3), the only difference being the definition of the radiative signal.

Cross Sensitivity Factor

The third factor takes into account the influence of the transmittance by any other atmospheric constituent different from water vapor:

$$M_{cross} = \prod_a (\tau_a) = \tau_0 . \qquad (5.9)$$

The cross sensitivity describes disturbing signals absorbers other than the required water vapor.

Measurement Channel Evaluation Factor

The three effects described in the equations (5.7), (5.8), and (5.9) are now multiplied. The product of the three parameters is the wavelength dependent channel qualifier for the measurement channels:

$$M_{meas} = M_{sens} \cdot M_{sign} \cdot M_{cross} \qquad (5.10)$$

$$= -e\tau_{wv} \ln \tau_{wv} \cdot \left(1 - \frac{\Delta L_s}{L_{PW=0} - L_s}\right) \cdot \tau_0 .$$

The crucial factor for strong absorption features is the sensitivity factor which allows the selection of measurement channels dependent on the water vapor amount in the atmosphere. For weak features, the other two factors become more

important. They allow for a decision on whether it is theoretically possible to measure the absorbing gas using the investigated channel.

5.1.3 Channel Selection Results for AVIRIS Data

The channel selection procedure was applied to MODTRAN-simulated data for the situation of AVIRIS images taken in 1991 over Central Switzerland, and in 1995 over Camarillo (California). Ranked sets of channels to be used in the differential absorption technique were defined. A selection threshold is introduced on the measures M_{meas} and M_{ref} to define a limited set of measurement and reference channels, excluding the worst channels from further consideration. The selection line is chosen such that a number of 5-6 channels for each type remains.

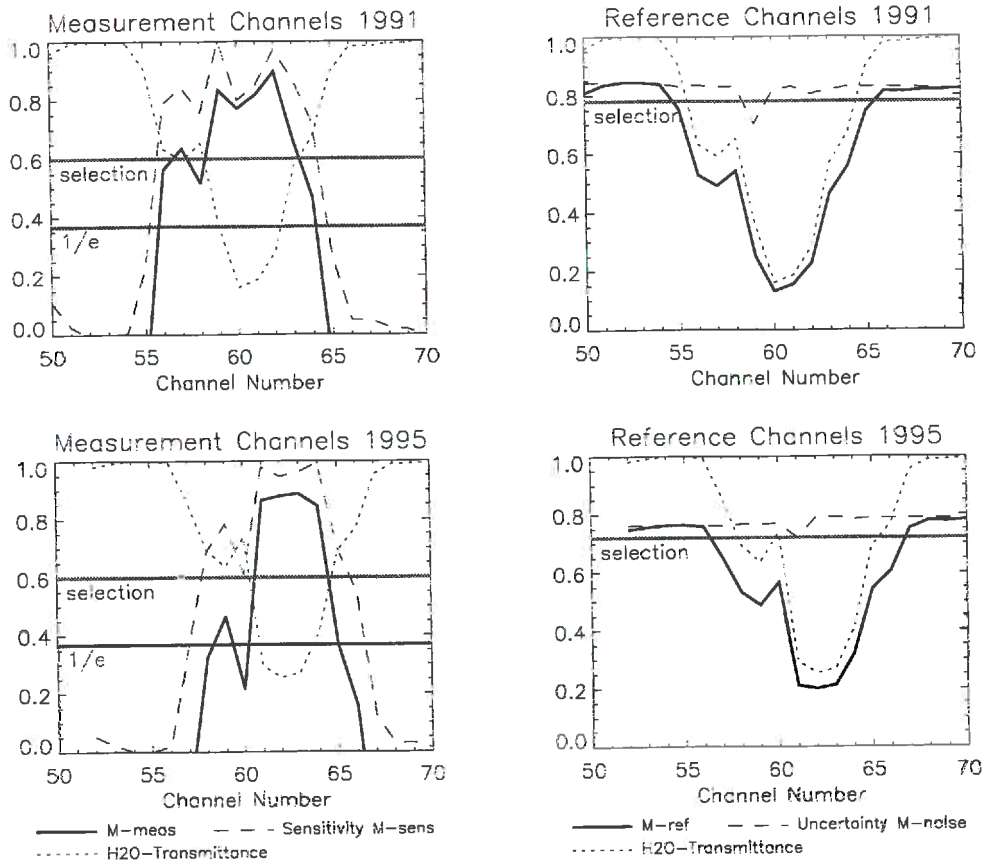

Figure 5.2: **Channel Selection Results for AVIRIS data sets of 1991 and 1995 with 2.8 and 1.9 cm precipitable water, respectively. For the measurement channels, the crucial sensitivity factor is shown for illustration, while the almost constant noise factor is depicted for the reference channels.**

The best suited water vapor absorption feature for nadir viewing sensors under average atmospheric conditions (≈ 2-3 cm of precipitable water vapor) is the 940 nm band. The transmittance characteristics in the center of this band are nearly ideal with respect to the selection of measurement channels. Furthermore, the influence of aerosol scattering is not dominant, whereas the total radiance is satisfactorily high. Hence, only channels between about 850 nm and 1070 nm are further considered under normal atmospheric conditions. At lower water vapor content (below 1 cm), a stronger band with sufficient absorption may be considered (e.g. the 1130 nm band). Conversely, at high content (over 3 cm) the channels in the band slopes are favored, or bands of lower absorption have to be chosen (e.g. the 820 nm band, see also Section 2.4 on page 16).

A crucial factor for the measurement channel selection is the average total water vapor transmittance which has to be estimated from total columnar water vapor content for each scene for the test cases. In the 1991 AVIRIS experiments the water vapor column was integrated from radiosonde profiles taken during the overflight time. For the 1995 data profiles from the subsequent day under similar meteorological conditions were available. For operational use, however, this quantity can also be calculated from standard atmospheric profiles. It influences mainly the selection of the measurement channels.

A plot of the most significant factors, following the equations (5.4) and (5.10), for 1995 and 1991 AVIRIS channels is shown in Figure 5.2. Table 5.1 lists the selected channels for the two data sets. The large evaluated channel sets allow numerous combinations of reference and measurement channels in differential absorption techniques. The plots clearly show that the spectral position of the favored measurement channels may change according to the atmospheric water content. The band center of the 940 nm band only has to be favored for water vapor content up to 2.5 cm, while for higher humidity the channels in the slopes would be more sensitive.

	AVIRIS 1991	AVIRIS 1995
measurement channels	57,59 to 62 (910, 930 to 959 nm)	61 to 64 (932 - 961 nm)
reference channels (close to the selected meas. channels)	52 to 54 (862 to 881 nm) 66 to 70 (987 to 1036 nm)	54 to 56 (865 to 884 nm) 68 to 70 (999 - 1018 nm)

Table 5.1: Selected AVIRIS channels for water vapor retrieval with 1991 and 1995 data sets.

5.2 Compilation of Differential Absorption Techniques

Differential absorption techniques are a practical way to determine gas content from a spectrum of an absorption band at low computing time costs. In general they perform a ratioing between the radiance at channels within the absorption feature (measurement channels), and an interpolated radiance of channels in its vicinity (reference channels) to detect the relative strength of the absorption which is related to the total column water vapor. Two major differential absorption techniques were used for hyperspectral imaging spectroscopy and compared in an earlier work [11]: The Narrow/Wide technique (N/W; [22]) and the Continuum Interpolated Band Ratio (CIBR; [32], [10]). A variation of the CIBR, the Linear Interpolated Regression Ratio (LIRR) was introduced for noise reduction purposes [65], while the single band ratio (also band quotient, BQ, [40]) is only of historic value. A summarizing compilation of the mentioned techniques follows in the subsequent subsections. Curve fitting procedures [26] are not considered in this study, primarily because of their higher computing time, but also because they are not generally available up to now.

The basic assumption of all differential absorption techniques is a direct relationship between apparent atmospheric transmittance and the ratio numbers, such that

$$R = \frac{L_s}{L_{s,\,PW=0}} \approx \tau_{wv}. \tag{5.11}$$

This generalization is correct, as long as the assumption is valid that the atmospherically backscattered radiance is influenced by the same total transmittance as the ground reflected radiance. A procedure which is based more directly on the simplified radiative transfer equation (as given in Section 2.1 on page 5) will be shown in Section 5.3.

Different combinations of channel sets out of the selected reference and measurement channels are used for their implementation. In the following section, a collection of already known and some new techniques are described which are all based on raw data measured at the sensor level. The term 'channel' stands for the at-sensor radiance values L_m and L_r, respectively. The index m denotes a measurement channel in an absorption region, e.g. the 940 nm water vapor absorption, and r stands for a reference channel on the side of the absorption band.

5.2.1 Band Quotient (BQ)

The single band quotient (BQ, [40]) is defined as the ratio R_{BQ} of one measurement and one reference channel:

$$R_{BQ} = \frac{L_m}{L_r}. \tag{5.12}$$

It is the prototype of the differential absorption techniques. The BQ technique is simple in implementation but very sensitive to varying background characteristics because the slope of the background reflectance spectrum is not considered. Errors are caused as soon as the background reflectance is not constant any more.

If the band quotient method is expanded to the maximum number of available channels, the non systematic errors can be reduced significantly. This 'Total Ratio' technique calculates the ratio between the sum of a number of evaluated measurement channels m_i and the sum of all reference channels r_i independent of their position in the spectrum:

$$R_{total} = \frac{\sum_i L_{m,i}}{\sum_j L_{r,j}}. \tag{5.13}$$

5.2.2 Narrow/Wide Method (N/W)

A Narrow/Wide method for measuring the total water vapor amount was first tested in 1989 [22]. The ratio is taken between a narrow and a wide band, centered at the same wavelength at the minimum of the water vapor absorption band. This method can be modified for application in imaging spectroscopy by ratioing the sum of the radiance in a group of measurement channels m_i to the sum of a larger set $(m_i + r_j)$, containing adjacent reference channels:

$$R_{N/W} = \frac{L_{Narrow}}{L_{Wide}} = \frac{\sum_i L_{m,i}}{\sum_i L_{m,i} + \sum_j L_{r,j}}. \tag{5.14}$$

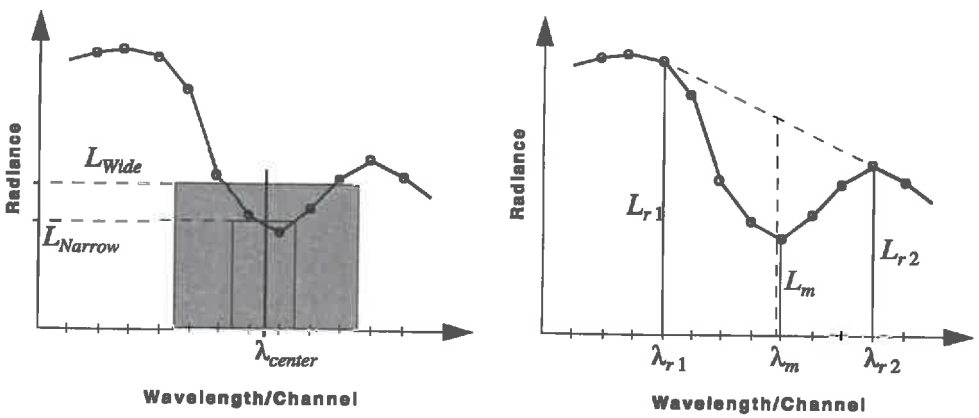

Figure 5.3: Schematic view of the Narrow/Wide and the CIBR technique in an absorption feature.

Because both references and measurements are taken within the same absorption band, the signal of the quotient is small, while spectrally varying background reflectance has little influence on the result.

This technique is of special interest for multispectral imaging where the total number of bands is limited. In its minimum configuration, only two channels are required; a narrow and a wide one, centered at the same wavelength in the absorption feature. For imaging spectroscopy applications, however, a larger set of the selected channels can be used, as indicated in equation (5.14).

5.2.3 Continuum Interpolated Band Ratio (CIBR)

The slope of the background reflectance spectrum can be reconstructed by using two reference channels on both sides of the absorption band. One measurement channel is divided by a linearly interpolated value between two reference channels at the measurement channel wavelength [10]. The ratio which is related to the water vapor amount then is defined as

$$R_{CIBR} = \frac{L_m}{w_{r1}L_{r1} + w_{r2}L_{r2}}, \text{where} \tag{5.15}$$

$$w_{r1} = \frac{\lambda_{r2} - \lambda_m}{\lambda_{r2} - \lambda_{r1}} \text{ and } w_{r2} = \frac{\lambda_{r1} - \lambda_m}{\lambda_{r2} - \lambda_{r1}}. \tag{5.16}$$

L_m is the radiance at the measurement channel with its central wavelength λ_m and L_{r1}, L_{r2} are the radiances at the reference channels at their central wavelengths λ_{r1} and λ_{r2}, respectively. The interpolation reconstructs the radiance exactly at the wavelength position of the measurement channel radiance L_m as if no water vapor were present, using the weighting factors w_{r1} and w_{r2} (see Figure 5.3).

5.2.4 Linear Regression Ratio (LIRR)

Another way of combining an arbitrary number of channels in a differential absorption technique is simply by averaging these channels, or the use of linear fitting algorithms. The consideration of the maximum number of selected channels reduces noise dependent error significantly, and also may reduce systematic and spectral calibration errors. The linear regression line through a set of reference channels is calculated and evaluated at the center wavelength of the measurement channels. The average radiance of all measurement channels is then related to the regressive interpolated value (analogous to the CIBR method). The linear regression ratio (LIRR) can then be written as

$$R_{LIRR} = \frac{\overline{L_m}}{LIR([\lambda_r], [L_r])\big|_{\overline{\lambda_m}}}, \tag{5.17}$$

where $\overline{L_m}$ is the mean of the signal of the measurement channels with the corre-

sponding mean wavelength $\overline{\lambda_m}$. The expression $LIR([\lambda_r], [L_r])$ denotes the linear regression line defined by the reference points (λ_r, L_r) which is evaluated at the wavelength $\overline{\lambda_m}$.

The LIRR in fact is a variation of the CIBR technique which uses the maximum amount of information available within an absorption feature. Erroneous channels are excluded with the channel selection technique presented in the previous chapter.

5.2.5 Non Linear Differential Absorption Techniques

All procedures described above are based on a linear (or even constant) assumption for the background reflectance. The principle of the CIBR can be extended by using more reference channels and fitting their radiance values to an arbitrary function instead of using a line. The function then could be evaluated at the measurement channel position. Such polynomial interpolations are intended to correct for non-linear background reflectance characteristics. Although at first sight this idea seems to improve the technique, two fundamental problems arise:

- The noise of a single reference channel can decrease the accuracy of a fitted interpolation function. This is especially true if the reference channels lie close one to another.
- The variations of the background reflectance are of a rather unpredictable nature. Usually, this spectrum does not follow an analytical (polynomial) function within a wavelength range of 100 nm and more.

Because of the high sensitivity to image noise, the water vapor signal practically vanishes and makes the procedures useless for current data. Such interpolation attempts therefore are no longer investigated.

5.3 The APDA Technique

5.3.1 Derivation of the Atmospheric Precorrection Technique

A differential absorption technique based directly on the radiative transfer equations given in Section 2.1.4 on page 10 is now derived. The relevant radiance measured in one specific channel measured by a sensor is given as

$$L_s = \rho \tau_{tot} \frac{1}{\pi} E_0 + L_{atm}, \tag{5.18}$$

where τ_{tot} is the effective (observed) total transmittance of the earth's atmosphere from the sun to the ground and from there to the sensor[1]. The apparent ground reflectance ρ includes the reflectance of the observed pixel, the effect of the terrain slope ('cosine effect'), and the path scattered radiance reflected by the adjacent

1. This assumption was shown to be valid for most of the real scenes (see Section 2.1 on page 5).

area. The adjacency effect is present whenever there is an atmosphere. Therefore, in real data ρ will never be zero. The backscattered atmospheric path radiance L_{atm} is not reflected by the ground and is thus independent of ρ. Note that all parameters of equation (5.18) depend on the wavelength of the used channel.

The total transmittance is now split into the water vapor transmittance τ_{wv} and a residual transmittance τ_0 which depends on aerosol and gas absorption. The radiance at the sensor level L_s can then be expressed in a simple form as

$$L_s = \rho\frac{1}{\pi}E_0\tau_0\tau_{wv} + L_{atm} = L_{gnd}\tau_{wv} + L_{atm}, \tag{5.19}$$

$$\text{where } L_{gnd} = \rho\frac{1}{\pi}E_0\tau_0 \tag{5.20}$$

is the total ground reflected radiance at the sensor level if no water vapor were present. The radiance L_{atm} does not depend on the ground reflectance, but is sensitive to the atmospheric composition, in particular to the aerosol amount and the water vapor content. Both of these quantities are functions of the path length (i.e. the ground altitude). Furthermore, the scattering effect is dependent on the imaging geometry.

Using equation (5.19), the radiances $L_s = L_i$ in three channels $i = m$, $r1$ and $r2$ are written. Assuming a spectrally linear background reflectance in the range of the wavelengths λ_i the radiance L_m in the measurement channel can be approximated by a linear interpolation as

$$L_m = [w_{r1}L_{gnd,\,r1} + w_{r2}L_{gnd,\,r2}]\tau_{wv,\,m} + L_{atm,\,m}(PW), \tag{5.21}$$

where the continuum interpolation factors w_{r1} and w_{r2} are the same as given in equation (5.16). The transmittance $\tau_{wv,m}$ is a function of water vapor for channel m but not for the reference channels $r1$ and $r2$ (i.e. $\tau_{wv,r1} = 1$ and $\tau_{wv,r2} = 1$).

Solving equation (5.21) for the transmittance in the water vapor channel $\tau_{wv,m}$ and substituting $L_{gnd,r1}$ and $L_{gnd,r2}$ from equation (5.19) we find an equation similar to the CIBR (see equation (5.15)) but with precorrection terms for the atmospheric path radiances $L_{atm,i}$:

$$\tau_{wv,\,m} = \frac{L_m - L_{atm,\,m}(PW)}{w_{r1}(L_{r1} - L_{atm,\,r1}) - w_{r2}(L_{r2} - L_{atm,\,r2})}. \tag{5.22}$$

5.3.2 The APDA Ratio

To increase the accuracy of the water vapor retrieval, an iterative approach is necessary. First, the path radiance is estimated based on the most probable water vapor content. Then, the first water vapor result is taken as a second guess to calculate the improved path radiance estimate (see Section 6.1 on page 89 for the implementation).

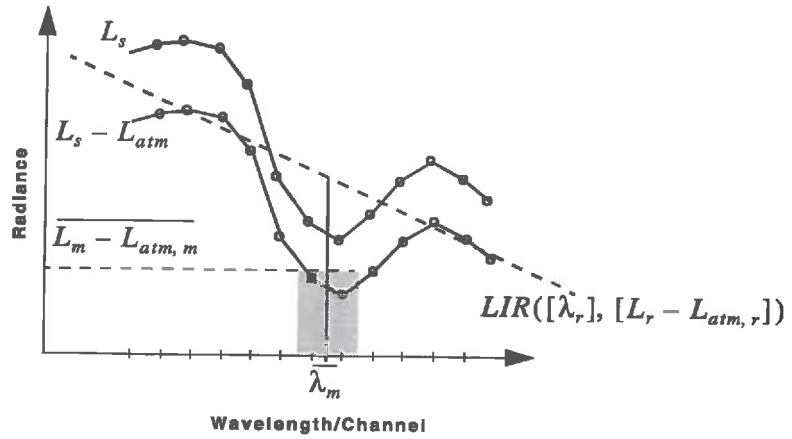

Figure 5.4: Schematic view of the APDA technique in an absorption band.

In this derivation only one measurement and two reference channels are used. However, equation (5.22) can also be extended to more channels, analogous to the linear regression ratio, given in equation (5.17). The linear interpolation of two reference channels is replaced by a linear regression line through an arbitrary number of channels and is evaluated at the center wavelength of the measurement channels. The radiance values of each channel are reduced by the corresponding atmospheric path radiance terms and inserted in the LIRR equation. This equation is a common differential absorption equation, which for the three channel case, reduces directly to equation (5.22):

$$\tau_{wv} \approx R_{APDA} = \frac{\overline{[L_m - L_{atm,\,m}]_i}}{LIR([\lambda_r]_j, [L_r - L_{atm,\,r}]_j)\big|_{\overline{[\lambda_m]_i}}}. \qquad (5.23)$$

The parameters in brackets are the center wavelengths and atmospheric precorrected radiances of i measurement channels and j reference channels, respectively.

Thus, an 'Atmospheric Precorrected Differential Absorption' technique (APDA) has been derived directly from the simplified radiative transfer equations. The theory clearly shows that a partial atmospheric correction has to be performed prior to the calculation of the differential absorption. All techniques described in the previous section can be improved by being applied to precorrected radiance data. A schematic view of the APDA technique is shown in Figure 5.4.

Figure 5.5 shows the apparent transmittance at selected background reflectances and constant columnar water vapor. The figure clearly depicts the changes of the apparent transmittance for low albedos without a pre-correction. If the pre-

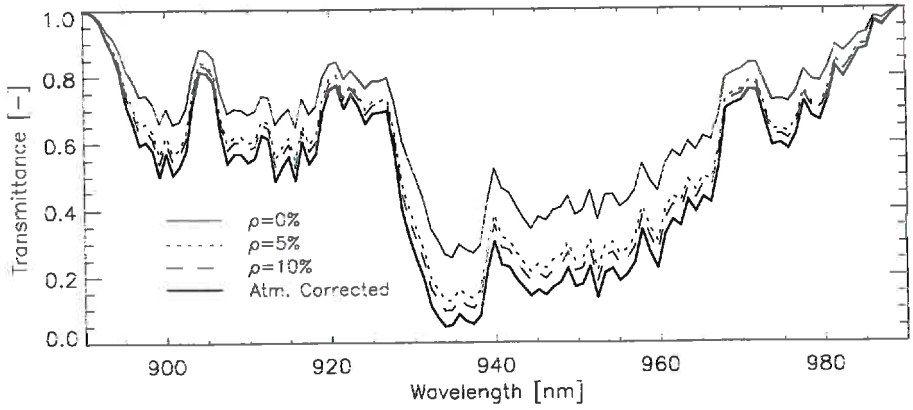

Figure 5.5: Linear interpolated (apparent) transmittance for non corrected radiance and the APDA corrected radiance at a constant columnar amount of water vapor [MODTRAN simulation].

correction is applied, the signal is mapped to almost the same apparent transmittance for varying background reflectances. It also is very close to the apparent transmittance over high reflectance targets.

5.3.3 The Precorrection Term

The atmospheric precorrection term $L_{atm,i}$ is a function of terrain height, aerosol profile and content, channel position and water vapor content. It can be estimated by calculating the total radiance at the sensor at zero albedo under varying ground altitude and water vapor content (for a given aerosol optical depth which has to be known approximately; see Section 6.1.4 for details).

Figure 5.6 illustrates how the atmospheric path radiance changes for a varying ground altitude at midlatitude summer conditions and for the urban aerosol model. The atmospheric path radiance in general is smaller for the measurement channels than for the reference channels since the atmospheric radiance is reduced by the water vapor absorption. The height variation produces changes in total aerosol content as well as in the water vapor amount. Both of these variables combine in a non linear way: the total atmospheric radiance in the reference channels decreases with height due to the lower backscattered radiance, yet it increases within the absorption band because the transmittance increase of the water vapor is stronger than the reduction of scattering.

This behaviour of the atmospheric path radiance shows how important a complete modeling of the correction term in the APDA equation over the terrain in mountainous regions is. The path radiance should not be neglected for reflectances below 10%, where it easily can become the main component of the radiance at the sensor (see again Figure 5.6).

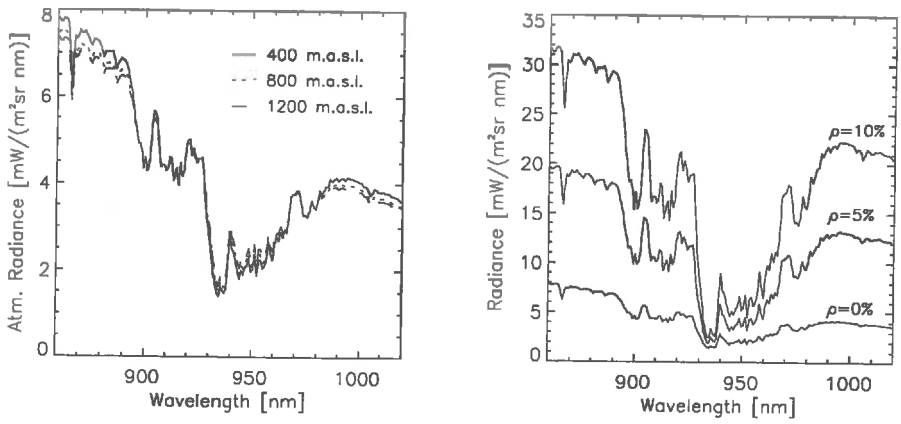

Figure 5.6: The atmospheric path radiance term for various altitudes and the total radiance for low background reflectances [MODTRAN simulation].

5.4 Error Analyses

5.4.1 The Effect of Precorrection for Variable Background Albedos

The original CIBR technique uses the simulated radiance at the top of the atmosphere for comparison with the measured radiance. Thus, atmospheric scattering effects are considered, but the influence of the additive atmospheric radiance on the ratio is neglected. At low ground reflectance, the atmospheric radiance is the major contributor to the total radiance, whereas at higher reflectances the ground reflected radiance term dominates. We introduce the total radiance at the sensor as described in equation (5.19) into the CIBR equation (5.15). In the limit $\rho \rightarrow 0$ the equation reduces to

$$R_{CIBR}(\rho \rightarrow 0) \approx \frac{L_{atm,\,m}(PW)}{w_{r1}L_{atm,\,r1} + w_{r2}L_{atm,\,r2}}. \qquad (5.24)$$

Since $L_{atm,\,r1}$ and $L_{atm,\,r1}$ are almost independent of the water vapor content, the CIBR is then proportional to the water vapor-dependent atmospheric path radiance $L_{atm,\,m}(PW)$. This term does not depend directly on the apparent water vapor transmittance $\tau_{wv,\,m}$, but is influenced by the diffuse transmittance of water vapor which is significantly higher.

When the background reflectance is high, the atmospheric path radiance is small in comparison to the ground reflected radiance, and can be neglected. The CIBR equation then reduces to

$$R_{CIBR}(\rho \rightarrow 1) \approx Const \cdot \tau_{wv,\,m}. \qquad (5.25)$$

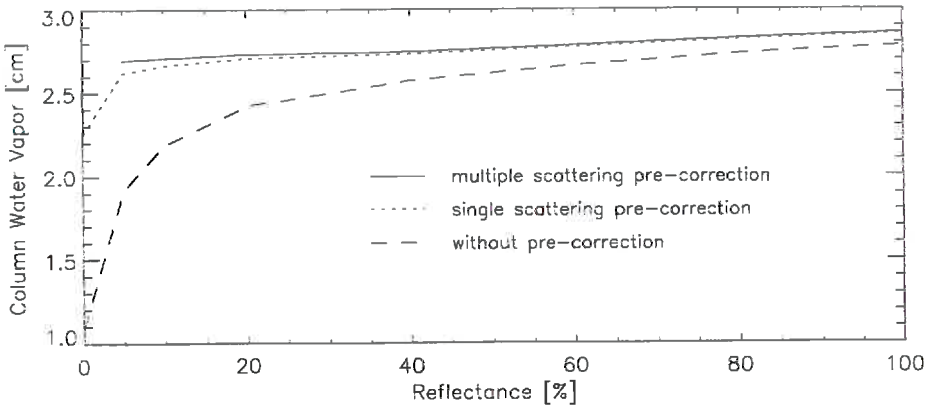

Figure 5.7: Water vapor column retrieval in dependency on the average ground reflectance value for various differential absorption techniques and a constant water vapor amount of 2.8 cm.

Thus the CIBR is proportional to $\tau_{wv,m}$ only for high background reflectances. At low background reflectances the water vapor retrieval gets less accurate, resulting in an underestimation over dark surfaces [26]. The analogous calculations for the N/W technique leads to the same conclusions.

This different behaviour over various targets could be corrected by inverting a look up table for various background albedos. The differential absorption procedure would then depend on the ground reflectance and therefore could not be applied to the data directly. An iterative combination of atmospheric correction and water vapor retrieval would be necessary. The APDA technique should correct for the above effect based on the physical derivation given in the previous section.

5.4.2 Tests on Simulated Data

The APDA equation and the CIBR were tested on MODTRAN-simulated radiance data [9]. The ground reflectance was varied systematically within the spectral range which is defined as the minimum and maximum wavelengths of channels *r1* and *r2*, respectively.

The simulation results showed that the CIBR ratio increases with decreasing average reflectance whereas the APDA ratio remains quasi constant. Figure 5.7 shows a plot of CIBR and APDA ratios as a function of the band-averaged reflectance in channel *m*. The CIBR maps low reflectances (i.e. $\rho_m < 0.2$) to higher ratios, thus lower water vapor. The APDA in contrast maps all reflectances to an almost constant ratio. A residual distribution of the ratio numbers can originate from varying reflectance slopes. This effect is similar for CIBR and APDA calculation.

The behaviour of these two techniques over a spectrally varying background was also tested using existing reflectance spectral data bases for minerals [35], man-made materials[2] and vegetation. The vegetation data base was created using the PROSPECT model [37]. The radiosity method ([7],[8]) was then used to compute canopy spectra. The radiative transfer code 6S [81] was used to compute the top of atmosphere (TOA) radiance over the water vapor band centered on 940 nm[3].

The original CIBR technique and three variations of the APDA technique are compared. The three variations are:

- *APDA*: The regular APDA equation using a fixed water vapor amount of 3 cm to compute the water vapor dependent atmospheric path radiance $L_{atm}(PW)$,
- *APDA (optimal)*: Equation (5.22) with exactly known $L_{atm}(PW)$,
- *APDA (iterative)*: Equation (5.22) with the iterative scheme described in Section 6.1.

The four techniques are compared by a measure similar to a quasi signal to noise ratio (SNR) which is based on the channel ratio number R:

$$SNR(R(PW)) = \frac{\overline{R(PW_{min})} - \overline{R(PW_{max})}}{\sigma(R(PW))}, \qquad (5.26)$$

where PW_{min} = 1 cm and PW_{max} = 5 cm are the minimum and maximum water vapor content, $\overline{R(PW)}$ denotes the average of the $R(PW)$ calculated for 379 spectra, and $\sigma(R(PW))$ denotes the standard deviation of $R(PW)$. The retrieval methods were compared by setting thresholds at ±5% and ±10% RMS water vapor deviation and counting the number of spectra within this interval. This indicates how robust the retrieval is over variable backgrounds. Table 5.2 summarizes the results obtained for the selected background spectra using the four techniques described above.

Retrieval Technique	5% Interval	10% Interval	Broad Bands 10% Interval
CIBR	35.4	9.5	13.2
APDA	8.2	1.9	3.2
APDA (optimal)	8.7	2.4	3.4
APDA (iterative)	7.9	1.8	3.2

Table 5.2: Percentage of reflectance spectra beyond 5% and 10% RMS columnar water vapor deviation for the AIVRIS band characteristics in comparison to a broad band instrument; e.g. MODIS (source: [9]).

2. Kruse F.A., 1992, IUGS, Boulder, CO, unpublished data

3. 6S was chosen instead of MODTRAN because of its faster performance on the large number of background spectra.

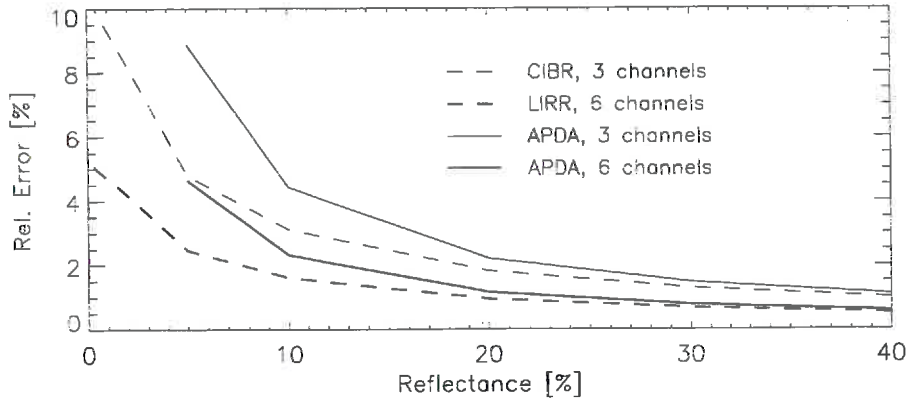

Figure 5.8: Relative error of the APDA and the CIBR technique due to image noise propagation, based on AVIRIS specifications.

The narrow band hyperspectral case has fewer reflectance spectra outside the ±10% limit than the broad band approach. The water vapor is overestimated over vegetation systematically [9] because of the liquid water absorption feature which increases the apparent water vapor in the atmosphere. This feature can be exploited to estimate canopy water content [27].

An analysis of the materials in which the iterative APDA had relative water vapor errors of more than ±10% showed that nearly all of them were classified as spectrally sloped or non-linear in the 940 nm band (see [9]). These special cases of background spectra still may lead to ground reflectance dependent errors in water vapor retrieval.

5.4.3 Error Propagation Due to Image Noise

The measured radiances L_m and L_r are affected by the sensor noise. The noise is given by the noise equivalent radiance L_{ner} for each image channel [34]. The APDA equation in general averages a number of measurement channels, reducing the absolute error for n measurement channels to

$$L_{err,\,m} = \sqrt{\frac{\sum_{m} (L_{ner,\,m})^2}{n}}. \qquad (5.27)$$

The absolute error for the reference channels interpolation is described by the error of the linear regression intercept at the central channel position $\overline{\lambda_m}$, as given by Bevington [5] for a least square fitted line for the points $(\lambda_r,\ L_r \pm L_{ne(r,r)})$:

$$L_{err,\,r} = \frac{1}{\Delta}\sum_r \frac{1}{(L_{ner,\,r})^2}, \text{ where} \tag{5.28}$$

$$\Delta = \sum_r \frac{1}{(L_{ner,\,r})^2}\sum_r \frac{(\lambda_r - \overline{\lambda_m})^2}{(L_{ner,\,r})^2} - \left(\sum_r \frac{\lambda_r - \overline{\lambda_m}}{(L_{ner,\,r})^2}\right)^2. \tag{5.29}$$

The relative error of equation (5.23) is then calculated in relation to the ground reflected radiance at constant atmospheric conditions (PW = 2 cm, rural aerosol type, visibility = 23 km) as

$$\frac{\Delta R_{APDA}}{R_{APDA}} = \sqrt{\left(\frac{L_{err,\,m}}{L_m - L_{atm,\,m}}\right)^2 + \left(\frac{L_{err,\,r}}{LIR([\lambda_r],\,[L_r - L_{atm,\,r}])\big|_{\overline{\lambda_m}}}\right)^2}. \tag{5.30}$$

The relative noise uncertainty of the retrieved APDA ratios is below 3% for a ground reflectance above 10% (see Figure 5.8). It increases to 4.5% at 5% reflectance with a further exponential increase towards zero reflectance. Thus, the method cannot be used for large, dark background targets, e.g. for water. The effect is reduced over small dark targets, where the adjacency radiance contributes significantly to the total radiance at the sensor (note that only the radiance not reflected by the ground is subtracted in the APDA ratio).

Atmospherically uncorrected ratios (CIBR/LIRR) are about half as sensitive to the image noise at low reflectances. The lower noise sensitivity occurs at those low reflectances where the systematic errors of these methods are high - the absolute error therefore is still higher for the uncorrected ratios than for the APDA technique (see the previous sections). An increasing number of measurement channels reduces the noise significantly, whereas additional reference channels have less impact.

5.4.4 Uncertainties Due to Aerosol Variations

The influence of aerosols is determined using MODTRAN simulations with constant water vapor but changing aerosol amounts (by varying the visibility stepwise from 10 to 40 km at ground level). The dependency of the corresponding derived water vapor amounts on the visibility is investigated.

The variations due to the simulated extreme aerosol situations were within 0.1 cm PW for the investigated scenes (see Chapter 6). This corresponds to a relative error of 3–5%, depending on the total water vapor content. If the APDA technique is applied, the variation is slightly increased. The APDA technique thus cannot improve the performance at variable aerosol content, although it subtracts parts of the path radiance. The differences between the aerosol scattering effects at varying visibilities are too large to be covered by the used simulated radiance values.

Because the water vapor amounts are calculated based on radiance simula-

tions at one average visibility, the introduced errors are of systematic nature. Underestimations of the water vapor amount occur if the visibility is higher than expected while for higher aerosol content the precipitable water is overestimated. The apparent water amount increases exponentially towards low visibilities. Hence, the visibility has to be known exactly especially for hazy atmospheric conditions. The deviations of the retrieved water vapor due to aerosol variations are well below 2% if the visibility is known at an accuracy of ±10%. It increases beyond 5% with less knowledge on the visibility (see Table 5.3).

Visibility	PW (CIBR) [kg/m^2]	Deviation [%]	PW (APDA) [kg/m^2]	Deviation [%]
10 km	22.2	+ 6.26	22.4	+ 6.57
15 km	21.5	+ 3.00	21.7	+ 3.13
23 km	20.9	(reference)	21.0	(reference)
40 km	20.4	- 2.35	20.5	- 2.40

Table 5.3: Variations of the water vapor retrieval results for varying aerosol amount, and relative deviations to the results at a visibility of 23 km.

The aerosol influence thus is a major contributor to the total uncertainty of differential absorption techniques. This uncertainty can be reduced by choosing appropriate radiance simulations using an estimated visibility (and thus the aerosol content) out of the image itself or from meteorological auxiliary data.

5.4.5 Variations Due to the Channel Combination

The influence of the channel combination is dependent on the specific data set and sensor. Some channel combinations may be suited for calculation, while others show errors due to problems in the sensor calibration, or MODTRAN simulation. In the following subsections, the term 'method' is used for an APDA ratio based on one specific channel combination set. 270 methods were investigated for the 1991 data and 108 methods for 1995, based on the pre-selected channels.

A spatial test image subset can be interactively defined as an adjacent region of the image, where ground reflectance variations are high and the terrain influence is low (e.g. flat agricultural fields). A good method for the measurement of a particular gas must show little sensitivity to the spatial image noise including the background reflectance variations. An indicator for the noise and background effect is found based on the standard deviation $\sigma(PW_{sub})$ of the water vapor retrieval results within the subset. It is assumed that the effective water vapor variation $\sigma(PW_{wv,sub})$ and the uncertainty signal $\sigma(PW_{\Delta L,sub})$ overlay each other independently. Therefore, the standard deviation of the water vapor content over the subset, and for each considered method, is taken as indicator value which should be minimal:

$$\sigma(PW_{sub}) \rightarrow Min\,, \text{where} \tag{5.31}$$

$$\sigma(PW_{sub}) = \sqrt{\sigma^2(PW_{wv,\,sub}) + \sigma^2(PW_{\Delta L,\,sub})}\,. \tag{5.32}$$

Based on the pre-selected channels (see Section 5.1 on page 63), all APDA methods with symmetric combinations of 4 or 2 reference channels and 2 or 1 measurement channels are tested with the above indicators. A limit for the indicators was set to get a pre-evaluated number of methods. They had to fulfill the requirements within the best 10% of all the methods. This 'practical evaluation' is based on effective quantification results in the resulting image and is one step in the error analysis process; a step which has to be made for each sensor and for each specific scene separately.

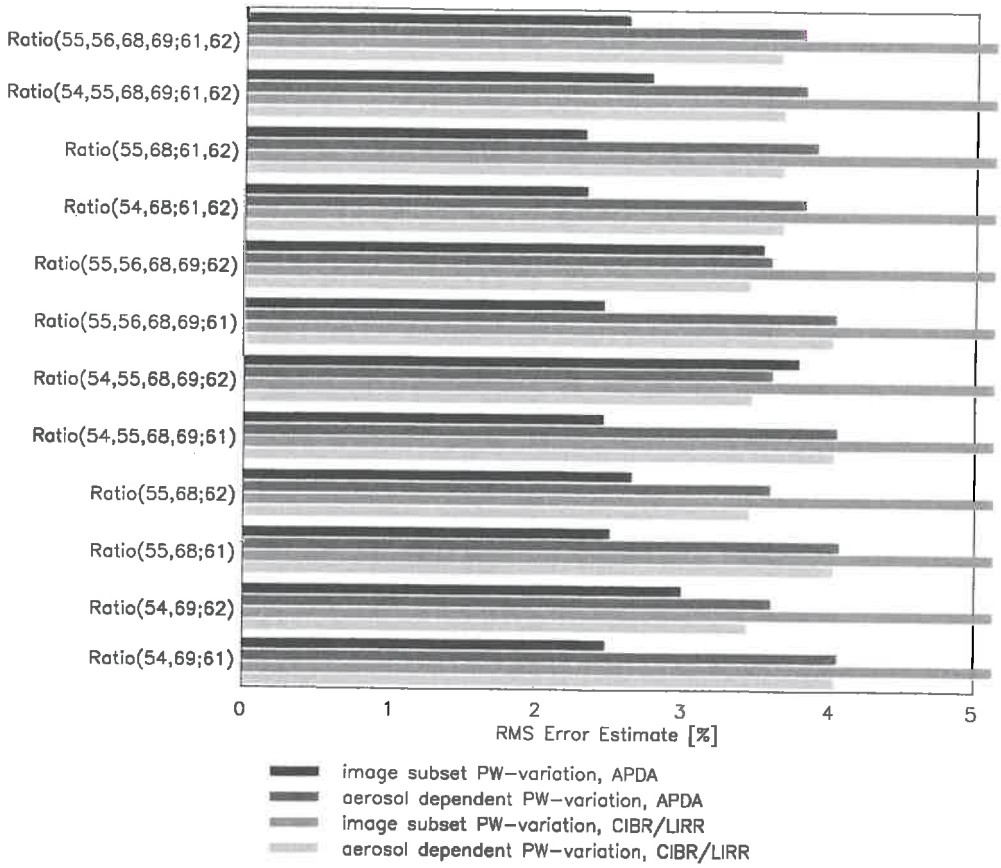

Figure 5.9: **Relative errors of some methods due to aerosol RMS deviation in comparison with the spatial image noise. Notation of the methods: TECHNIQUE(meas. channels; ref. channels).**

An increasing number of measurement channels reduces the variations as expected, whereas additional reference channels even may decrease the total errors (see Figure 5.9). The apparent water vapor variations in the image subset using the atmospherically precorrecting methods are less than half as large as those of the traditional differential absorption techniques (which reach values between 8% and 11%; outside the range in Figure 5.9).

The main influence on the absolute water vapor retrieval originates from the chosen measurement channels. The effects of the measurement channel position for 1991 and 1995 AVIRIS data are shown in Figure 5.10. In both data sets the measurement channels around 930 nm tend to an underestimation of about 10% which probably is related to the position of these bands in the steeply falling water vapor transmittance at this wavelength. At larger wavelengths (channels 62 and 64) a higher water vapor content is estimated. This pattern may originate either from the increased liquid leaf water absorption at this wavelength or from an unknown spectral channel position shift.

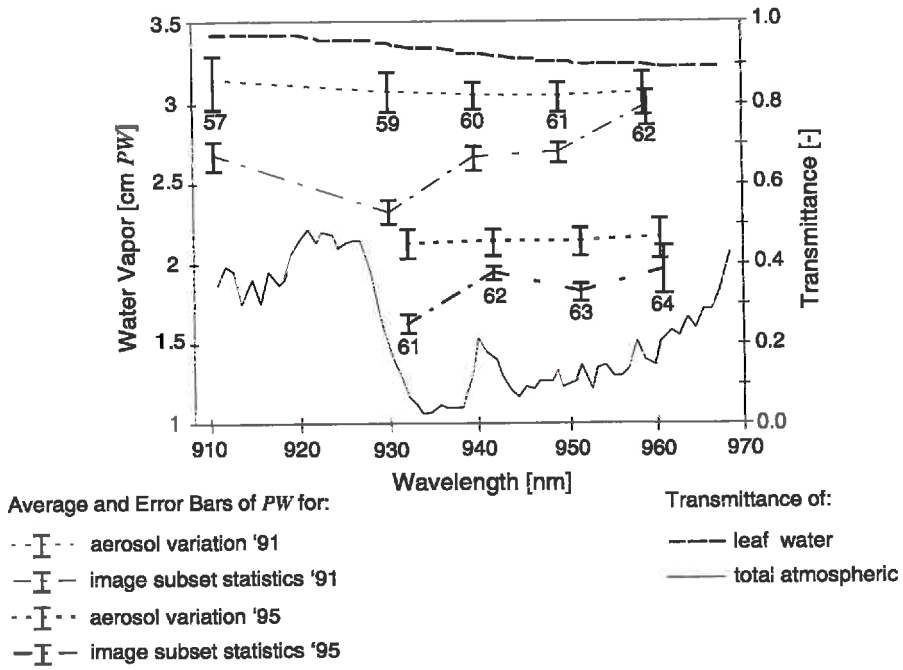

Figure 5.10: Qualification results for APDA techniques with one measurement channel for 1991 and 1995 data and for simulated atmospheric conditions. The obvious underestimation in the channels 59 (1991) and 61 (1995), respectively, and their higher variation due to aerosol loading may originate from the steep total transmittance slope. The leaf water reflectance influences mainly the channels of higher wavelengths.

The *PW* estimates over the subsets of both data sets for different reference channel combinations (at constant measurement channels) were found to be within ±2–3%. The increasing number of reference channels had only a marginal influence on the retrieval results. Therefore only methods with up to four reference channels have to be considered. The resulting RMS deviations are nearly twice as large for methods with measurement channels in the slope of the band (±3–6%) than for those in the center (±1.5–3%) (see Figure 5.10). The absorption band slope channels therefore have to be used carefully.

5.5 Relation of Transmittance and Water Vapor Amount

The differential absorption technique yields ratio values corresponding to a (quasi) gas transmittance which need to be transformed to total water vapor amounts. An exponential approach is usually used to relate the differential absorption ratio number (*R*) to the corresponding water vapor amount (*PW*). For the present study this correlation was extended to an equation with three empirical regression parameters *k*, *b* and *c*.

$$\tau_{wv} \approx R_{APDA} = e^{-(c + k(PW)^b)} \tag{5.33}$$

solved for the water vapor amount:

$$PW(R_{APDA}) = -\left(\frac{\ln(R_{APDA}) + c}{k}\right)^{\frac{1}{b}}. \tag{5.34}$$

This equation fits the MODTRAN derived APDA results for the expected variation of the atmosphere in water vapor and aerosols and therefore is valid only for the investigated range of water vapor. It allows a decrease in the computing time for the look up table-inversion from nearly one hour to less than one minute; the potentially induced errors being less than 1%. The regression parameters are retrieved only once at the beginning of the calculation as a best fit to all simulated atmospheric situations. They also could be tabulated for a variety of average water vapor amounts. For the few investigated atmospheric situations and channel combinations, the values for *k* range from 0.12 to 0.18, for *b* from 0.66 to 0.80 and for *c* from -0.05 to 0.4, for an inversion to kg/m^2 precipitable water. These values depend on the absolute water vapor amount, the range of the water vapor amounts, the used measurement channels, the aerosol content and the assumptions on background reflectance characteristics.

Figure 5.11 illustrates the relationship of *k* and *b* for more than 300 different situations. Almost no dependency of *b* on *k* is found for channels showing high absorption ($k > 0.1$). The assumption of a channel independent constant *b* therefore seems to be valid (note that this assumption was made for the channel selection procedure). The exponent *b* tends towards 1 for low absorption channels

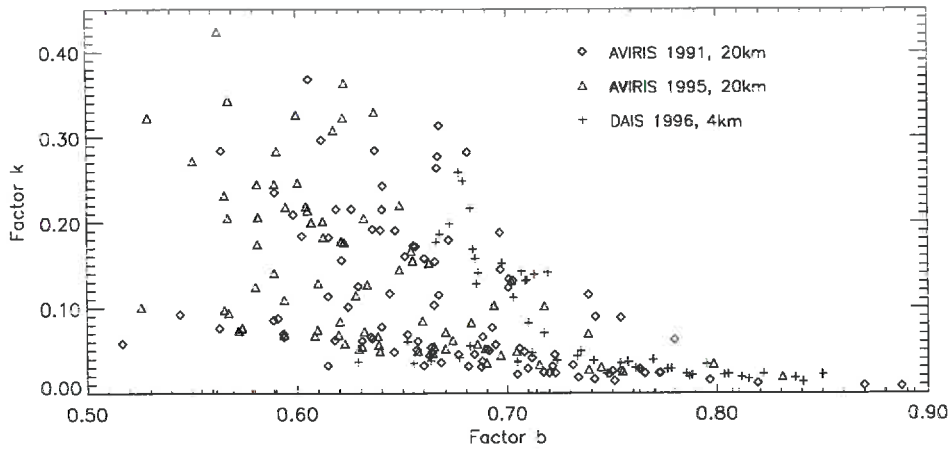

Figure 5.11: The relation of the fitting constants *k* and *b* for three different atmospheric situations and for an approximately 1 nm bandwidth resolution.

($k < 0.02$). This observation is in good agreement to the explanation that Beer Lambert's Law should be valid for channels with low absorption. For intermediate absorption *b* tends to decrease with growing *k*. The three plotted atmospheric states differ from one another systematically. The average value of *b* is higher for the sensor at 4 km altitude compared to the situation at 20 km altitude. This fact shows that it is not easy to define a general relationship between the two factors. Probably the best way for their determination is to define them for each channel combination and atmospheric state directly from radiance simulations.

This short analysis only concerns the factors k and b which already were used for calibration and water vapor retrieval in the sun photometry Section 3.1.4 on page 24. They both can be derived from physical approximations. Conversely, the factor *c* is a fitting constant without any physical meaning. It only is needed to improve the quality of the fit for the expected range of water vapor. It is zero for an ideal function, because the transmittance value for $PW = 0$ is one by definition. If *c* would be forced to zero, however, the fit will be worse for most of the cases. Note again that the relationship (5.33) has only to be valid for the expected range of water vapor in the image area – a more common relation cannot be defined analytically, as depicted within the above observations.

5.6 Further Expansion of the APDA Technique

The APDA technique as presented in the previous chapters has one big disadvantage despite its good performance for most of the targets: it does not work over totally dark targets, such as water or cast shadow areas. As a solution, equation (5.23) could be inverted, such that the amount of water vapor is calculated from the path scattered radiance itself instead of the direct ground reflected radiance. It is derived in analogy to equation (5.19) as

$$L_s = \rho\frac{1}{\pi}E_0\tau_0\tau_{wv} + L_{atm} = L_{gnd}(PW, \rho) + L_{dif}\tau_{wv}^{dif}, \qquad (5.35)$$

where τ_{wv}^{dif} is the apparent water vapor transmittance of the diffuse radiance (which is significantly higher than the direct transmittance as shown already in Section 5.3.3). If equation (5.35) is solved for this transmittance, the following expression (similar to equation (5.22)) results:

$$\tau_{wv,\,m}^{dif} = \frac{L_m - L_{gnd,\,m}(PW, \rho)}{w_{r1}(L_{r1} - L_{gnd,\,r1}(\rho)) - w_{r2}(L_{r2} - L_{gnd,\,r2}(\rho))}. \qquad (5.36)$$

This expression unfortunately still is highly dependent on the background reflectance. Thus the derivation of the column water vapor from the diffuse radiance component at the sensor is possible only if the retrieval is combined with a complete atmospheric correction which provides the ground reflectance accurately. The only way to make use of equation (5.36) more directly is a pre-classification of those elements within the image which reflectances are close to zero. These targets then can be processed separately based on the transmittance functions for diffuse radiance.

However, the signals processed by this expanded procedure are low and therefore must be exactly calibrated. Furthermore, zero reflectance has to be assumed, and last but not least, the influence of the adjacency radiance should be considered too (this is often the main contribution to the sensor signal). For low altitude airborne data, the total path scattered radiance is small over dark targets. Therefore, the signal of the water vapor is very small too. There is a minimum altitude of an airplane which would allow the water vapor measurement over dark targets. Some helicopter based spectroradiometric measurements have shown that the path radiance and the adjacency effects decrease rapidly at flight altitudes below 1000 m above ground [63].

The expansion of the APDA procedure has to be combined with a complete atmospheric correction algorithm. A possible overall concept could follow these steps:

1) Correct the atmospheric path radiance of the channels in the atmospheric window regions (on the basis of the assumed aerosol model, or even using an image based procedure) and calibrate these channels to ground reflectance.
2) Interpolate a first guess of the ground reflectance in the water vapor channels.

3) Calculate the iterative APDA technique as described above.
4) Calculate the water vapor amount based on the path radiance and the interpolated reflectance (a technique which first has to be defined).
5) Weight the results of the iterative APDA and the path radiance differential absorption technique based on the apparent reflectance, such that the original APDA is used for high reflectances and the path radiance for dark targets.
6) Correct the channels in the water vapor regions based on the known water vapor amount and the aerosol content.

This atmospheric correction procedure should allow the production of improved results for hyperspectral data, especially in the water vapor features. Its implementation will be the topic of future studies.

5.7 Conclusions on Differential Absorption Techniques

It was shown that the new atmospheric precorrected differential absorption (APDA) technique allows for accurate measurement of spatial water vapor distributions even over flat areas with strong background reflectance variations. The achieved accuracy is sufficient for current applications. The techniques presented above may also be useful to retrieve other gases with absorption features in the visible or near infrared part of the spectrum, such as O_2 or O_3.

The basic APDA technique is fully automated and performs in less than one minute for an AVIRIS scene (if the look up table is already created). Further automatization could be achieved by using a set of MODTRAN standard look-up-tables together with predefined channel combinations. Additionally, an average aerosol loading could be estimated with the described procedure, by using the DEM and statistical information of the image to define a suited image subset automatically. The implementation is currently in a semi-operational state and could be extended to a complete application for the usage of differential absorption techniques in imaging spectroscopy.

Chapter 6:

Application to Imaging Spectroscopy Data

6.1 Implementation

The described differential absorption techniques and processing algorithms proposed in the previous chapters are implemented in a modular system based on IDL® (Interactive Data Language, RSI Inc.). The single modules cover the various steps of the processing chain for water vapor:

- noise estimation and image data quality assessment,
- MODTRAN radiance and sensor simulation,
- Look Up Table (LUT) creation with MODTRAN,
- channel selection and error propagation analyses,
- common differential absorption techniques,
- atmospheric precorrection and APDA calculation,
- path radiance estimation by LUT inversion based on DEM,
- terrain adjustment and profile retrieval.

The following sections describe some of the algorithms. More information on selected modules can be found in Appendix D.

6.1.1 The APDA Algorithm

The following iterative procedure is used to compute the water vapor image from prepared data sets (see Figure 6.1 for a flow chart of this algorithm):

1) Use a radiative transfer code to compute a LUT containing the total radiance L_s at the sensor for an average reflectance background (e.g. ρ=0.4) and the atmospheric path radiance L_{atm} as a function of water vapor content, terrain height and wavelength at an estimated visibility.
2) Find the ratios R corresponding to the water vapor amounts of each MODTRAN run by applying the APDA technique to the LUT (subtract the atmospheric path radiance term from the total radiance term and calculate the ratio values).
3) Fit all the ratio values to the water vapor amounts using the function from equation (5.33) and store the fitting parameters k, b and c.

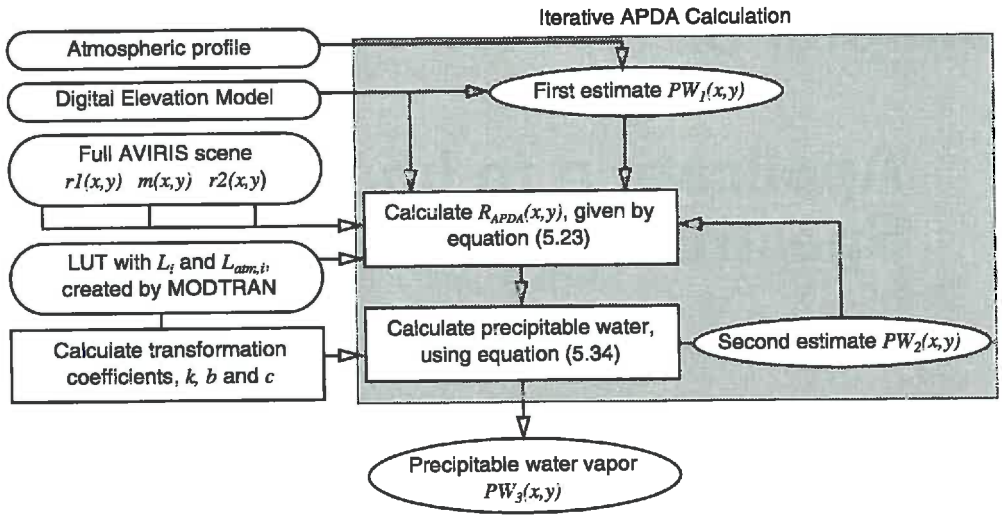

Figure 6.1: Flowchart of the iterative APDA algorithm. Only two iterations are illustrated because they provide sufficient accuracy.

4) Assume a starting water vapor content (PW_1) for all image pixels from the DEM and a standard atmospheric profile.
5) Calculate the APDA ratio following equation (5.23) and transform the ratio values to water vapor content (PW_2) using equation (5.34).
6) Substitute the values of L_{atm} in equation (5.23) with the new water vapor dependent values derived from the LUT and the DEM height information.
7) Recalculate the image ratio R_{APDA} and transform the ratio values to the final water vapor content $PW_3(x, y)$.
8) Steps 5 through 7 can be repeated until $\overline{PW_n} - \overline{PW_{n-1}}$ is less than a given threshold (e.g. < 10^{-4} cm).

Our computations have shown that two iterations converge sufficiently which makes further calculations dispensable.

Figure 6.2 shows an overview flowchart of the water vapor retrieval technique, including the APDA algorithm described above. The whole technique also contains the channel selection procedure described in Section 5.1 on page 63, and a channel combination evaluation procedure which makes use of the error analyses results as described in Section 5.4.5 on page 82.

This calculation is based on calibrated radiance values and known locations of each image pixel. Thus, the required preprocessing steps are:

- absolute calibration to radiance equivalents,
- spectral calibration within ±1 nm in the absorption bands,
- geometric correction on DEM at an accuracy of below 30m.

If one of these requirements is not fulfilled, the data cannot be used for a proper estimate of the columnar atmospheric water vapor. If the accuracy is lower than described above, the error range can grow beyond a 5–10% limit.

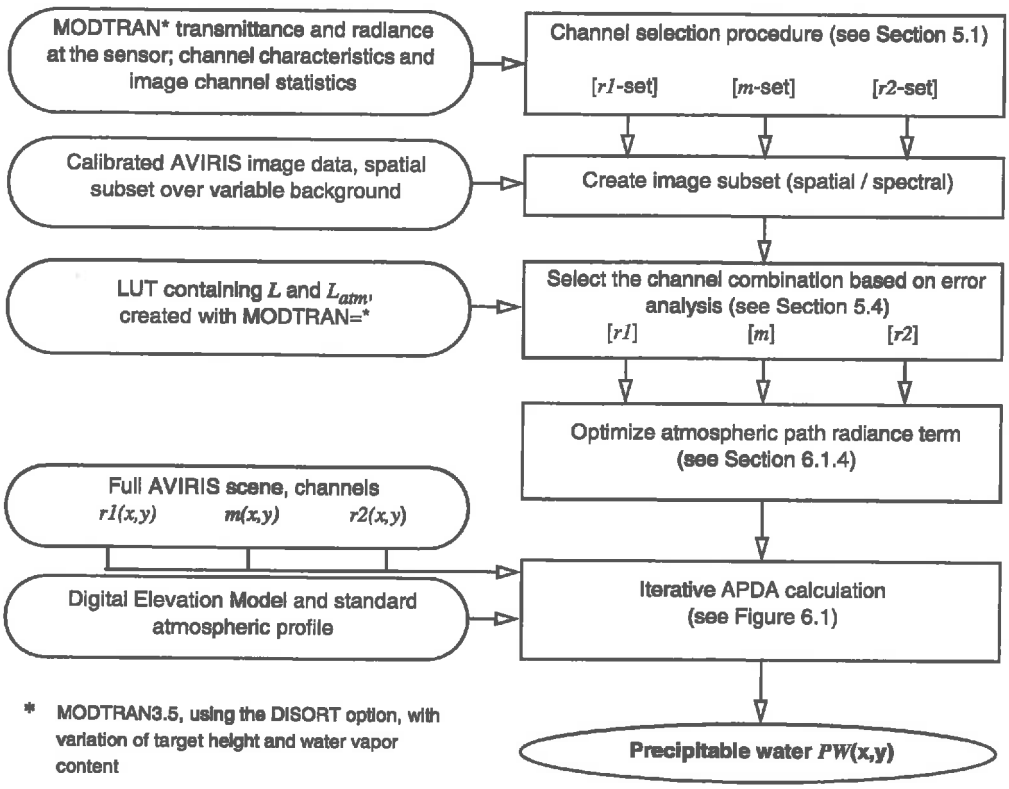

Figure 6.2: Flowchart of the complete water vapor retrieval methodology using the APDA technique in combination with the channel selection procedure.

6.1.2 Definition of the Look Up Table for the APDA Technique

The key part of the whole processing algorithm is the LU). It can be used for various processing steps:

- channel selection,
- method optimization (e.g for the definition of the channel combination),
- atmospheric precorrection,
- path radiance estimation,
- inversion of differential absorption results to precipitable water vapor.

The LUT used in the above algorithm consists of radiance data in four dimensions (see Figure 6.3). The radiance is calculated at a discrete number of height levels at vertical intervals of 200–500 m to account for the changing influence of aerosols with height. The atmospheric water vapor is then reduced for each height level by applying factors of 0.75 and 0.5, respectively, which defines the dimen-

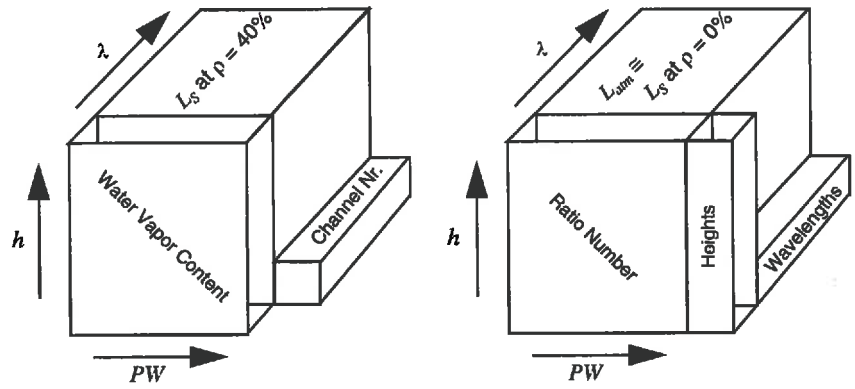

Figure 6.3: The four-dimensional Look Up Table, as used for atmospheric precorrected water vapor retrieval.

sion of possible horizontal water vapor variations. These calculations are done over the whole wavelength range of the absorption feature at a resolution of approximately 1 nm and a constant reflectance (e.g. 40%), using the MODTRAN radiative transfer code. The atmospheric radiance is stored in the fourth dimension (depicted by the right cube in Figure 6.3). It is retrieved with the same parameters as the total radiance by setting the ground reflectance to zero.

The LUT then is convolved to the specific channel characteristics, reducing the amount of data points in the wavelength dimension to the number of channels. The channel numbers and the central wavelengths per channel are stored in the lowest level of the LUT as an additional element. Furthermore, the total amount of water vapor per atmospheric situation is extracted directly from the MODTRAN output and is stored in a virtual channel of the radiance cube. The heights of the single levels are written to the position beneath the water vapor content. The same layer in the atmospheric radiance cube is used to store the ratio values of the APDA technique, applied to the cube itself. The latter is simply done by subtracting the atmospheric radiance cube from the sensor radiance cube and then applying the linear regression ratio of the chosen channels to all spectra within the cube.

This LUT, however, does not contain the angular dimension which should be available for wide swath sensors. The view angle for each pixel has an essential influence on the path scattered signal and should be considered as soon as it is more than about 10–15° from nadir. Thus, the used LUT is not appropriate for the correct processing of DAIS data which are scanned at angles of up to ±26°.

Almost the same LUT can also be used for complete atmospheric correction algorithms. A third cube containing the amount of total path scattered radiance is necessary for that scope. These additional radiance values are needed to correct

for the adjacency effects as well as to correct for the effect of diffuse irradiance. An absolutely complete atmospheric correction and water vapor retrieval LUT would also contain the view angle dimension for wide swath sensors.

6.1.3 Atmospheric Precorrection of the Image

The described LUT is used to process the partial atmospheric correction on the image data while performing the APDA calculation. As already described in previous sections, the data has to be geocoded. The DEM data is used to create an artificial image of atmospheric path radiance, using the LUT information. This path radiance depends on height, water vapor amount and wavelength. Thus, the interpolation of the path radiance per pixel is not only done relative to the height but also to the amount of water vapor, given by the relative stretching factor to the first assumption on water vapor. In unpredicted situations, the term even may be extrapolated from the given LUT values. The result is a virtual image of the theoretical spatial distribution of the atmospheric path radiance based on the DEM. This image is subtracted from the calibrated raw image.

This calibration step, called 'atmospheric precorrection', is only performed for the used channels, and is not stored permanently. The corrected channels are processed directly by the differential absorption technique. Finally, the retrieved ratio image is inverted to the precipitable water using the inversion constants initially derived from the LUT.

6.1.4 Optimization of the Atmospheric Path Radiance Term

The atmospheric path radiance term (L_{atm}) in the APDA equation (5.23) depends on the aerosol and water vapor distribution which are functions of terrain elevation. Initially, the aerosol content is defined using a standard model at an estimated visibility. An adjusted atmospheric path radiance term $L_{atm,i}$ for each channel i is found empirically to be:

$$L_{atm,\,i} = L^{M}_{atm,\,i}\left(1 + c\frac{w_{atm,\,i}}{w_{atm,\,max}}\right) \text{where} \tag{6.1}$$

$$w_{atm,\,i} = \frac{L^{M}_{atm,\,i,\,max} - L^{M}_{atm,\,i,\,min}}{L^{M}_{atm,\,i,\,min}}. \tag{6.2}$$

The factor a is an empirical adjustment parameter, and $L^{M}_{atm,i}$ is the basic first assumption for the amount of atmospheric path radiance, as derived from MODTRAN for channel i. The weighting factor $w_{atm,i}$ indicates how strongly the state of the atmosphere influences the atmospheric path radiance term in each channel. It is found from the ratio between a maximum and a minimum atmospheric path radiance: the value $L^{M}_{atm,i,max}$ is taken at dry atmosphere with high aerosol concentrations (stored with the lowest altitude in the LUT), in direct contrast to $L^{M}_{atm,i,min}$ (highest altitude and humid atmosphere).

In equation (6.1), the weighting factor $w_{atm,i}$ is normalized by the maximum weighting factor $w_{atm,max}$ of all channels within the LUT. A $w_{atm,i}$–weighting of 1 is attributed to the channel with the highest path radiance change between 'max' and 'min' conditions, whereas no path radiance variations would be assigned to $w_{atm,i} = 0$. This procedure allows definition of one single adjustment parameter (c) for all channels which weights the path radiance of each channel depending on its relative amount.

This channel independent parameter c is only valid for one specific method applied to the investigated image scene. It is derived by minimizing the standard deviation $\sigma(PW_{sub})$ over an image subset (as described in Section 5.4.5 on page 82) while adjusting the path radiance term with equation (6.1). The obtained values for c in the investigated AVIRIS scenes were -0.10 and -0.18, respectively. This indicates that the initial assumptions on atmospheric path radiance were correct within a range of about 20%.

The LUT stretch factor c obtained by this procedure finally is used for the processing of the whole image. The flow chart in Figure 6.2 shows the position of this procedure in the complete APDA processing chain. Such an adjustment of the atmospheric path radiance is not absolutely necessary, but helps to increase the accuracy for low level water vapor variations. The procedure could also be used for image based retrieval of the amount of aerosols for atmospheric correction if a spatially adaptive filtering would be applied.

6.1.5 Correction of the Slew Rate Effect

The application of the APDA technique on whiskbroom scanner data (AVIRIS) showed the unexpected effects of edge-enhancement along the borders of agricultural fields (see Figure 6.4). Since cast shadows (e.g. in irrigation channels or from plants) would not show this phenomenon in a systematic way, a sensor inherent effect is supposed. According to Chrien[1] the instrument's focal plane may be equipped with amplifiers that are too slow. If the scanner slew rate is higher than the reaction time, bright areas bounded by dark areas will appear delayed in scan direction. The delay increases with the magnitude of the signal change, and is therefore maximal for high absolute reflectance differences in channels of high atmospheric transmittance. The effect thus is significantly higher for the reference channels because they have more than twice the absolute signal than the measurement channels (which by definition are located in the absorption feature).

To correct for this effect, a spatial shift between the single not-geocoded channels was introduced. A procedure to detect sub-pixel shifts [80] was applied for the channels used in the water vapor retrieval algorithm. This analysis which maximizes the correlation between the single channels, showed that the reference

1. Tom Chrien, JPL, CA, personal communication

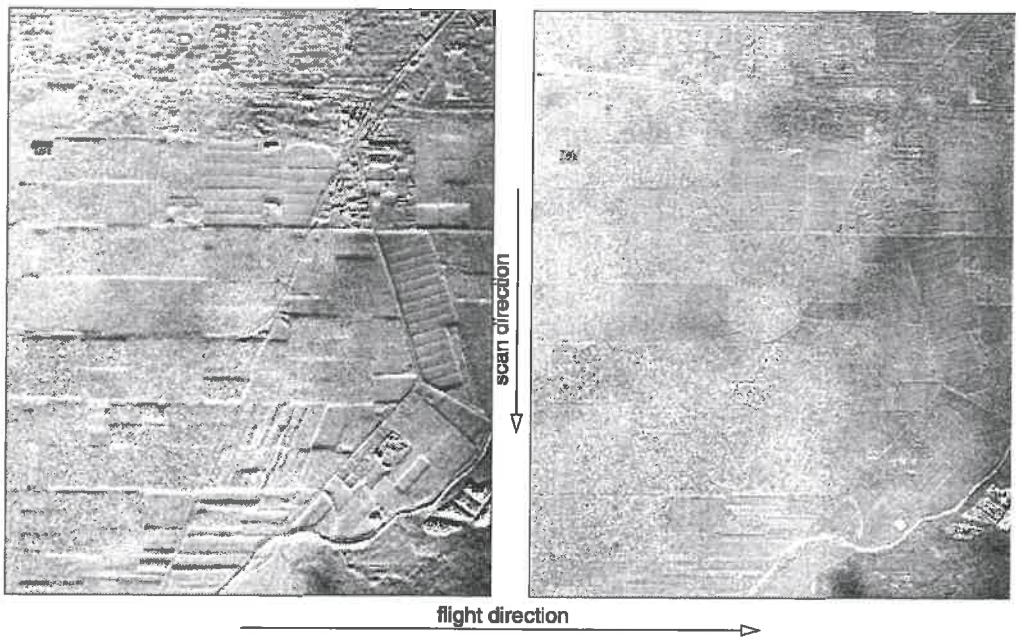

Figure 6.4: **Slew rate effect in 1995 AVIRIS data and its correction (water vapor retrieval examples). The pattern in the left image originates from the slow amplifiers of the AVIRIS sensor arrays in combination with a high slew rate.**

channels (# 54,55,56,68,69,and 70 for 1995 AVIRIS data) were shifted in scan direction by about 0.15 pixels with respect to the measurement channels (# 60,61,62,and 63). In flight direction nearly no shift was detected. All relevant channels were then registered from the raw image by the calculated sub-pixel shifts, using bilinear interpolation. The corrected water vapor images were significantly improved compared to the unregistered images (see Figure 6.4).

6.2 Application to AVIRIS Data

The methodology described in the previous sections was applied to two AVIRIS scenes:

1) Site: Central Switzerland, 'Risch', Date: July 5th, 1991 (AVIRIS 070591 run 6, scene 1)
2) Site: Santa Monica, 'Camarillo', Date: May 26th, 1995 (AVIRIS 052695 run 8, scene 3)

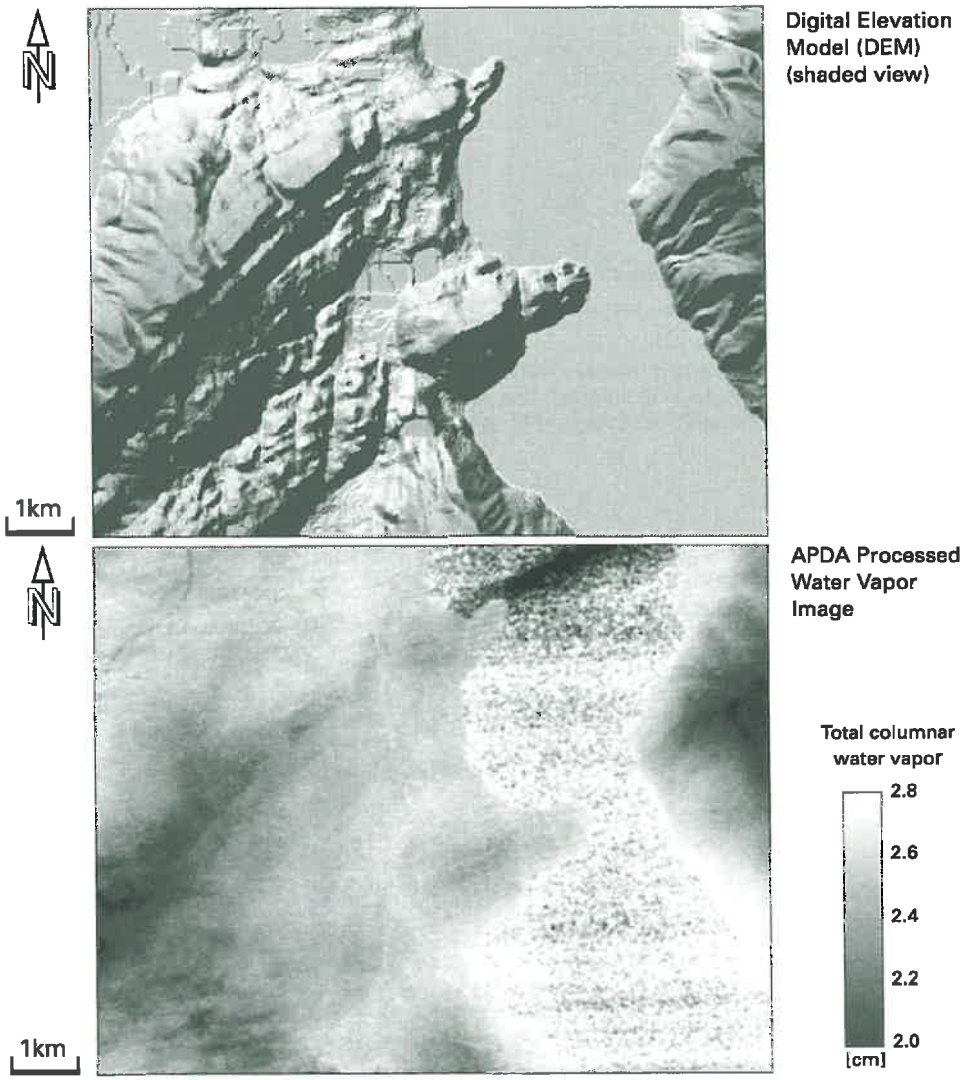

Figure 6.5: Water vapor distribution for 1991 AVIRIS data using the APDA technique in comparison with the digital elevation model in shaded relief view. No valid results are achieved over the lake area (signal vanishes in noise).

6.2.1 Scene over Central Switzerland

The selected differential absorption method for 1991 was applied to the AVIRIS'91 scene of Central Switzerland [49]. The average SNR of the 1991 data was only one fifth compared to the most recent AVIRIS data. However, this data set is valuable for atmospheric imaging spectroscopy because of the extensive simultaneous in-situ measurements of atmospheric trace gases, which were taken during the Swiss POLLUMET experiment [52]. Various soundings in and close to the test region were combined to obtain the actual profile for the time of overflight. The columnar water vapor error of these radiosonde measurements is estimated to be ±10%.

The AVIRIS scene was geocoded with a parametric correction algorithm by Meyer [49]. The fully height dependent APDA technique could therefore be applied to this mountainous scene. The water vapor retrieval results of the APDA(60,61;54,67) method are shown in Figure 6.5. The mean columnar water vapor along the shore of the lake as measured from the image is about 2.85 cm. The integration of the in-situ water vapor radio sounding profiles yields a total column of 2.97 cm over the lake level (414 m.a.s.l.). This small difference of about 5% between radiosonde data and the AVIRIS–retrieved column water vapor is within the error of radiosonde data in general (about ±10% for column water vapor) and also within the error range of the retrieval procedure described above. An even better agreement is found when comparing the retrieval difference between the highest and the lowest terrain pixels to the corresponding integrated radiosonde profile.

The highest concentrations of water vapor (in g/m^3) are found in the boundary layer (lower troposphere) with a strong decrease in height. Therefore, the spatial water vapor distribution correlates very well with the DEM of the region. The difference in terrain height between the highest and the lowest terrain pixels (954 m.a.s.l. and 414 m.a.s.l., respectively) causes a decrease in water vapor column of about 0.9 cm. The same amount is obtained by integrating the radiosonde profile between these two levels within an error of less than 5%.

The atmospheric precorrection effect on the 1991 AVIRIS data is illustrated in Figure 6.6. If the differential absorption methods are applied to the raw image without atmospheric precorrection, the water vapor is underestimated over relatively dark surfaces (e.g. the forests or the airfield). Over the river (upper left in image) both methods fail, but the effect is still reduced by the precorrection. These observations of the error range are in agreement with the theoretical values, predicted in the previous chapter (see e.g. Section 5.4 on page 77).

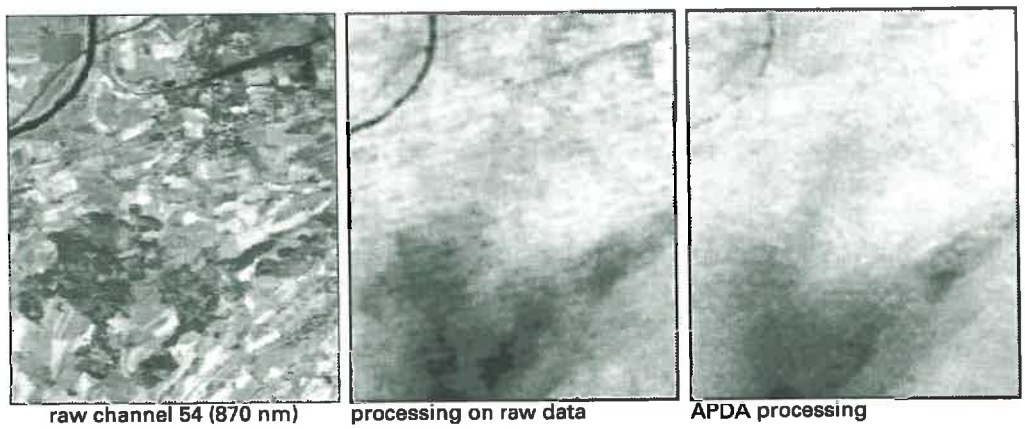

Figure 6.6: Effect of the atmospheric precorrection on the water vapor retrieval over forests (lower left of subset) and the airfield (upper right edge) in 1991 AVIRIS data.

6.2.2 Scene over Camarillo (CA)

The same methodology was also applied to newer AVIRIS data originating from summer, 1995 campaigns over the Santa Monica area (CA). The investigated scene was geocoded using the PARGE algorithm and then processed with the APDA technique. Some of the evaluations could also be done on the basis of the raw data (not geocoded) because the agricultural area in the scene is rather flat (maximum elevation about 50 m.a.s.l.).

Figure 6.7 shows the results of the APDA water vapor retrieval. The effect of the atmospheric precorrection is obvious when compared with the uncorrected image. When performing the traditional differential absorption technique, high impacts of the background characteristics are reported with underestimations over dark surfaces (upper image). After the atmospheric precorrection most of this impact disappears (lower main image). The resulting water vapor distribution is much less biased by the land use features than the previous water vapor calculation (note that the smoother appearance is not a filtering effect but is only due to the applied precorrection).

The range of water vapor is within about 1.6 to 1.9 cm, and even small variations over the plane between 1.7 and 1.8 cm can be observed in the slew rate corrected APDA image. A radiosonde profile from the date of data acquisition reports an amount of 2.05 cm above sea level. The difference of about 10% is within the radiosonde accuracy and can also originate from water vapor variations during daytime. Another reason for the systematic difference is channel 61 which was used for the calculation because it helps to qualitatively improve the resulting image. This channel was shown to introduce underestimations of 5–8% (see Section 5.4.5, Figure 5.10) compared to methods without that measurement channel. The water vapor retrieval results are therefore systematically low in

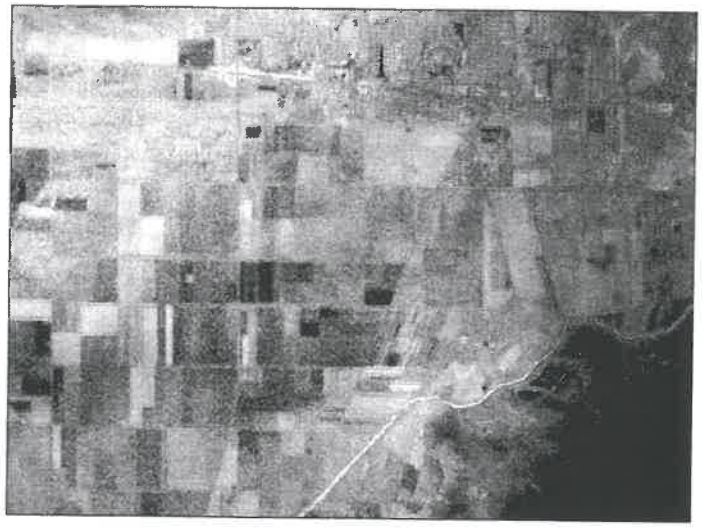

Uncorrected Water Vapor Processing

(using the LIRR techniques)

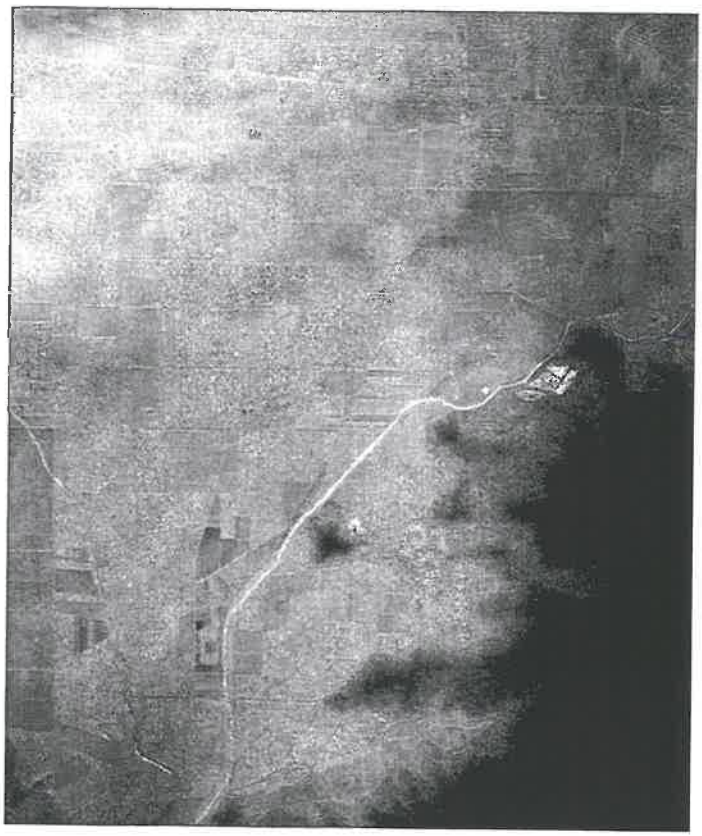

Atmospheric Precorrected Water Vapor Image

(using the APDA technique)

Figure 6.7: High sensitivity atmospheric precorrected water vapor distribution for AVIRIS 1995 data over Camarillo (CA) using channels 54,55,61,62,68 and 69 in comparison with the non corrected processing (using the same channels). The elevated area (lower right of image) appears black because the low water vapor column is outside the chosen scale.

comparison to the radiosonde data. The offset could be easily corrected by applying a measurement channel dependent factor which would reduce the difference between image and radiosonde data to about 5%.

This accuracy and sensitivity cannot be achieved with the CIBR, N/W or LIRR technique, where background effects override the signal of the water vapor. However, in the final image there are some remaining effects caused by low ground reflectance which show that the water vapor retrieval procedure may be improved. Some of these errors occur over water targets and in cast shadow areas. This effect cannot be solved by the APDA technique, as already shown in Section 5.4.3. The increased noise over dark targets is also obvious from the APDA image (as simulated in Section 5.4.3). Both problems could only be solved by a reflectance dependent processing of dark areas which is only possible in combination with a total atmospheric correction. Some further residual variations in the image may be induced by varying leaf water content of the observed plants or non–linear background reflectance characteristics. The first problem could be solved by a combined retrieval of leaf water, while the second one cannot be reduced with known methods.

The largest influence on the retrieved water vapor, however, is due to the elevation of the terrain (lower right corner of the image). A method which allows correction of this effect is given in Section 6.5.

6.3 Application to DAIS Data

The DAIS image data is not easy to process because of its intermediate level calibration. However, some attempts were made to retrieve the atmospheric water vapor from DAIS data. The water vapor information would be needed specifically for atmospheric correction algorithms. The atmospheric path radiance for low altitude sensors (such as the DAIS) is only 2–3% of the total radiance at 40% ground reflectance. Thus, the atmospheric precorrection has an influence on the water vapor retrieval only over dark surfaces (the amount of path radiance for AVIRIS data is about 10% for the same conditions).

The number of available measurement channels are limited to six channels within the 940 nm absorption band. Only two of them are sensitive enough for water vapor retrieval (see Table 6.1). The measurement channel #27 was favoured for the application since it is less sensitive to spectral calibration uncertainties and has a higher sensitivity at average midlatitude summer water vapor amounts than channel #26. The chosen reference channels are given in Table 6.1. They were selected directly on the wings of the absorption feature. Because the number of available channels are very limited, no further quantitative analyses for the channel selection had to be done. .

The results of the APDA(27;23,30) technique applied to the DAIS data (see Figure 6.8) shows overestimations of the water vapor over dark targets, indepen-

	Channel Number	Wavelength
Reference 'Left'	**22, 23**	**859, 878 nm**
Measurement	**26, 27**	**930, 948 nm**
Reference 'Right	**30, 31**	**1001, 1017 nm**

Table 6.1: Selected channels for water vapor retrieval with the DAIS imaging spectrometer. The preferred channels are bold.

dent of atmospheric precorrection. In addition, the amount is underestimated over bright targets. These results are in direct contradiction to the theory which predicts underestimations over dark targets. Furthermore, the absolute content are less than half the integrated column from radiosonde measurements. These large discrepancies cannot be explained by wrong assumptions for the atmospheric state or problems with the procedures used. They have to be attributed to an erroneous calibration of the DAIS sensor.

The overestimation is probably produced by a combination of too high dark current subtraction with too high gain factors in the measurement channel. For the correct water vapor processing, the image data has to be recalibrated. It is assumed that only the measurement channels have to be adjusted. A recalibration offset is calculated such that dark targets appear similar to the surrounding pixels, while the lower gain has to be determined in order that relatively bright targets no longer have lower water vapor amounts than relatively darker targets. Such a recalibration follows the empirical equation

$$L_{recal} = (b - b_{off})DN + (a + a_{off}) = L_{cal} + a_{off} - b_{off}DN. \quad (6.3)$$

The original DN have to be known for this correction. If they are not known, the gain correction may be approximated by $b_{off}DN \approx cL_{cal}$. A radiance offset a_{off} = 0.8 mW/(m^2 sr nm) had to be applied to the calibrated data for better results over the dark targets, and a gain correction factor b_{off} = 0.2 was applied to the measurement channels for a better absolute accuracy. The results in the image could be improved significantly (see Figure 6.8), although they did not reach the high independency of background reflectance obtained with the AVIRIS data.

The miscalibration in these bands also leads to errors in atmospheric correction algorithms; the too high signals in the measurement channels induces an apparent overcorrection of these channels if the appropriate (standard-) atmosphere is used. This effect was observed at various DAIS data sets from 1996 and 1997 measurement campaigns[2]. Only the introduction of a dry (not realistic) atmosphere or the described recalibration corrects this effect.

The experiments have shown that there are still some efforts left to be done in calibrating DAIS data to radiance standards, specifically in the 940 nm water vapor absorption region. The special investigation of the water vapor feature thus

2. The mentioned scenes are currently under investigation at RSL.

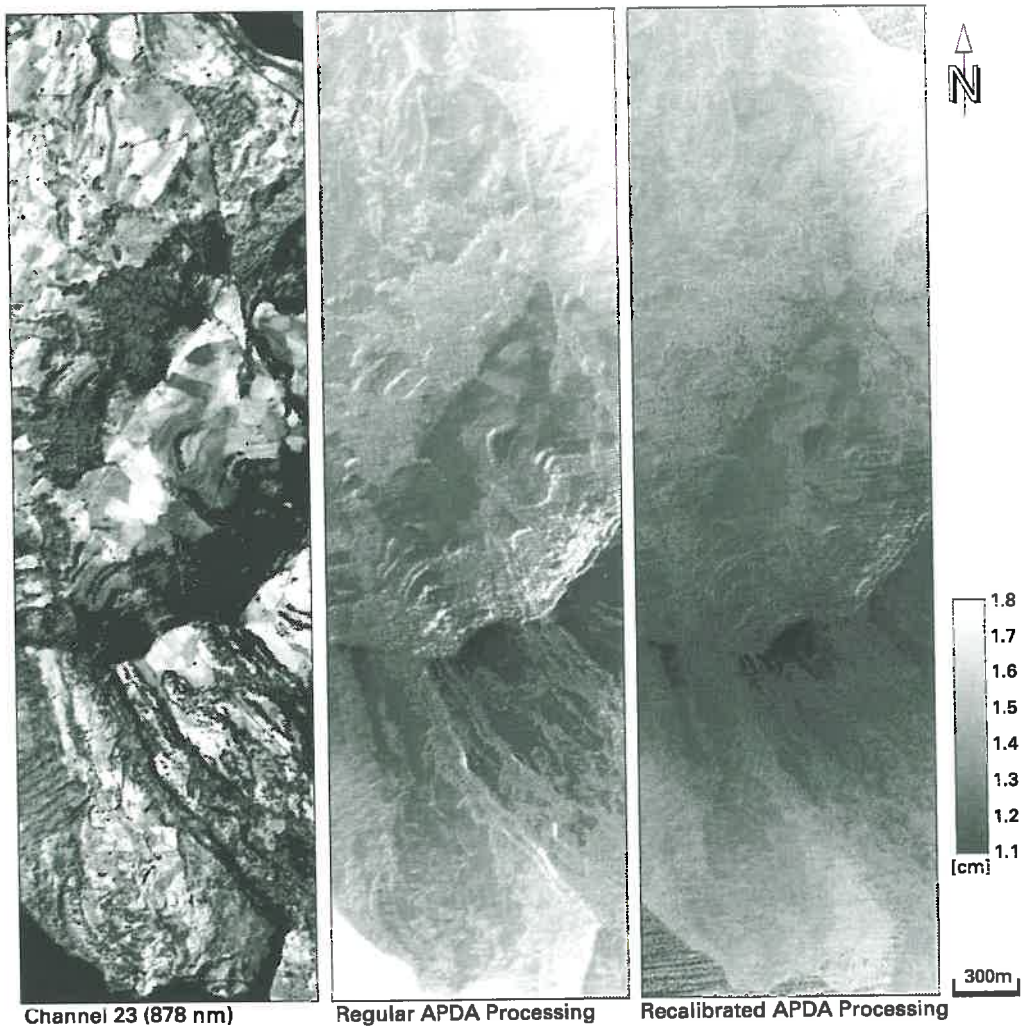

Figure 6.8: Water vapor retrieval results for DAIS 1996 data over the Rigi Mountain (Central Switzerland). The amount is overestimated over dark targets and cast shadows (middle). After recalibration (right) these effects are reduced, while the amount is still underestimated over bright targets.

also allows for the validation of the image data calibration. It would be theoretically possible to create a systematic quantitative method of in-flight calibration based on these observed effects. Such a method could help improve the performance of imaging spectrometry sensors in this very sensitive spectral region.

6.4 Image Based Profiling Procedures

Terrain modelling techniques allow the combination of digital elevation model data and geocoded water vapor distribution images. In the following sections, procedures are described for calculating columnar profiles, as well as for deriving the concentration of water vapor along terrain slopes. The resulting profiles agree satisfactorily with in situ measurements, and have the potential to provide new information about water vapor distribution in the atmosphere.

6.4.1 Columnar Water Vapor Profile Retrieval

The columnar water vapor is averaged at a given number of discrete height levels of the digital terrain model to obtain a mean columnar water vapor profile $PW_p(h)$ within the image.

$$PW_p(h) = \overline{PW(x, y, h_{x,y})} \qquad (6.4)$$

$$\text{with:} \quad h - \frac{\Delta h_p}{2} \leq h_{x,y} \leq h + \frac{\Delta h_p}{2},$$

where Δh_p is the resolution of the columnar profile retrieval and h denotes the height level. $PW(x, y, h_{x,y})$ is the previously retrieved columnar water vapor at the coordinates (x,y). The corresponding height $h_{x,y}$ per data point is read

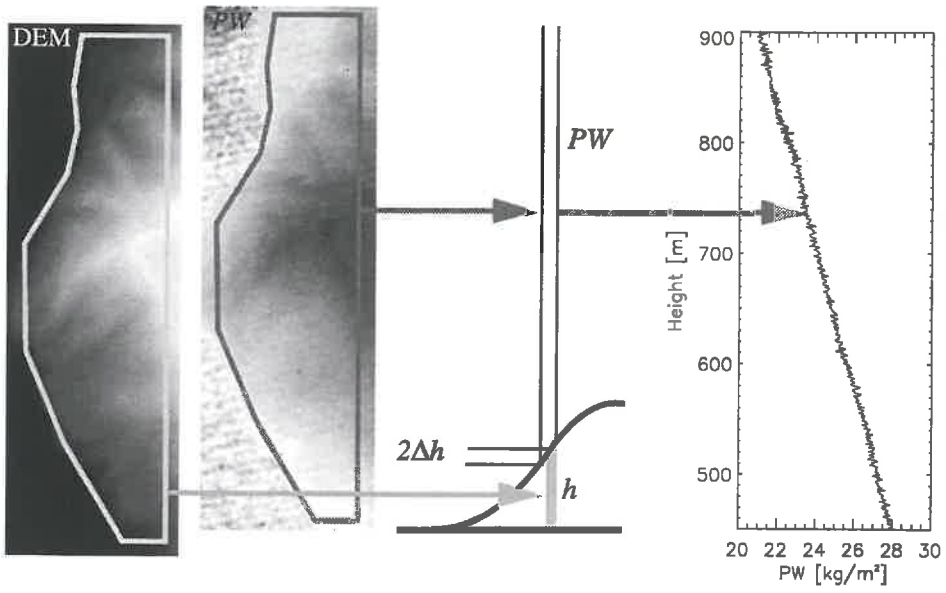

Figure 6.9: Principle of the columnar water vapor profiles retrieval from image data and DEM information.

directly from the DEM and introduced into equation (6.4).

Figure 6.9 shows the principle of columnar water vapor profiling for 1991 AVIRIS data. A fairly steep slope up to the Zugerberg mountain can be used for the calculation. The lake area has to be masked because it is not possible to retrieve the columnar water vapor at a satisfactory accuracy over water. Some noise appears in the calculated profile with height since it is derived at a lowest vertical resolution of 1 m. A low number of pixels per height level and the non-smoothed 1991 data quality are the reasons for this shape. Already a resolution of 20 m improves the columnar profile appearance significantly and is chosen for the further calculations.

The results of the columnar water vapor retrieval are shown in Figure 6.11. The column water vapor agrees with the radiosonde measurement within an accuracy of better than 10%.

6.4.2 Concentration Profile Retrieval

Water vapor concentration profiles along terrain slopes are determined from the total columnar water vapor content by calculating the variation of the columnar water vapor with height. A floating regression line through a number of columnar data points is calculated. Its resolution is given by the height difference Δh_u between the two limits of the regression line. The slope of the line denotes the water vapor concentration u at the height level h:

$$u(h) = \frac{PW_p\left(h - \frac{\Delta h_u}{2}\right) - PW_p\left(h + \frac{\Delta h_u}{2}\right)}{\Delta h_u}. \qquad (6.5)$$

The retrieved profiles within one specific image vary depending on the vertical resolution (see Figure 6.10): high erroneous variations are reported at vertical resolutions from below 20 m. At 50 metres there are still height dependent variations which are not reported from the radiosonde profiles. At 100 m and lower resolution, the profile is similar to the radiosonde measurements. Thus, the potential vertical resolution of this profiling method is not better than 100 m.

Not every terrain is suited for this kind of profile processing; there must be height variations from 200 metres up within the area. This range is based on the maximum resolution of the profile retrieval. Furthermore, the region of interest shall not be larger than 5 to 10 square kilometres since otherwise a mixture of horizontal distribution and vertical profile within the atmosphere occurs. Thus, the best results can be achieved along steep uniformly rising mountain slopes.

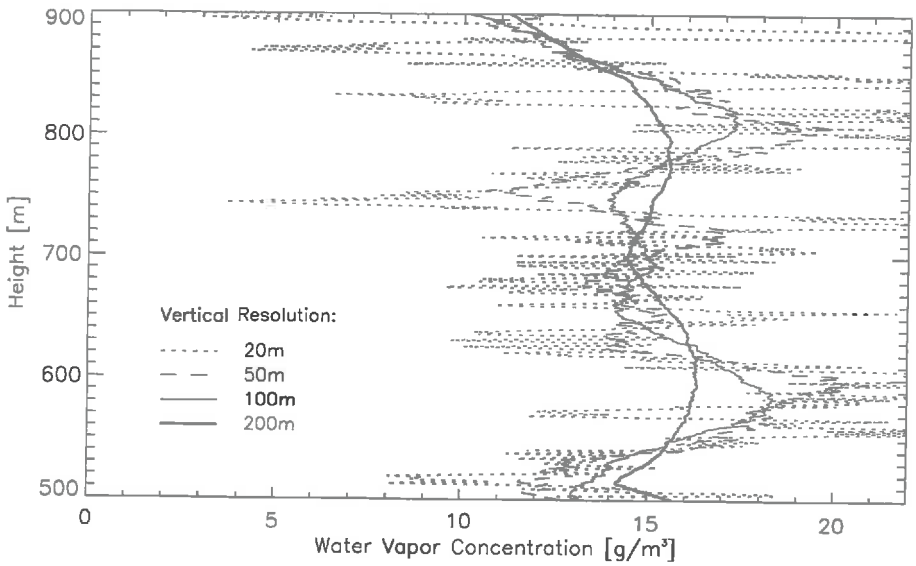

Figure 6.10: Influence of the vertical resolution on the accuracy of water vapor concentration retrieval.

6.4.3 Comparison of North and South Slope Profiles

The above methodology is applied to the AVIRIS data over complex terrain in Central Switzerland and in California. For both processed images the columnar and the concentration profiles were retrieved over one specific mountain. In 1991, the radiosonde profile was taken within the image area at the time of the overflight. The 1995 sounding originates from a measurement of the previous day (at similar meteorologic conditions) from a meteorological station located close to the scene.

Figure 6.11 shows the results for the 1991 data. The columnar profiles of the north and the south slopes differ mostly in the lowest part of the mountains and agree at the top. They both are underestimated relative to radiosonde measurements by about 5%. For the water vapor concentration profiles, a good average agreement between radiosonde and AVIRIS calculated profiles is found. The deviation range is within ±7%. The concentration over the south slope is higher than the radiosonde concentration, while the north slope profile shows lower concentrations. This observation is in agreement with theory which assumes convective streams along the south slope leading to advection of humid air from the lake area[3].

In 1995 data, the difference between the columnar results is more than 10%.

3. Markus Furger, PSI, Villigen (CH), personal communication

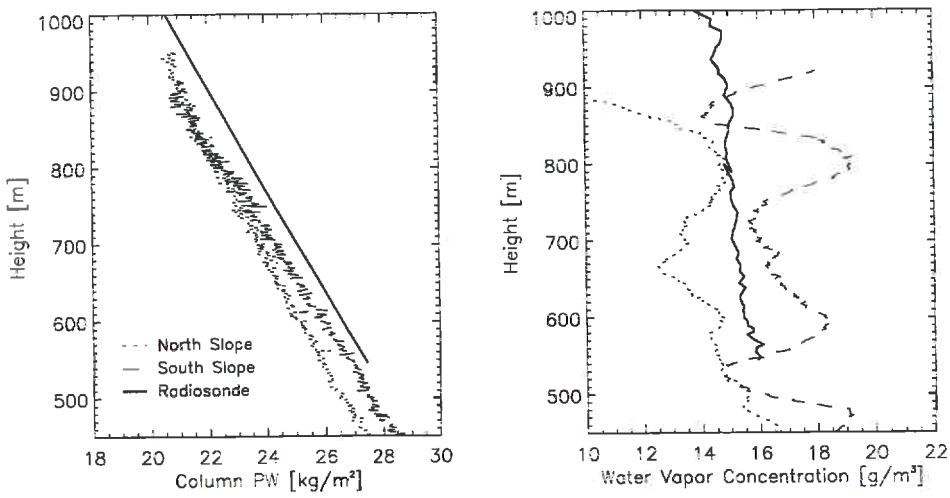

Figure 6.11: Columnar profiles (left) and concentration profiles (right) calculated over different terrain slopes from 1991 AVIRIS data in comparison with radiosonde measurements.

We suppose that the inferior result in the Californian scene originates from the non-simultaneous radiosonde data. Much higher water vapor concentrations were detected in the upper boundary layer when the sonde was launched. The concentration profiles for 1995, however, agree within a 10% range depending strongly on the aspect of the slope. The south slope of the mountain shows higher concentration than the north side. This pattern therefore is consistent between the two data sets.

It remains to be investigated whether the variations with height are real signals of water vapor disturbances on the slope or if they occur from terrain dependent horizontal variations (e.g. on heterogeneous slope steepness).

6.5 Reduction of the Terrain Influence

In mountainous areas it is not possible to interpret the spatial water vapor distribution satisfactorily since the columnar water vapor decrease from hills overrides the spatial information. The columnar profiles combined with DEM-height information can be used to reduce the spatial water vapor information to a flat scene.

For this purpose the following procedure is applied: An artificial average water vapor column image is produced by mapping the (already averaged) columnar profile information PW_p back on the DEM. Each height level of the DEM $h(x,y)$ is assigned to the corresponding columnar profile value. This idealized

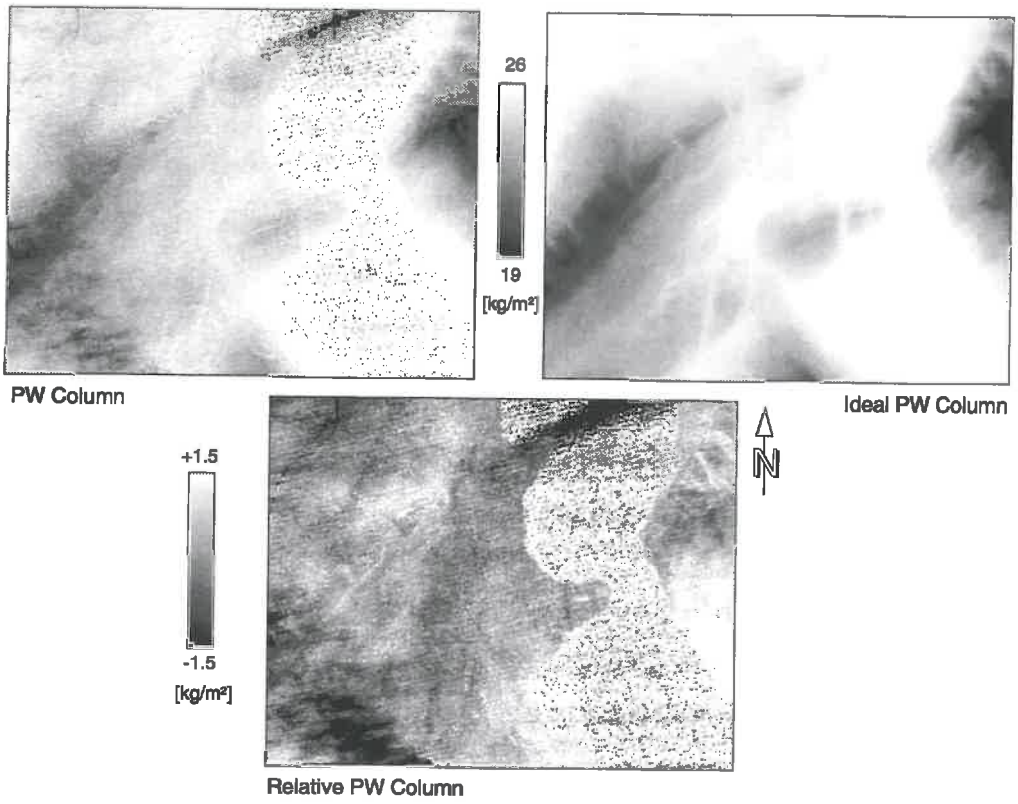

Figure 6.12: Terrain reduction process for 1991 AVIRIS data. The ideal water vapor distribution is subtracted from the effective columnar water vapor distribution to obtain the adjusted image with the relative water vapor.

water vapor image is subtracted from the originally calculated water vapor distribution $PW(x, y)$ which yields a map of the relative water vapor distribution $PW_{rel}(x, y)$ (see Figure 6.12 for an example view of this procedure):

$$PW_{rel}(x, y) = PW(x, y) - PW_p(h(x, y)), \tag{6.6}$$

with PW_p values derived from equation (6.4). The topographic influence now is minimized, and the higher water vapor concentrations on southern slopes appear clearly in the Zugerberg area at the eastern border of the lake. The dark area in the southwest corner of the image is caused by cirrus clouds which reduce the (optical relevant) path for water vapor detection. The relative distribution map now allows for the interpretation of horizontal water vapor variations which could not be studied in the original image (compare Figure 6.5).

6.5.1 Influence of Geocoding on Terrain Adjustment

Geocoding is a indispensable task for atmospheric processing of imaging spectrometer data. The thickness of the atmosphere depends on the height of the terrain and therefore can be calculated from the digital elevation model (DEM). This parameter can only be linked to image data, when they are geocoded precisely to DEM geometry. This link is used for atmospheric correction algorithms as well as for the algorithms described in this paper.

Figure 6.13 shows the sensitivity of the terrain adjustment procedure to a geometric shift. An inaccuracy of about 3 pixels (here: 90 m) makes the procedure inaccurate over the mountain area. Variations in columnar water vapor are produced with over- and underestimations, respectively, on both sides of the mountain ridge. The relative difference between these two areas may be up to 10 percent for the example pixel shift. This effect can also be used for the validation of georeferencing procedures. It allows area based controls of the accuracy in mountain areas where ground control points often are difficult to obtain.

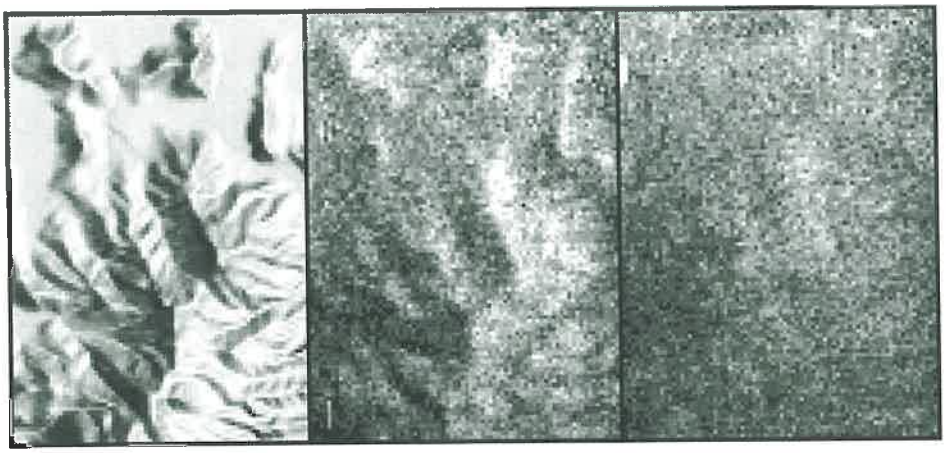

Figure 6.13: Influence of geocoding inaccuracies on the terrain adjusted water vapor retrieval results. Left: DEM shaded view, middle: geocoding accuracy of 60 metres, and right: geocoding accuracy of 20 metres.

6.5.2 Result for AVIRIS 1995 Data

The relative water vapor is given as negative and positive difference values independent of the terrain (Figure 6.14) after the terrain reduction. It is possible to recalculate the columnar images by adding the average of the lowest height levels water vapor column. For the Camarillo data, a value of 1.75 cm was added. In this case, the correction is a reduction of the columnar water vapor amount to the sea level.

These new kind of images allows for a real horizontal distribution interpretation. Higher amounts over the south slopes of the mountains or in specific valleys help to understand small scale convections. Clean air subsidence appears as dark features within the image. Such patterns may help to understand air transport processes, especially during summer smog situations.

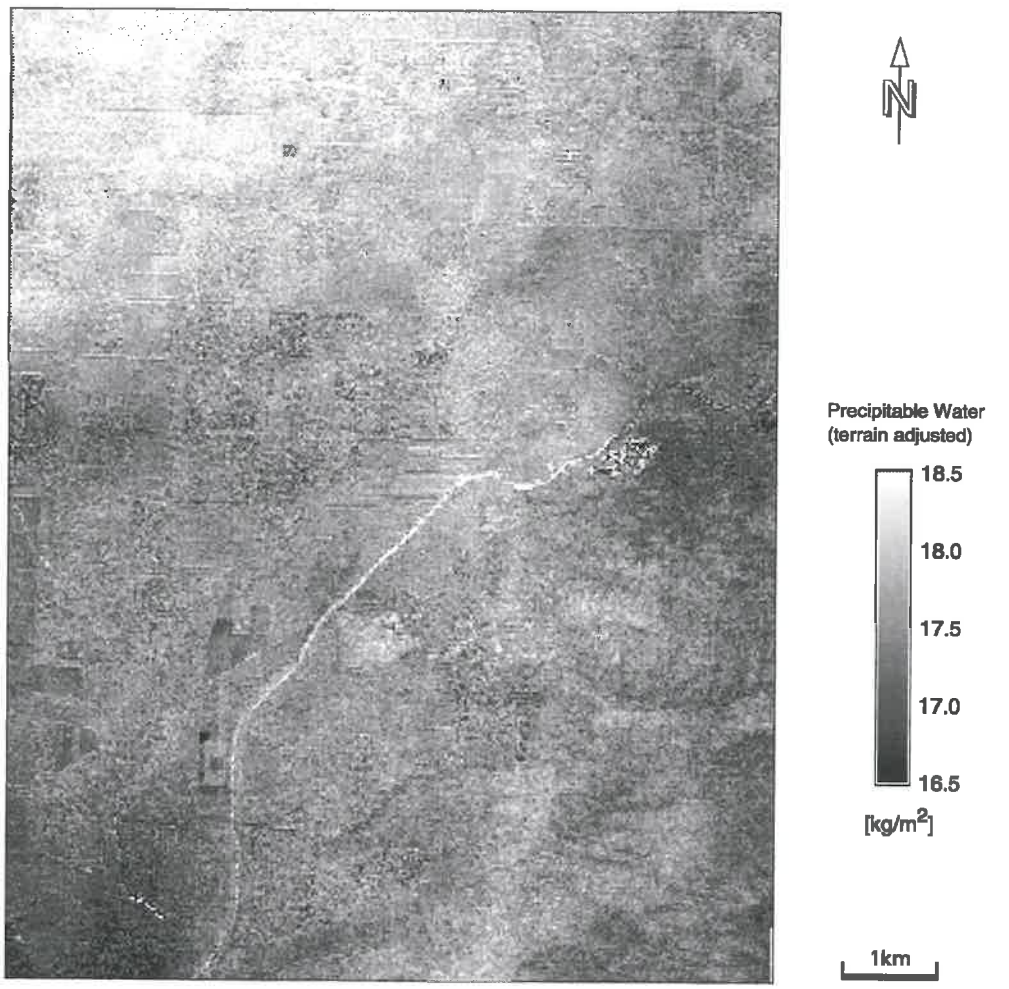

Figure 6.14: Terrain adjusted APDA water vapor retrieval results for geocoded AVIRIS 1995 data over Camarillo CA. The horizontal resolution is 30m (see also Figure 6.7).

Chapter 7:

Conclusions

Differential absorption methods have been shown to provide valuable information about tropospheric water vapor distribution from imaging spectroscopy data as well as from sun photometer measurements. The new processing techniques, using the digital elevation model together with the geocoded water vapor images, allow the quantification of horizontal distributions at a resolution of about 20 m and the estimation of vertical concentration profiles at resolutions down to 100 m. The methodology furthermore improves the reliability of differential absorption methods, especially in comparison with other retrieval methods (such as curve fitting).

The depicted methodology to retrieve water vapor consists of the following steps: First, the raw image is calibrated to absolute radiance units. Second, it is geocoded to a DEM geometry (this step may not be necessary over completely flat terrain for certain processing algorithms). Third, the columnar water vapor is retrieved from the image by the APDA technique. Finally, columnar profiles can be calculated depending on height, and the terrain adjustment can be performed. It is furthermore possible to calculate specific concentration profiles along terrain slopes.

Most of the described steps may not only be used for the retrieval of atmospheric water vapor. Moreover, they are applicable to differential absorption processing with respect to other atmospheric constituents, as well as for the exploitation of absorption features of materials on the earth's surface.

7.1 Radiometry of the Atmosphere

The radiative energy transport through the atmosphere is very complex and can not fully be described in easily applicable equations. Basic assumptions therefore have been introduced which help to describe the radiance at remote sensing sensors as well as at ground based instruments. For the simulation of the spectral signatures radiative transfer codes are used. The simulated signatures are of interest mainly for measurement of aerosols and water vapor.

Special procedures allow the determination of water vapor and aerosol content from ground based radiometric sun photometer measurements. This technique is in favor for ground-truthing because of better reliability compared to in-situ measurements. The calibration for the Reagan sun photometer has been done in high altitude campaigns.

7.2 Preprocessing Results

The preprocessing of imaging spectroscopy data has been analyzed from calibration to atmospheric correction. A special emphasis has been put on geometric correction since atmospheric effects are highly dependent on the scanning geometry. The resulting images of the parametric geocoding algorithm (PARGE) are within accuracies of 10 to 50 meters. The new application even has the potential to reach an increased accuracy if the provided parameters (i.e. location and attitude of the airplane) would be of higher reliability.

Atmospheric correction was shown to have a high impact on the retrieval of atmospheric parameters, and, vice versa, the atmospheric parameters have to be used for accurate atmospheric correction algorithms. This relationship leads to the necessity of a complete atmospheric processing methodology including parameter retrieval and atmospheric correction.

7.3 The APDA Technique

An efficient technique to determine the amount of columnar water vapor has been derived from simplified radiative transfer equations. A ranking process for the single channels allows for a quantitative selection prior to the application of the APDA technique to a specific scene. A sophisticated procedure defines ideal channel position and combination for any hypothetical or real sensor and scene. This analysis improves the results of the water vapor retrieval significantly through eliminating the influence of erroneous channels.

The behaviour of the new APDA technique was simulated over various backgrounds, an extensive error analysis was made and the new technique was finally applied to imaging spectroscopy data. The relative water vapor error was shown to lie consistently within ± 5% for most of the analyses made. It only increases for low altitude sensors over very dark targets, where the signal is absolutely minimal. A further extension of the technique is only possible if the reflectance of each pixel can be estimated in a complete atmospheric correction algorithm. In this case the atmospheric path radiance itself could be used for trace gas retrieval. Thus, the goal to define an appropriate differential absorption technique for water vapor retrieval therefore could be achieved.

7.4 Future Development

A challenge remains to retrieve the water vapor over dark surfaces such as water or shadowed areas since in these cases the path radiance there is the only quantity containing information about the atmosphere. This complementary measurement of water vapor will only be possible with further improvements in methodology. Such techniques may differ from differential absorption and curve fitting techniques. The full amount of radiance at the sensor level has to be used for such a retrieval technique. The most promising approach is the combination with a complete atmospheric correction scheme which considers adjacency effects and the whole geometric situation.

In a next step, the PARGE geocoding and the APDA algorithm will be improved to an operational state. These algorithms may be both part of a future integral preprocessing application which combines geometric and atmospheric calibration of imaging spectroscopy data. Intermediate layers of water vapor content and aerosol distribution may only be by-products within such an application. This extensive work on operationalisation has to be done although all described algorithms are already in at least semi-operational state.

7.5 Potential Applications of the Water Vapor Results

The water vapor retrieval methodology allows the gathering of important information about concentrations in the lower troposphere, and could help to improve and test evapotranspiration models. The latent energy flux within the canopy is of special interest to quantify the impact of land use changes on the microclimate and (indirectly) on bio-ecological parameters.

The use of the methods in meteorological models could be a further application. However, this would only be valuable if hyperspectral data is available at a high temporal resolution covering the same area as current meteorological satellites. Such new instruments in fact only would need three (or even two) narrow channels in the 940 nm absorption region to collect this new kind of meteorological data. First steps in this direction are done with the MERIS [54] and the MODIS [42]sensors on future spaceborne platforms.

A third application of these measurements is the monitoring and the investigation of air transport processes and air pollution. The special techniques of terrain modeling would allow the usage of the technique in alpine valleys. These results could be of special interest for research projects, where single campaigns are organized, and where it is sufficient to overfly the region only once.

The depicted examples show that the differential absorption methodology for the retrieval of atmospheric water vapor has the potential to fulfill needs in various scientific and operational applications. This technique therefore has to be further investigated. Its usefulness will increase as new imaging spectrometers on board of airborne as well as spaceborne platforms are flown on a regular basis.

Appendix A:

Special Definitions

The following definitions are valid throughout the thesis and may differ from definitions given by other authors:

absorption line	narrow absorption feature, usually caused by one single physical process (change of energetic state)
absorption band	broad absorption feature, usually a combination of physical processes
aerosols	(large) atmospheric particles, which mainly cause scattering effects - not including the atmospheric gases
albedo	spectrally non-resolved reflectance of a target, physically: integration of the reflectance over the reflective part of the spectrum
atmospheric gases	all gases of the atmosphere, including nitrogen, oxygen, carbon dioxide, water vapor and trace gases
atmospheric radiance	path radiance at the sensor which never has been scattered by the ground
attitude	angles of the airplane in relation to a horizontal surface and the north (or the flight) direction
band	spectral region with one characteristic signatures or measurement range of a multispectral instrument
channel	narrow bandwidth spectral measurement unit defined by its spectral position and bandwidth; also hyperspectral imaging layer
columnar profile	total gas column in relation to the altitude
continuum interpolation	linear interpolation of an absorption feature to its central wavelength position
differential absorption	spectral selective absorption described by the relation of absorbing channels to non-absorbing channels
flightpath	path of the airplane given by geographical position and height

georectification	direct (e.g. polynomial) image transformation to a map coordinate system
georeferencing	assigning of map coordinates to each image pixel by reconstructing the image geometry on a DEM
geocoding	production of a map-like image, using the results of the georeferencing process
imaging spectrometer	airborne instrument used for imaging spectroscopy applications
imaging spectroscopy	theory and methodology for the spectrally continuous imaging of the electromagnetic spectrum
measurement channel	channel located within an absorption feature
method	here: differential absorption technique using a specific channel combination
parameteric geocoding	geocoding of an exact image using attitude data and exact airplane position for reconstruction of the scanning geometry
precipitable water vapor	total column of water vapor in the atmosphere, usually measured in cm or in kg/m^2
preprocessing	radiometric calibration, georeferencing, and atmospheric correction of hyperspectral data
pre-correction	partial atmospheric correction by subtracting the atmospheric path radiance component from the radiance at the sensor
reference channel	channel located on the wings of an absorption feature
signature	characteristic shape of the electromagnetic spectrum of an (atmospheric) constituent
sun photometer	direct solar irradiance measurement instrument
slew rate effect	image distortion effect in whiskbroom scanner systems, caused by slow amplifiers
terrain adjustment	reduction of the influence of the terrain shape on the water vapor retrieval; similar to a height reduction process
view angle vector	view vector from the airplane to the scanned pixel (sometimes also called 'look angle vector')
visibility	distance, in which a dark target can be distinguished from a bright target by an human observer – often used for estimation of the aerosol amount and as tuning factor in RTCs
whiskbroom scanner	scanner principle with rotating mirror for the imaging of the single scanlines

Appendix B:

Acronyms

6S	Second Simulation of the Satellite Signal in the Solar Spectrum
AFGL	Air Force Geophysics Laboratories
APDA	Atmospheric Pre-Corrected Differential Absorption
AVIRIS	Airborne Visible/Infrared Imaging Spectrometer
ATCOR	Atmospheric Correction Program [57]
ATREM	Atmospheric Removal Program [28]
BQ	Band Quotient
BRDF	Bidirectional Reflectance Distribution Function
BRF	Bidirectional Reflectance Factor
CASI	Compact Airborne Spectrographic Imager
CCD	Charge Coupled Device
CCRS	Canada Center for Remote Sensing
CIBR	Continuum Interpolated Band Ratio
DAIS (7915)	Digital Airborne Imaging Spectrometer (7915)
DEM	Digital Elevation Model
DGPS	Differential Global Positioning System
DLR	Deutsches Luft– und Raumfahrtszentrum
DN	Digital Numbers
ENVI	Environment for Visualizing Images (RSI Inc.)
ESA	European Space Agency
FIGOS	Field Goniometer System
FOV	Field of View
FWHM	Full Width at Half the Maximum
GER	Geophysical and Environmental Research Corp.
GER3700	GER 704 Channel Portable Spectroradiometer
GIFOV	Ground Instantaneous Field of View
GIUZ	Geographisches Institut der Universität Zürich
GMT	Greenwich Mean Time
GPS	Global Positioning System
IDL	Interactive Data Language (RSI Inc.)
IR	Infrared
IFOV	Instantaneous Field of View
JPL	Jet Propulsion Laboratory, Pasadena (CA, USA)

LANL	Los Alamos National Laboratory (NM, USA)
LIRR	Linear Regression Ration
LOWTRAN	Low Resolution Atmospheric Transmission Model
LUT	Look Up Table
MODTRAN	Moderate Resolution Model for LOWTRAN7
MODO	Modtran Interface Application
NASA	National Aeronautics and Space Administration
NER	Noise Equivalent Radiance
NIR	Near–Infrared Part of the Electromagnetic Spectrum
N/W	Narrow Wide Band Ratio
PARGE	Parametric Geocoding Application
PCI	PCI Geomatics Inc.
PCIDL	IDL Interface Procedures to PCI Data Format
PSF	Point Spread Function
PSI	Paul Scherrer Institute
RMS	Root Mean Square (Error Estimate)
RSI	Research Systems Inc.
RSL	Remote Sensing Laboratories
RTC	Radiative Transfer Code (e.g. MODTRAN or 6S)
SNR	Signal to Noise Ratio
SPM	Sun Photometer
SWIR	Short–Wave Infrared Part of the Electromagnetic Spectrum
UV	Ultraviolet Part of the Electromagnetic Spectrum
VIS	Visible Part of the Electromagnetic Spectrum

Appendix C:

Hard- and Software

C.1 Hardware

This work was completed using mainly Sun Sparc workstations (SUN Ultra 2, 2x200 MHz CPU's, 45 GByte Wide SCSI disk array, 512 MByte RAM, Creator 3D Z–buffered graphic plane) running under Sun Solaris 2.5.1 operating system.

For the final image processing and publication purposes Apple Macintosh computers (Apple PowerMac 8100, 100 Mhz PPC, 3 GByte disk, 40 MByte RAM), running under MacOS 8.1 were used.

The writing was done on a Macintosh PowerBook 5300 (100MHz PPC 603 under friendly support of the Swiss National Railways (where large parts of the writing was done during travelling...).

C.2 Software

The software used for the scientific part is RSI IDL 5.0.3 (http://www.rsinc.com), RSI ENVI 3.0 (http://www.envi–sw.com), and PCI Easi/Pace 6.2 (http://www.pcigeomatics.com). The developed software was written on top of this system and is described in Appendix D. It was mainly tested and used in the IDL installation on the SUN Unix environment.

MODTRAN 3.5 was provided by the AFGL at no cost and could be installed on the SUN Unix system where all radiance simulations were done (http://www.plh.af.mil/VSBM/gpoc/modtran.html).

IDL programming took place in the convenient IDL-emacs environment (http://www.mpae.gwdg.de/mpae_RZ/software/emacs/emacs-idl.html)

Most of the Graphics were produced using IDL for Mac V5.0.2 (http://www.rsinc.com) while the images were prepared for publication using Adobe Photoshop, V4.0.2. (http://www.adobe.com)

Typesetting was done using Adobe FrameMaker 5.1.1 (http://www.adobe.com) with the Adobe Garamond and Univers family typefaces. The Adobe Acrobat Distiller was used to create the files of the PDF distribution.

Appendix D:

Description of the Developed Software

D.1 The Modo MODTRAN Utility

The MODTRAN code as provided by the AFGL is fully written in FORTRAN. It is handled by special ASCII input files, called 'tape5' for the definition of the atmosphere and 'refbkg' for background reflectance characteristics, respectively. The direct handling of these files is very sensitive and requires a lot of experience. This also bears the danger of introducing errors in the simulations. It was the goal to ease down the use of the code, by providing a graphical user interface for the creation of the input files as well as for the treatment of the outputs with respect to hyperspectral remote sensing. The efforts resulted in a shareware called 'MODO'.

Key features

- creation of standard tape5's,
- creation and dealing with multiple run tape5s,
- editing of customized atmospheres (despite aerosols),
- direct execution of MODTRAN, including tape management extensions,
- extraction of spectra from the standard MODTRAN outputs,
- plotting of the standard MODTRAN outputs,
- convolution of MODTRAN outputs to hyperspectral (Gaussian response) sensors.

The main missing features by now are the creation and editing of customized aerosol profiles, the convolution to multispectral response functions, and the direct handling of background reflectance files. These options may be introduced in the further development.

System requirements

- IDL 5.x for newest version of MODO,
- IDL 4.x version still available from ftp,
- a complete MODTRAN installation on the system is necessary since MODO only is a user interface sitting on top of Modtran,
- The interface was tested on Sun workstations and Macintosh Computers -

but since IDL is claimed to be platform- independent, it also should work on the ubiquitous Windows machines.

Depending on your MODTRAN installation the direct run feature might be disabled. Nevertheless, MODO allows creation of the tape5's on any system. Modtran then can be run externally while the output can be exploited with MODO afterwards.

Availability

The compiled software may be freely distributed 'as is' under a general shareware agreement. The shareware fee ($50) helps to maintain the application and to perform minor upgrades. Please send a mail to Daniel Schläpfer (dschlapf@geo.unizh.ch) to get information on updates and MODO - related news. The most actual version can be downloaded from anonymous ftp (ftp.geo.unizh.ch/pub/dschlapf/idl/modo). Please follow the installation instruction and type afterwards 'modo' in the IDL-prompt to start the application.

The code or special parts of the code are protected under copyright laws and may only be provided (or sold) upon special agreement.

D.2 The PARGE Application

The developed parametric geocoding algorithms were bundled in a complete application which is based on the ENVI data format and uses an additional internal data structure. Its main features are described in Section 4.4. The following list includes all options:

Features

- consistent data structure for various airborne imaging instruments,
- fully IDL (Interactive Data Language, RSI Inc.) based and therefore portable application with window based user interface,
- direct data input from ENVI, AVIRIS and DAIS data formats,
- input filters for USGS and other DEMs,
- procedures for locating, resampling and subsetting the DEM,
- synchronization of external DGPS data on scanner frequency,
- interactive filtering of attitude data (low pass / high pass / special),
- processing status management, including full status save and restore features, consistency checks and quick-views of the status,
- ground control points import from PCI/ENVI data base,
- ground control point based algorithms for auxiliary data offsets estimation:
  - roll/pitch offsetting
  - true heading offsetting (cartographic declination estimate)
  - FOV / height offsetting,
- exact correction of roll, pitch and true heading distortions (no small angle

approximations),
- flightpath reconstruction possible using ground control points information,
- two implemented geocoding algorithms for different accuracy requirements:
  - sub-pixel accuracy achieved by a DEM-oversampling algorithm (considering the effective dimensions of each pixel)
  - pixel accuracy using a pixel centre based triangulation algorithm,
- gap filling after geocoding using triangulating nearest neighbour techniques (no radiometric data modifications),
- on-line help system for direct help on procedures,
- batch processing (window independent) possible due to display-independent core program structure,
- fast final geolocating procedure using the calculated indices (allows the easy geolocation of calculation results on raw image data),
- output to desired DEM geometry in ENVI data format, additional outputs of pixel view vectors.

System requirements

- IDL 5.x (version 4.x could be compiled upon request),
- ENVI licence recommended for data preparation and further analyses,
- at least three times the memory of your desired output image dimensions,
- optimized for Unix environment (works also on memory-pumped Windows and Macintosh systems).

Availability

The first pre-release of PARGE was made available to selected users for well defined purposes and for testing only. It requires some expertise for accurate data preparation and processing decisions. The use will be eased down by expanding the on-line help system and by providing more standard filters and double check features. The full application will be commercially available in the first half of 1999.

D.3 The Sun Photometry Tools

A toolbox was created which allows the analyses of sun photometer data for standard applications. The routines cover the following topics:

Features

- data conversion and read out,
- refractive index of air calculation,
- airmass calculation,
- Langley plot analysis and calibration,
- precipitable water vapor retrieval,
- zenith angle determination (astronomical and apparent),
- vertical optical thickness calculation.

System requirements

- IDL 4.x or 5.x,
- IDL utilities collection from RSL (see Appendix D.5).

Availability

The tools and the full code are available for free upon request, or may be downloaded by ftp from ftp.geo.unizh.ch/pub/dschlapf/idl/sunphot.

D.4 The Gas Retrieval Application

All described water vapor retrieval procedures were implemented based on the PCI data format and in conjunction with MODTRAN simulation capabilities. The collection includes the whole process, starting with channel selection, method evaluation up to APDA processing and data output handling.

Features

- channel selection analysis,
- method evaluation based on channel combinations,
- fifferential absorption techniques,
- dlew rate correction procedures,
- LUT creation based on MODTRAN runs,
- subset creation based on PCI imaging spectroscopy cube,
- quantification function fitting,
- atmospheric pre-corrected differential absorption,
- optimization of the path radiance term,
- terrain modelling techniques:
  - profile retrieval
  - terrain adjusted water vapor distribution retrieval,
- output scaling of absolute water vapor amounts.

A widget user interface bundles the main parts of the differential absorption techniques and the terrain modelling. Conversely, data preparation and validation is not menu driven.

Availability

The single modules are available upon request. The basic widget application is only for internal use and lacks completeness as well as full on-line help. However it also may be distributed upon request. Some of the key features will be available in future atmospheric correction applications.

D.5 Various

Some procedures were developed and customized for the use as libraries for building applications:

PCIDL Interface

Interface for read and write to the PCI data format from IDL. The main features are:

- PCI-Header read/write,
- channel read/write (except for IMAGELN linked PCI files),
- database creation (IDL-CIM),
- segment read/write (not all segment types supported).

ENVI Interface

Interface to the ENVI data format, based on procedures from Peter Strobl (DLR). They support:

- ENVI-Header read/write,
- ENVI file open, read/write, close (simultaneous opening of various files),
- ENVI geolocating read/write.

Data Quality Analysis

- Signal to Noise estimation,
- filtering algorithms.

Programming Library

- standard alert, status and control widgets which allow display-independent programming,
- standard data format interface procedures (columnar ASCII etc.).

Help System

A help system was created which allows the use the (old) standard IDL help system and to directly access the standard help texts in the procedure headers from within applications or from the IDL-prompt.

Availability

The distribution of the PCIDL and ENVI data format interfaces is restricted. However, the code or these compiled procedures can be provided (or sold) upon special request. All other procedures are available for free or over anonymous ftp from ftp.geo.unizh.ch/pub/dschlapf/idl/utils.

References

[1] Anger C.D., Babey S.D., and Adamson R.J., 1990: A New Approach to Imaging Spectroscopy. In *Imaging Spectroscopy of the Terr. Environ.* SPIE, Orlando (FL), 1298:72–85.

[2] Bach H., and Mauser W., 1994: Atmospheric Correction of Hyperspectral Data in Terms of the Determination of Plant Parameters. In *EOS / SPIE Symposium ROM*, Munich, 10 pp.

[3] Bartoloni A., Mochi M., and Milillo G., 1995: An Algorithm for the Reconstruction of Columnar Aerosol Size Distribution from Spaceborne Spectrometer Data. In *Sensors and Env. App. of R. S.*, Askne (Ed.), Balkema, Rotterdam, pp. 337–341.

[4] Berk A., Bernsten L.S., and Robertson D.C., 1989: MODTRAN: A Moderate Resolution Model for LOWTRAN7. AFGL Technical Report, GL–TR–89–0122, Hanscom AFB, MA, 38 pp.

[5] Bevington P.R., and Robinson D.K., 1992: *Data Reduction and Error Analysis for the Physical Sciences.* McGraw–Hill, Inc., New York, 330 pp.

[6] Bizzarri B., 1992: Requirements and Projects for High Resolution Atmosperic Sounding. In *Central Symposium of the 'International Space Year'*, ESA, Paris, pp. 201–210.

[7] Borel, C.C., Gerstl, S.A.W., and Powers, B.J.,1991: The Radiosity Method in Optical Remote Sensing of Structured 3–D Surfaces. *Remote Sens. Environ.* 36:13–44.

[8] Borel C.C., and Gerstl S.A.W., 1994: Non–linear Spectral Mixing Models for Vegetative and Soil Surfaces. *Remote Sens. Environ.* 47:403–416.

[9] Borel C.C., and Schläpfer D., 1996: Atmospheric Pre–Corrected Differential Absorption Techniques To Retrieve Columnar Water Vapor: Theory and Simulations. In *6th Ann. JPL Airb. Earth Sc. Workshop*, Pasadena (CA), pp. 13–21.

[10] Bruegge C.J., Conel J.E., Margolis J.S., Green R.O., Toon G., Carrère V., Holm R.G. and Hoover G., 1990: In–situ Atmospheric Water–Vapor Retrieval in Support of AVIRIS Validation. In *Imaging Spectroscopy of the Terr. Environ.*, SPIE, Orlando (FL), 1298:150–163.

[11] Carrère V., and Conel J.E., 1993: Recovery of Atmospheric Water Vapor Total Column Abundance from Imaging Spectrometer Data around 940 nm – Sensitivity Analysis and Application to Airborne Visible/ Infrared Imaging Spectrometer (AVIRIS) Data. *Remote Sens. Environ.* 44:179–204.

[12] Chang S.–H., Westfield M.J., Lehmann F., Oertel D., and Richter R., 1993: 79–Channel Airborne Imaging Spectrometer. In *Imaging Spectroscopy of the Terr. Environ.*, SPIE, Orlando (FL), 1937:164–172.

[13] Chrien T.G., Green R.O., and Eastwood M.L., 1990: Accuracy of the Spectral and Radiometric Laboratory Calibration of the Airborne Visible/Infrared Imaging Spectrometer (AVIRIS). In *Imaging Spectroscopy of the Terr. Environ.*, SPIE, Orlando (FL), 1298:37–49.

[14] Chrien T.G., Green R.O., Chovit C.J., Eastwood M.L., and Sarture C.M., 1996: Calibration of the Airborne Visible/Inrared Imaging Spectrometer in the Laboratory. In *6th Ann. JPL Airb. Earth Sc. Workshop*, JPL, Pasadena (CA), I:39–48.

[15] Ciddor P.E., 1996: Refractive Index of Air: New Equations fo the Visible and Near Infrared. *Applied Optics*, Opt. Soc. of Am. 35(9):1566–1573.

[16] Clark R.N., Swayze G., Heidebrecht K., Goetz A.F.G., and Green R.O., 1993: Comparision of Methods for Calibrating AVIRIS Data to Ground Reflectance. In *4th Ann. JPL Airb. Geosc. Workshop*, JPL, Pasadena (CA), I:35–36.

[17] De Jong S.M.,and Chrien T.G., 1996: Mapping Volcanic Gas Emissions In The Mammoth Mountain Area. In *6th Ann. JPL Airb. Earth Sc. Workshop*, Pasadena (CA), I:75–80.

[18] Denker J.S., 1996: *See How It Flies*. Available from World Wide Web: <http://www.monmouth.com/~jsd/how/htm/>, ISBN 7016405, chapter 19.

[19] Deschamps P.Y., Herman M., and Tanré D., 1983: Definitions of Atmospheric Radiance and Transmittance in Remote Sensing. *Remote Sens. Environ.* 13:89–92.

[20] Edlen K., 1966: The Refractive Index of Air. *Metrologia*, 2:12.

[21] Ehsani A.R., and Reagan J.A., 1992: A Microprocessor Bad Auto Sun–Tracking Multi–Channel Solar Radiometer System. In *Dig. of IGARSS'92*, Houston (TX) 3 pp.

[22] Frouin R., Deschamps P.–Y, and Lecomte P., 1990: Determination from Space of Atmospheric Total Water Vapor Amounts by Differential Absorption Near 940 nm: Theory and Airborne Verification. *J. of Appl. Meteorology*, Am. Met. Soc., 29: 448–459.

[23] Forgan B.W., 1994: General Method for Calibrating Sun Photometers. *Applied Optics*, Opt. Soc. of Am., 33(21):4841–4850.

[24] Furger M., Dommen J., Graber W.K., Prévôt A., Poggio L., Andreani S., Keller J., Portmann W., Bürki D., Erne R. and Richter R. (1996) Vertical ozone transport in the Alps (VOTALP): The valley experiment 1996. *Annual Report 1996, Annex V*, Paul Scherrer Insitute, Villigen, Switzerland

[25] Gao B.–C., and Kaufman Y.J., 1995: Correction of Thin Cirrus Effects in AVIRIS Images using the sensitive 1.375–µm Cirrus Detecting Channel. In *Fifth Ann. JPL Airb. Earth Sc. Workshop*, JPL, Pasadena (CA), I:59–62.

[26] Gao B.–C., and Goetz A.F.H., 1990a: Determination of Total Column Water Vapor in the Atmosphere At High Spatial Resolution from AVIRIS Data Using Spectral Curve Fitting and Band Ratioing Techniques. In *Imaging Spectroscopy of the Terr. Environ.*, SPIE, Orlando (FL) 1298:138–149.

[27] Gao B.–C., and Goetz A.F.H., 1990b: Column Atmospheric Water Vapor and Vegetation Liquid Water Retrievals from Airborne Imaging Spectrometer Data. *J. of Geophysical Research*, 95(D4):3549–3564.

[28] Gao B.–C., Heidebrecht K.B., and Goetz A.F.H., 1993: Derivation of Scaled Surface Reflectance from AVIRIS Data. *Remote Sens. Environ.*, 44:165–178.

[29] Gege P., Kübler D., Mooshuber W., Müller R., Reinartz P., Schröder M., Schuly J., Van der Piepen H., Brockmann C., Cordes W., and Dörffer R., 1994: Analysis of Data from the Imaging Spectrometer ROSIS. In *1st Int. Airb. R. S. Conference and Exh.*, ERIM, Strassbourg (F), I:85–92.

[30] Gonima L., 1993: Simple Algorithm for the Atmospheric Correction of Reflectance Images. *Int. J. of Remote Sensing*, 14(6):1179–1187.

[31] Goody R.M., and Yung Y.L., 1989: *Atmospheric Radiation. 2nd Ed.*, Oxford Univ. Press, 505 pp.

[32] Green R.O., Carrère V., and Conel J.E., 1989: Measurement of Atmospheric Water Vapor Using the Airborne Visible/Infrared Imaging Spectrometer. In *Workshop Image Processing*, ASPRS, Sparkes (NV), 6 pp.

[33] Green R.O., Roberts D.A., and Conel J.E., 1996: Characterization and Compensation of the Atmosphere for the Inversion of AVIRIS Calibrated Radiance to Apparent Surface Reflectance. In *6th Ann. JPL Airb. Earth Sc. Workshop*, Pasadena (CA), I:136–146.

[34] Green R.O., Conel J.E., Margolis J., Chovit C., and Faust J., 1996: Calibration of the Airborne Visible/Inrared Imaging Spectrometer in the Laboratory. In *6th Ann. JPL Airb. Earth Sc. Workshop*, Pasadena (CA), I:115–126.

[35] Grove C.I., Hook S.J., and Paylor E.D., 1992: Spectral Reflectance of Minerals 0.4 to 2.5 Micrometers. JPL Publication 92–2, 406 pp.

[36] Holben B., Vermote E., Kaufman Y.J., Tanré D., and Kalb V., 1992: Aerosol Retrieval over Land from AVHRR Data – Application for Atmospheric Correction. *IEEE Trans. on Geosc. and R. S.*, 30(2):212–222.

[37] Jacquemoud S., and Baret F., 1990: PROSPECT: A Model of Leaf Optical Properties Spectral. *Remote Sens. Environ.*, 34:75–91.

[38] de Haan J. F., Hovenier J.W., Kokke J.M.M., and van Stokkom H.T.C., 1991: Removal of Atmospheric Influences on Satellite Imagery: A Radiative Transfer Approach. *Remote Sens. Environ.*, 37(1):1–21.

[39] Kasten F., and Young A.T., 1989: Revised optical airmass tables and approximation formula. *Applied Optics*, Opt. Soc. of Am., 28(22):4735–4738.

[40] Kaufman Y.J., and Gao B.–C. 1992: Remote Sensing of Water Vapor in the Near IR from EOS/MODIS. *IEEE Trans. on Geosc. and R. S.*, 30(5):871–884.

[41] Killinger D.K., Churnside J.H., and Rothman L.S., 1995: Atmospheric Optics. In *Handbook of Optics*, M.Bass (Ed.), Opt. Soc. of Am., McGraw–Hill, New York, Vol. I, pp. 44.1-44.50.

[42] King M.D., Kaufmann Y.J., Menzel W.P., and Tanré D., 1992: Remote Sensing of Cloud, Aerosol, and Water Vapor Properties from the Moderate Resolution Imaging Spectrometer (MODIS). *IEEE Trans. on Geosc. and R. S.*, 30(1):2–27.

[43] Kneizys F.X., Shettle E.P., Abreu L.W. Chetwynd J.H., Anderson G.P., Gallery W.O., Selby J.E.A., and Clouga S.A., 1988: Users Guide to LOWTRAN7. Opt./IR Tech. Div., AFGL, Hanscom AFB (MA), 137 pp.

[44] Kneisys F.X., Abreu L.W., Anderson G.P., Chetwynd J.H, et al., 1995: The MODTRAN 2/3 and LOWTRAN 7 Model. Philips Laboratory, prepared by Ontar Corporation, North Andover (MA), 267 pp.

[45] Kramer J.H., 1994: *Observation of the Earth and Its Environment, Survey of Missions and Sensors.* Springer–Verlag, Berlin, pp. 169ff, 186ff.

[46] Krishna Rao P., Holme S.J., Anderson R.K., Winston J.S., and Lehr P.E., 1990: *Weather Satellites: Systems, Data, and Environmental Applications.* Am. Met. Soc., pp. 69–150.

[47] Liou K.–N., 1980: *An Introduction to Atmospheric Radiation.* Academic Press, Inc., 385 pp.

[48] Marchant S., 1998: METEOSAT Weather Satellite Images from the University of Nottingham. Micropr. Lab, Cripps Comp. C., The Univ. of Nottingham, http://www.nottingham.ac.uk/meteosat.

[49] Meyer P., 1994: A parametric approach for the Geocoding of Airborne Visible/Infrared Imaging Spectrometer (AVIRIS) Data in Rugged Terrain, *Remote Sens. Environ.*, 49(2):118–130.

[50] Meyer P., Larson S.A., Hansen E.G., and Itten K.I., 1993: Preprocessing: Geocoding of AVIRIS Data using Navigation, Engineering, DEM, and Tracking System Data. In *Proc. of the 4th Ann. JPL Airborne Geoscience Workshop*, JPL, Pasadena (CA), I:127–132.

[51] Murray F.W., 1967: On the Computation of Saturation Vapor Pressure. *J. of Appl. Meteorology*, Am. Met. Soc., pp. 203–204.

[52] Neininger B., 1991: Field Phase Report of the POLLUMET–IOP's–91. POLLUMET–Koordinationsstelle, ETH, Zürich, 96 pp.

[53] Oertel D., 1994: The First Stage of the Digital Airborne Imaging Spectrometer DAIS–7915 Laboratory Calibration at DLR Oberpfaffenhofen. In *1st Int. Airb. R. S. Conference and Exh.*, ERIM, Strassbourg (F), II:214–224.

[54] Rast M., Bezy J.L., 1990: ESA's Medium Resolution Imaging Spectrometer (MERIS): Mission, System and Applications. In *Imaging Spectroscopy of the Terr. Environ.* SPIE, Orlando (FL), 1298:114–125.

[55] Realmuto V.J. (Ed.), 1992: *Proceedings of the Second TIMS Workshop.* JPL Pub. 90–55, JPL, Pasadena (CA), 74 pp.

[56] Roberts D.A., Yamaguchi Y., and Lyon R.J.P., 1986: Comparison of Various Techniques for Calibration of AIS data. In *2nd AIS workshop, JPL Publication 86-35*, JPL, Pasadena (CA), pp. 21–30.

[57] Richter R., 1996: A Spatially Adaptive Fast Atmospheric Correction Algorithm. *Int. J. of Remote Sensing*, 17(6):1201–1214.

[58] Rothman L. S., and McCann A., 1996: *HITRAN 1996.* CD-ROM prepared by Ontar Corp., North Andover (MA)

[59] Sandmeier S., and Itten K.I., 1997: A Physically–Based Model to Correct Atmospheric and Illumination Effects in Optical Satellite Data of Rugged Terrain. *IEEE Trans. on Geosc. and R. S.*, 35(3):708–717.

[60] Schaepman M., Itten K.I., Schläpfer D., Kurer U., Veraguth S., and Keller J., 1995: Extraction of Ozone and Chlorophyll A Distribution from AVIRIS Data. In *5th Ann. JPL Airb. Earth Sc. Workshop*, JPL, Pasadena (CA), 1:149-152.

[61] Schaepman M., 1998: *Calibration of a Field Spectroradiometer: Calibration and Characterization of a Non–Imaging Field Spectroradiometer Supporting Imaging Spectrometer Validation and Hyperspectral Sensor Modelling*, PhD Thesis, Dept. of Geography, University of Zurich, 146 pp.

[62] Schaepman M., Schläpfer D., Strobl P., and Mueller A., 1997: Ground Spectroradiometric Measurements in Support of the Validation of the Calibration of Digital Airborne Imaging Spectrometer (DAIS 7915) Data. In *3rd Int. Airb. R. S. Conference and Exh.*, ERIM, Copenhagen (D), I:217–223.

[63] Schaepman M., Keller P., Schläpfer D., Cathomen C., and Itten K.I., 1997: Experimental Determination of Adjacency Effects over an Eutrophic Lake using a Helicopter mounted Spectroradiometer for the Correction of Imaging Spectrometer Data. In *3rd Int. Airb. R. S. Conference and Exh.*, ERIM, Copenhagen (D), II:497–504.

[64] Schläpfer D., Keller J., and Itten K.I., 1995: Imaging Spectrometry of Tropospheric Ozone, New Methods of Channel Selection. IGARSS'95, Florence, separatum, 3 pp. (available at: http://www.geo.unizh.ch/~dschlapf/paper.html).

[65] Schläpfer D., Keller J., and Itten K.I., 1996: Imaging Spectrometry of Tropospheric Ozone and Water Vapor. In *Progress in Environ. R. S. Reas. and Applications*, E. Parlow (Ed.), 15th Earsel Symp. Basel, Balkema (Publ.), Rotterdam (NL), pp. 439–446.

[66] Schläpfer D., Borel C.C., Keller J., and Itten K., 1996: Atmospheric Pre–Corrected Differential Absorption Techniques to Retrieve Columnar Water Vapor: Application to AVIRIS 91/95 Data. In *6th Ann. JPL Airb. Earth Sc. Workshop*, JPL, Pasadena (CA), I:209–217.

[67] Schläpfer D., Keller J., and Itten K.I. 1997: Retrieval of the Horizontal and the Vertical Water Vapor Distribution from AVIRIS Data . In *7th Int. Symp. on Phys. Meas. and Sig. in R. S.*, ISPRS, Courchevel (F), II:591–598.

[68] Schmid B., Spyak P.R., Biggar S.F., Wehrli C., Sekler J., Ingold T., Mätzler C., and Kämpfer N., 1998: Evaluation of the Applicability of Solar and Lamp Radiometric Calibration of a Precision Sun Photometer Operating between 300 and 1025 nm. *Applied Optics*, Opt. Soc. of Am., 37(18):3923-3941.

[69] Schmid B., 1995: *Sun Photometry, a Tool for Monitoring Atmospheric Parameters.* PhD Thesis, Institute of Applied Physics, Bern, 140 pp.

[70] Schowengerdt R.A., 1997: *Remote Sensing: Models and Methods for Image Processing.* 2nd Ed., Academic Press, 522 pp.

[71] Schor U., 1992: Atmosphärensondierung mit Ballonsonden. Bericht 206, Inst. f. Geodäsie und Photogrammetrie, ETH Zürich, 35 pp.

[72] Smith M.O., Roberts D.A., Shipman H.M., Adams J.B., Willis S.C., and Gillespie A.R., 1987: Calibrating AIS Images Using the Surface as a Reference. In *3rd AIS Workshop, JPL Publication 87–30*, pp. 63–69.

[73] Soufflet V., Devaux C., andTanré D., 1992: Modified Lanley Plot Method for Measuring the Spectral Aerosol Optical Thickness and its Daily Variations. *Applied Optics*, Opt. Soc. of Am., 31(12):2154 –2162.

[74] Strobl P., Mueller A., Schläpfer D., and Schaepman M., 1997: Laboratory Calibration and Inflight Validation of the Digital Airborne Imaging Spectrometer DAIS 7915 for the 1996 Flight Season. In *Algorithms for Multispectral and Hperspectral Imagery III*, SPIE, Orlando (FL), 3071:225–236.

[75] Tanré D., Deschamps P.Y., Duhaut P., and Herman M., 1987: Adjacency Effect Produced by the Atmospheric Scattering in Thematic Mapper Data. *J. of Geophysical Research*, 92(D10)12.000–12.006.

[76] Tanré D., Deroo C., Duhaut P., Herman M., Morcrette J.J., Perbos J., and Deschamps P.Y, 1990: Description of a Computer Code to Simulate the Satellite Signal in the Solar Spectrum: The 5S Code. *Int. J. of Remote Sensing*, 11(4):659–668.

[77] Tetens O., 1930: Über einige meteorologische Begriffe. *Zeitschrift Geophysik*, 6:297–309.

[78] Van de Hulst H.C., 1957: *Light Scattering by Small Particles.* Dover Publications, New York, 470 pp.

[79] Vane G., and Goetz A.F.H., 1988: Terrestrial Imaging Spectroscopy. *Remote Sens. Environ.*, 24:1–29.

[80] Varosi F., 1988–1998: Varosi's General Purpose IDL Code Library (vlib). Mail Code 685, NASA/Goddard Space Flight Center, Greenbelt, MD, ftp://idlastro.gsfc.nasa.gov/pub/contrib/varosi/vlib/image.

[81] Vermote E., Tanré D., Deuzé J.L., Herman M., and Morcette J.J., 1994: Second Simulation of the Satellite Signal in the Solar Spectrum. 6S User Guide, NASA–Goddard Space Flight Center, Greenbelt (MD), 182 pp.

[82] Wang J., Anderson G.P., Revercomb H.E., and Knuteson R.O., 1996: Validation of FASCOD3 and MODTRAN3: comparison of model calculations with ground–based and airborne interferometer observations under clear–sky conditions. *Applied Optics*, Opt. Soc. of Am., 35(30):6028–6040.

[83] Woodham R.J., and Gray M.H., 1987: An Analytic Method for Radiometric Correction of Satellite Multispectral Scanner Data. *IEEE Trans. on Geosc. and R. S.*, GE–25(3):4307–4317.

[84] Young A.T., 1994: Air Mass and Refraction. *Applied Optics,* Opt. Soc. of Am., 33(6):1108–1110.

[85] Zalewski E.F., 1995: Radiometry and Photometry. In *Handbook of Optics*, M. Bass (Ed.), Opt. Soc. of Am., McGraw–Hill, New York, Vol. II, pp. 24.1-24.51.

Acknowledgements

The following institutions are gratefully acknowledged for their generous support of this study:

- the Swiss National Science Foundation for the initiative for the research project and the sponsoring of the Sun Photometer,
- the Paul Scherrer Institute (Switzerland) for the financial support,
- the Los Alamos National Laboratory (NM, USA) for the support during a six month student exchange program,
- the JPL, Pasadena (CA, USA) for providing AVIRIS data free of charge for research purposes,
- the DLR, Oberpfaffenhofen (Germany), for providing DAIS data and overflights in Switzerland,
- the RSL and the Department of Geography of the University of Zurich (GIUZ) for the facilities which allow for an efficient remote sensing work.

The following persons are acknowledged for helpful hints, patience, fruitful discussions, and friendly co-work during the time of the study:

- Prof. K.I. Itten, RSL, for his generous way of managing Ph.D. studies in the group for Remote Sensing Applications and his support for unconstrained developments,
- Johannes Keller, PSI, for his great sense for physical modelling, his continuous support, and the accurate correction of the thesis,
- Michael Schaepman, RSL, for supporting discussions and for managing the Swiss National Science Foundation Project,
- Chris Borel, LANL, for substantial input while developing the APDA technique and the support during the six months at Los Alamos (NM),
- Tobias Kellenberger, RSL, for his friendly support and his valuable corrections to the thesis.

Other persons who helped with helpful hints and testing results on the created procedures are at RSL: Peter Meyer, Peter Keller, Matthias Kneubuehler, and Ivo Leiss; at DLR: Andreas Müller, Peter Strobl, and Andrea Hausold; at LANL: Bill Clodius and Barry Smith, and at PSI: Markus Furger. The accurate english reading was done by Caroline Westort, GIUZ.

Last but not least I want to thank my wife Silvia, and all my personal friends for their friendly understanding during the sometimes stressful periods and some great recreational times in the Swiss mountains.

Remote Sensing Series

Vol. 5 *R. Schoch:* **Land-Cover Studies and Crop Acreage Estimates from Aerial Photography and Satellite Imagery – A Case Study in the Region of Ta'izz-Turbah, Yemen Arab Republic.** (246 pp, 1982, sFr.40.–)

Vol. 8 *U. Frei:* **Geometrische Korrekturen von NOAA-AVHRR-Daten.** (87 pp, 1984, sFr. 25.–)

Vol. 10 *M. Keller:* **Ausaperungskartierung mit Landsat-MSS Daten zur Erfassung ökologischer Einflussgrössen im Gebirge.** (111 pp, 1987, sFr. 36.–)

Vol. 11 *M. Baumgartner:* **Schneeschmelz-Abflusssimulationen basierend auf Schneeflächenbestimmungen mit digitalen Landsat-MSS und NOAA-AVHRR-Daten.** (201 pp, 1987, sFr. 35.–)

Vol. 13 *K. Ch. Graf:* **Verwendung geodätischer Abbildungen bei der Geocodierung von Satellitenbildern.** (116 pp, 1988, sFr. 30.–)

Vol. 14 *H. H. Schiesser:* **Fernerkundung von Hagelschäden mittels Wetterradar untersucht an Ackerkulturen.** (199 pp, 1988, sFr. 35.–)

Vol. 15 *E. Meier:* **Geometrische Korrektur von Bildern orbitgestützter SAR-Systeme.** (137 pp, 1989, sFr. 35.–)

Vol. 16 *P. Meyer:* **Segmentierung und symbolische Beschreibung als Grundlage zur Klassifikation landwirtschaftlicher Kulturen in einem Multispektralscanner-Datensatz.** (151 pp, 1990, sFr. 40.–)

Vol. 17 *K. Itten, P. Meyer, T. Kellenberger, C. Affentranger, I. Leiss:* **Mapping of Swiss Forests with NOAA-AVHRR.** (62 pp, 1991, sFr. 30.–)

Vol. 18 *K. Itten, P. Meyer, T. Kellenberger, R. Lee, St. Sandmeier, P. Bitter and K. Seidel:* **Correction of the Impact of Topography and Atmosphere on Landsat-TM Forest Mapping of Alpine Regions.** (50 pp, 1992, sFr. 40.–)

Vol. 19 *B. Oester:* **Erfassen der Waldschaden-Entwicklung anhand von grossmassstäblichen Infrarot-Farbluftbildern.** (163 pp, 1991, sFr. 40.–)

Vol. 20 *U.J. Burkart:* **Simulation und Prognose des Schmelzwasserabflusses sowie Bestimmung des regionalen Schneewasseräquivalents unter Zuhilfenahme von Satellitenbilddaten – dargestellt am Beispiel des Einzugsgebietes Rhein-Felsberg und Teilgebieten.** (126 pp, 1991, sFr. 40.–)

Vol. 21 *H. Haefner, A.H. Schumann:* **Remote Sensing Applications in Hydrology and Water Resources Management.** (39 pp, 1992, sFr. 30.–)

Vol. 22 *U. Frei:* **Compilation of Cartographic and Spaceborne Remote Sensing Data for Thematic/Topographic Mapping.** (102 pp, 1993, sFr. 40.–)

Vol. 23 *F. Holecz:* **Postprocessing von SAR-Satellitenbilddaten.** (149 pp, 1993, sFr. 40.–)

Vol. 24 *A.A. Darvishsefat:* **Einsatz und Fusion von multisensoralen Satellitenbilddaten zur Erfassung von Waldinventuren.** (146 pp, 1995, sFr. 40.–)

Vol. 25 *K. Ch. Graf:* **Realistic Landscape Rendering using Remote Sensing Images, Digital Terrain Models and 3D Objects.** (120 pp, 1995, sFr. 40.–)

Vol. 26 *St. Sandmeier:* **A Physically-Based Radiometric Correction Model. Correction of Atmospheric and Illumination Effects in Optical Satellite Data of Rugged Terrain.** (144 pp, 1995, sFr. 40.–)

Vol. 27 *W. Brüsch:* **Das Snowmelt Runoff Model ETH (SRM-ETH) als universelles Simulations- und Prognosesystem von Schneeschmelz-Abflussmengen.** (166 pp, 1996, sFr. 45.–)

Vol. 28 *T. Kellenberger:* **Erfassung der Waldfläche in der Schweiz mit multispektralen Satellitenbilddaten. Grundlagen, Methodenentwicklung und Anwendungen.** (290 pp, 1996, sFr. 35.–)

Vol. 29 *M. Suter:* **Aspekte der interaktiven real-time 3D-Landschaftsvisualisierung.** (150 pp, 1997, sFr. 40.–)

Vol. 30 *D. Small:* **Generation of Digital Elevation Models through Spaceborne SAR Interferometry.** (168 pp, 1998, sFr. 40.–)

Vol. 31 *M. Schaepman:* **Calibration of a Field Spectroradiometer.** (146 pp, 1998, sFr. 35.–)

Vol. 32 *D. Schläpfer:* **Differential Absorption Methodology for Imaging Spectroscopy of Atmospheric Water Vapor.** (131 pp, 1998, sFr. 30.–)

Contact:

***Remote Sensing Laboratories,** Department of Geography*
University of Zurich-Irchel, Winterthurerstrasse 190
***CH-8057 Zurich,** Switzerland*
Phone 0041-1-635 51 31, Fax 0041-1-635 68 42